Hybrid Atomistic–Continuum Formulations for Gaseous Flows

by

Hettithanthrige Sanith Wijesinghe

S.M. Aeronautics and Astronautics, Massachusetts Institute of Technology (1998)
MEng. Aeronautical Engineering, Imperial College, U.K. (1996)

Submitted to the Department of Aeronautics and Astronautics in partial fulfillment of the requirements for the

degree of

Doctor of Philosophy

at the

Massachusetts Institute of Technology

September 2003

Author_____
Department of Aeronautics and Astronautics
August 1st, 2003

Certified by_____
Nicolas G. Hadjiconstantinou
Associate Professor of Mechanical Engineering, MIT
Thesis Supervisor

Certified by_____
David L. Darmofal
Associate Professor of Aeronautics and Astronautics, MIT

Certified by_____
Mark Drela
Professor of Aeronautics and Astronautics, MIT

Certified by_____
Alejandro L. Garcia
Professor of Physics, San Jose State University

Accepted by_____
Edward M. Greitzer
H. N. Slater Professor of Aeronautics and Astronautics, MIT
Chairman, Committee On Graduate Students

Hybrid Atomistic–Continuum Formulations for Gaseous Flows

by

Hettithanthrige Sanith Wijesinghe

Submitted to the Department of Aeronautics and Astronautics
on August 1st, 2003, in partial fulfillment of the
requirements for the degree of
Doctor of Philosophy in Aeronautics and Astronautics

Abstract

Hybrid atomistic–continuum formulations allow the simulation of complex hydrodynamic phenomena at the nano and micro scales without the prohibitive cost of a fully atomistic approach. This is achieved through a domain decomposition strategy whereby the atomistic model is limited to regions of the flow field where required and the continuum model is implemented side–by–side in the remainder of the domain within a single computational framework. The current work is focused on arguably the most critical elements of any hybrid formulation: the atomistic–continuum coupling method and the imposition of continuum boundary conditions on the atomistic subdomain. The relative merits of different approaches for both are delineated and demonstrated using sample test problems.

For the case of incompressible steady gaseous flows a hybrid formulation is developed using a finite element method for the continuum subdomain and the direct simulation Monte Carlo (DSMC) method for the atomistic subdomain. The Schwarz alternating method is used to couple both subdomains using an overlap region across which the successive exchange of Dirichlet boundary conditions yields a steady state solution. This approach has the advantages of decoupling both length scales and time scales of the atomistic and continuum solvers leading to superior performance over conventional explicit schemes. Continuum boundary conditions are imposed on the atomistic subdomain using the Chapman–Enskog distribution function in conjunction with particle reservoirs. A driven cavity test problem shows convergence in $O(10)$ Schwarz iterations for flow Reynolds numbers $O(1)$.

The Schwarz method is also, for the first time, extended to couple unsteady hybrid incompressible flows. Tests for an impulsively driven Couette flow highlight the versatility of this approach to advance solutions to arbitrary times through appropriate interpolation of Dirichlet boundary conditions. Techniques are also developed using limited ensemble averaging of the atomistic solution to realize significant computational savings over a standard ensemble averaging process while maintaining the same variance reduction.

Finally an unsteady compressible hybrid formulation utilizing Adaptive Mesh and Algorithm Refinement (AMAR) technology is described. DSMC is used to model the atomistic regions on the finest grid of the adaptive hierarchy. The continuum flow is solved using a second order Godunov scheme. New gradient–based tolerance parameters are developed to provide robust detection and tracking of concentration diffusion fronts and stationary and moving shock waves. Extension of AMAR to binary gas mixtures is also completed and demonstrated using a binary gas shock wave test problem.

Thesis Supervisor: Nicolas G. Hadjiconstantinou
Title: Associate Professor of Mechanical Engineering

Acknowledgments

I've had the great privilege to learn from a multitude of faculty, administrators and peers throughout my graduate career. Much of my personal and professional development was driven by the interactions and discussions I've had with this community. I'd like to take this opportunity to acknowledge those who've made a significant impact on my life and cared about my welfare and success in many ways.

First and foremost I'd like to thank my advisor Prof. Nicolas Hadjiconstantinou for providing me an opportunity to work in an immensely captivating research field. In my graduate school application essay I stated my interests were "..to pursue computational fluid dynamics and its application to complex flows". I had little idea at the time how this objective would translate to a specific research topic and had serious doubts about the practicality of my expectations. Thanks to Nicolas however I've managed to remain focused throughout and have now, finally, reached this goal. The analysis in this thesis is owed in whole to the many discussions we've had. I've truly benefited from Nicolas' mentorship.

I'd also like to acknowledge the guidance provided by Prof. Alejandro Garcia. He spent considerable time teaching me the specifics of the "Bird" routines and was extremely patient through all my mistakes navigating a new simulation code. I'd also like to acknowledge Alej's kindness and generosity for making my visits to California first of all possible and also enjoyable. His advising style has taught me much about how best to encourage and motivate.

I'd also like to thank all the folks at CASC; Rich Hornung, Andrew Wissink, Steve Smith and Xabier Garaizar for providing me access to the computational resources and support at Lawrence Livermore. Rich has always been available to answer my technical questions and has also been helpful to navigate numerous administrative hurdles. His code forms the foundation of the analysis conducted using AMAR and I am grateful to him for providing me access and installation help -the latter half of this thesis would not have been possible otherwise. Andrew has helped me many times to resolve frustrating compiling issues and Steve's visualization software and data reduction routines have been invaluable. Xabier has facilitated many details "behind the scenes" to make my visits to the lab possible for which I am also very thankful.

I'd also like to acknowledge my thesis committee members Mark Drela, David Darmofal and Andreas Schulz for their guidance and support. They've all made time for me through busy and hectic schedules. I greatly appreciate this. I'd also like to thank Anthony Patera and Alfio Quarteroni for very valuable discussions regards domain decomposition methods.

My non–academic pursuits have been a journey of self discovery very much as important as my research endeavors. I owe a great deal to the Graduate Student Council which I joined the very first week I arrived at MIT. I've benefited tremendously from the interactions with many peers who've taken time out to serve the larger graduate student com-

munity; Eugene Bae, Luis Ortiz, Joost Bonsen, Geoffrey Coram, Alvar Otero, John Lock, Vijay Shilpiekandula, Erich Caulfield, Albert Chow, Barun Singh, Christina Silcox, Sharon Karackattu, Matt Traum, Fleming Ray, Christiane Struve, Syed Alam, David Collins, Terence Fan, Chris Tan, Brian Schneider, Eva Moy, Veronique Bugnion, Yanqing Du, Ying Li, Pubudu Wariyapola, Sriram Krishnan, Sham Sokka, Ronak Bhatt, Manish Jethwa, Dilan Seneviratne, Soulaymane Kachani, Adam Lorenz, Peter Madden....the list goes on and on. I will remember all the projects we worked on for years to come.

I've also had the pleasure of getting to know a dedicated team of MIT staff and administrators who are committed to improve the welfare of graduate students: Ike Colbert, Larry Benedict, Blanche Staton, Barrie Gleason, Elizabeth Reed, Hannah Bernstein, John Nonnamaker, Bob Simha, Lydia Snover, Kelvin Chin, Toni Robinson, Sally Susnowitz, Amy McCreath, Danielle Guichard-Ashbrook, Byran Tamburro, Maria Raposo, Marie Stuppard and last but not least Emmi Snyder. The topics of our discussions are too numerous to list here but I've learnt a great deal about the opportunities, challenges and processes for change at MIT during our numerous conversations over the years. I'd especially like to thank Ike Colbert for the financial assistance he provided me during the latter half of my degree.

Throughout the years I've also been blessed with many close friendships. Ranmali, Priyanka, Shane, Huzaifa, Tatsuo, Ashi, Nishi, Ishani, Rushani, Chandika, Gayathri, Marco, Prasanga, Tom and Nina -thank you for all the great times. I hold them close to heart.

Finally I dedicate this thesis to my parents and sister whose love, support and sacrifice over the years have made it possible for me to pursue all my ambitions. I owe all my achievements to you.

Contents

List of Figures

List of Tables

Nomenclature

Symbols

A	signed area of a grid cell face
a	local speed of sound
At	Atwood number
$\mathbf{C}$	thermal velocity vector
$\mathcal{C}$	normalized thermal velocity vector
$\mathbf{c}$	particle velocity vector in reservoir
c	mass concentration of reference fluid species
$\mathcal{D}$	diffusion coefficient
d	diameter of atomistic collision cross–section
E	specific energy
$\delta\mathcal{F}$	refluxing correction
$\mathbf{F}$	flux vector
$\mathbf{f}$	arbitrary function
$\mathbf{g}$	arbitrary boundary condition
H	specific enthalpy
h	overlap region width
J	coordinate transformation jacobian
Kn	Knudsen number
k	Boltzmann's constant
$\mathbf{L}$	linear operator
L	length of domain, characteristic dimension

l	cell dimension
l_j	non–dimensional jump length
l_s	non–dimensional slip length
$\mathcal{M}$	reduced mass
M	Mach number, number of collisions
m	atomic mass
N	total number of particles
N_{1--6}	velocity interpolation functions
N^P_{1--3}	pressure interpolation functions
N_b	number of normal velocity nodes
N_c	number of particles per cell
N_E	ensemble counter
N_{ef}	effective number
N_{m1}	DSMC time step counter
N_S	Schwarz iteration counter
N_T	time step integration counter
n	number density
$\mathbf{n}$	surface normal
P	pressure
$\mathbf{p} = (p_x, p_y, p_z)$	vector of momentum densities
p	time step ratio between subdomains
Pr	Prandlt number
q	dimensionless heat flux
$\mathcal{R}$	uniform deviate, reservoir region
$\mathbf{R}$	vector of surface tractions
R	universal gas constant
R_ρ	density gradient tolerance parameter
R_{mc}	mass concentration gradient tolerance parameter
R^{dev}_{mc}	mass concentration deviation tolerance parameter
$\mathbf{r}$	particle position vector
Re	Reynolds number
S	surface element

T	temperature
t	time
$\mathbf{U}$	Euler solution state vector
U	characteristic velocity scale
U_{dc}	driven cavity velocity
$\mathbf{u} = (u_x, u_y, u_z)$	fluid velocity vector
u	x–component of velocity
V	system volume
V_c	cell volume
V_0	wall velocity
$\mathbf{v}$	particle velocity vector
v	y–component of velocity
v_r^{max}	maximum relative velocity
W	weighting factor
w	z–component of velocity
$\Delta x, \Delta y, \Delta z$	grid spacing

Greek

δ	mean atomistic spacing, Kronecker delta
η	natural coordinate
Γ	part of domain boundary
γ	ratio of specific heats, non–dimensional density gradient
κ	thermal conductivity
λ	particle mean free path
μ	viscosity
ν	kinematic viscosity
Ω	domain region
$\partial\Omega$	boundary of domain
ϕ	azimuthal angle

ρ	mass density
σ	atomic diameter, standard deviation
σ_T	energy accommodation coefficient
σ_v	momentum accommodation coefficient
τ	mean collision time, dimensionless shear stress tensor
θ	vertical angle
ξ	natural coordinate

Subscripts

0	mean
1,2	first, second species
I,II	first, second subdomains
α	particle index
c	continuum
cm	center of mass
e	element specific
i,j,k	coordinate indices
max	maximum
n	temporal index
p	particle
r	relative
w	wall value
x,y,z	spatial coordinates

Superscripts

δ	intermediate time index
i, k	time step indices

n	time iteration index

Operators and Modifiers

$\widetilde{()}$	Non–dimensionalized quantity
[]	matrix quantity
$(^*)$	post–collision quantity
$\langle\rangle$	mean value
Δ	Difference operator
∇	Gradient operator

Acronyms

AMR	Adaptive Mesh Refinement
AMAR	Adaptive Mesh and Algorithm Refinement
DSMC	Direct Simulation Monte Carlo
FEM	Finite Element Method
MD	Molecular Dynamics
RMI	Richtmyer–Meshkov Instability
SAMRAI	Structured Adaptive Mesh Refinement Application Infrastructure

Chapter 1

Introduction

The objective of this Chapter is to give an introduction to hybrid atomistic–continuum formulations and their purpose. While the current work is focused on gaseous systems, liquid systems will also be described briefly for completeness. The limitations of current hybrid formulations are then described and a set of research questions outlined. Finally the key contributions from this work is summarized together with the thesis structure.

1.1 Background

The physics of fluid phenomena span a wide range of length scales from the atomistic through the atmospheric. Two parallel formulations exist to predict the gas flow behavior that spans these length scales; the discrete or atomistic formulation and the continuum formulation. As shown in Figure 1-1 the range of validity of each formulation can be mapped with respect to a non–dimensional length scale, the Knudsen number, $Kn = \lambda/L$ where λ is the atomistic mean free path ($= 4.9 \times 10^{-8}$m for air) and L is a characteristic dimension.

Design tools based on continuum formulations are traditionally preferred for engineering applications due to their computational efficiency but are increasingly reaching their limit of applicability especially within the operating environments typical of novel nano and micro-electro-mechanical systems (N/MEMS). Ducts of width 100nm or less which are common in such applications correspond to Knudsen numbers of order 1 or above [15].

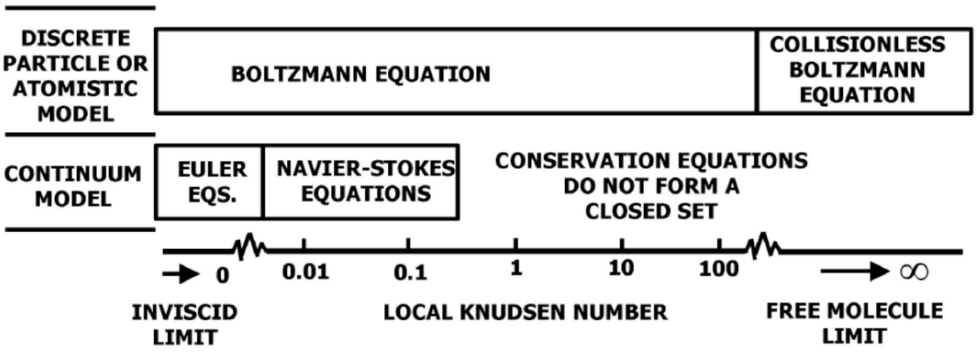

Figure 1-1: The Knudsen number limits on hydrodynamic formulations. Adapted from [20].

The Knudsen number for Helium leak detection devices and mass spectrometers can reach values of up to 200 [87]. Also material processing applications such as chemical vapor deposition and molecular beam epitaxy involve high Knudsen number flow regimes [26]. The assumption of a fluid continuum deteriorates not only with increase in Knudsen number but also in the vicinity of material interfaces and sharp gradients. In particular continuum formulations for high Mach number moving shock waves are reported to generate spurious post-shock oscillations [10, 98].

Figure 1-2 depicts an alternate view of the effective limits of the continuum formulation with respect to characteristic dimension and gas density ratio (here δ = inter–atomic spacing and d = diameter of atomistic collision cross-section). This limit map shows the continuum formulation to be borderline at the micron scale even at standard temperature and pressure (density ratio = 1). The errors resulting from the use of a continuum formulation can therefore be significant. For example, the load capacity of a hard–drive mechanism predicted by continuum equations at standard temperature and pressure and $Kn = O(1)$ is in error by more than 30% [34, 4]. While greater accuracy can be obtained over a broader range of length scales using an atomistic formulation, there are practical limitations caused by the substantial computational overhead required for a Molecular Dynamics (MD) or direct simulation Monte Carlo (DSMC) atomistic simulation approach. A significant challenge therefore exists to develop accurate yet efficient design tools for gas flow modeling at the nano and micro scales.

In response to this challenge, "hybrid" atomistic–continuum simulations have been

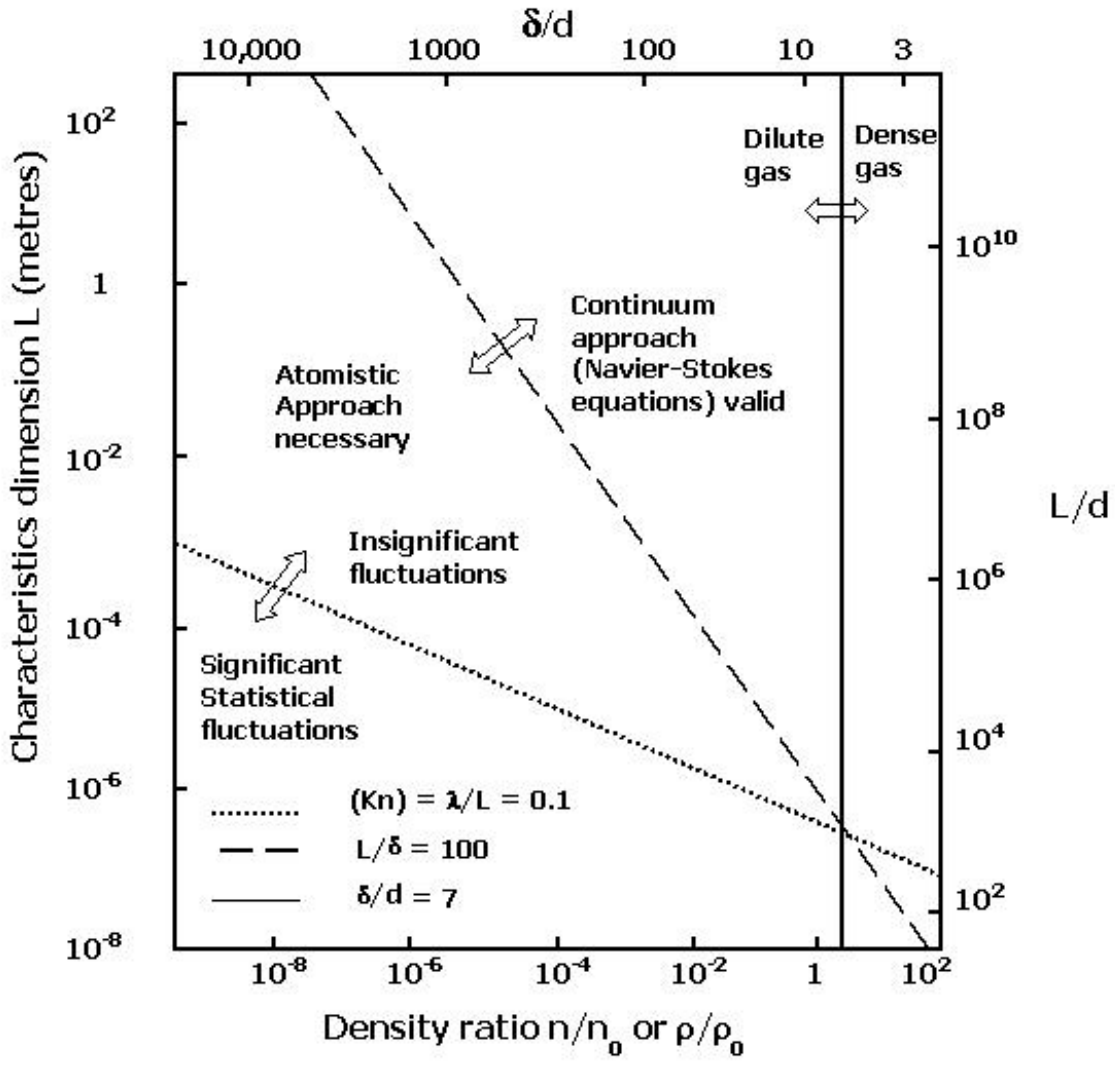

Figure 1-2: Effective limits of the continuum formulation based on density ratio and system characteristic dimension. n_o, ρ_o are the number and mass densities at standard temperature and pressure. Adapted from [20]. Reproduced with help [44].

proposed as a novel approach to model hydrodynamic flows across multiple length and time scales. These hybrid approaches limit atomistic models to regions of the flow field where needed and allow continuum models to be implemented side–by–side in the remainder of the domain within a single computational framework. A hybrid method therefore allows the simulation of complex hydrodynamic phenomena which require modeling at the microscale without the prohibitive cost of a fully atomistic calculation.

1.2 Development of a Hybrid Scheme

Over the years a fair number of hybrid simulation frameworks have been proposed. Original hybrid methods focused on dilute gases [90, 91, 31, 51, 76], which are arguably easier to develop than their liquid counterparts mainly because boundary condition imposition is significantly easier in the former. The first hybrid methods for liquids appeared a few years later [69, 47, 48, 33]. Numerous hybrid schemes have also been proposed and demonstrated for solids [1, 77, 82]. All these initial attempts have led to a better understanding of the challenges associated with hybrid methods.

To a large extent, the two major issues in developing a hybrid method is the choice of a coupling method and the imposition of boundary conditions on the atomistic simulation. These two can in general be viewed as decoupled. The coupling technique can be developed on the basis of matching two compatible and equivalent hydrodynamic descriptions over some region of space and can hence borrow from the already existing and extensive continuum–based numerical methods literature. This is further discussed in Section 1.2.1. Boundary condition imposition can be posed as a general problem of imposing macroscopic boundary conditions on an atomistic simulation. This is a very challenging problem that has not yet been resolved. Continuum boundary condition imposition on the atomistic subdomain is discussed in Section 1.2.2. Atomistic boundary condition imposition on the continuum subdomain is generally well understood, as is the process of extracting macroscopic fields from atomistic simulations (typically achieved through averaging).

1.2.1 Atomistic–Continuum Coupling

The choice of coupling procedure is one of the most important aspects of hybrid method development. Although not originally realized, it is intimately linked to the nature of the flow (elliptic/hyperbolic) just like in continuum–only numerical methods. Unfortunately, significant confusion has resulted regarding the relative merits and applicability of different coupling approaches.

Hybrid atomistic–continuum coupling belongs to the field of heterogeneous domain decomposition [73]. This is a generalization of the classical, homogeneous domain decomposition approach in which the *same kind* of problem occurs in each subdomain [74]. Examples include the propagation of electromagnetic waves in heterogeneous media with different conductivity coefficients [8] and fluid–structure interaction between the action of blood flow and compliant vessel walls [71]. Multiple non–overlapping and/or overlapping domains $\Omega_i,\ i = 1...n$ can be utilized to partition the complete computational domain Ω. Common to all decompositions is the problem of coupling solutions across a shared interface Γ. A wide range of numerical formulations have been proposed which utilize both state variable (Dirichlet) and flux variable (Neumann) boundary conditions and combinations thereof [43]. One of the most popular techniques is that of explicit time coupling that lends itself naturally to coupling hyperbolic conservative formulations by matching fluxes. A second type of approach uses exchange of state properties or fluxes to achieve implicit (in time) coupling to either given times for time–dependent problems or steady states in steady problems. In this thesis prototypical examples from these two general classes of coupling methods are used to illustrate and investigate their relative advantages and general characteristics in the context of hybrid atomistic–continuum formulations.

It is important to realize that a particular coupling procedure is not the objective but a means to obtain a hybrid method. In other words, just like in continuum–only numerical methods, the *flow physics* dictates *both* a) the use of say, a compressible or incompressible formulation in the continuum subdomain (the atomistic description captures both limits automatically) and b) the coupling method that best matches the characteristics of the mathematical formulation. Considerations which influence the choice of coupling method is expanded on below under the assumption that the hybrid method is applied to problems

of practical interest and therefore the continuum subdomain is appropriately large. The discussion below focuses on time scale considerations that are more complex but are equally important to limitations resulting from length scale considerations, such as the size of the atomistic region(s).

It is well known [94] that the time step for explicit integration of the compressible formulation, Δt_c, scales with the physical time step, $\Delta t_h = \Delta x_c/U$ (which is in balance with the physical time scale L/U), according to

$$\Delta t_c \leq \frac{M}{1+M}\Delta t_h \tag{1.1}$$

where Δx_c is the continuum grid spacing, U is a characteristic velocity scale and M is the Mach number. As the Mach number becomes small, the well–known stiffness problem arises whereby a) numerical efficiency degrades due to disparity of the time scales in the system of equations and b) the accuracy of the compressible solution degrades due to mismatch of magnitudes between fluxes in the original equations and the corresponding terms in the numerically added artificial viscosity [97]. For this reason, when the Mach number is small, the incompressible formulation is often used which allows integration at the physical time step Δt_h. In the hybrid case, matters are complicated by the introduction of the atomistic integration time step, Δt_m, which is at most of the order of Δt_c (for some cases in gases) and in most cases significantly smaller (liquids). One consequence of Equation (1.1) is that as the global domain of interest grows, Δt_h grows and transient calculations in which the atomistic subdomain is explicitly integrated in time using Δt_m become more computationally expensive and eventually infeasible. The limitation of using a compressible formulations for incompressible flow fields has however not been evident to date since the test problems used for hybrid scheme verification consist of small continuum subdomains and small total integration times; neither of these assumptions hold in practical flow problems where hybrid formulations should ideally be applied. The severity of this problem increases with decreasing Mach number and makes unsteady incompressible problems very computationally expensive. New integrative frameworks which coarse grain the time integration of the atomistic subdomain are therefore required.

Fortunately, for low speed steady problems implicit methods exist which provide solu-

tions without the need for explicit integration of the atomistic domain to the global problem steady state. The particular method developed here is known as the Schwarz method and is described shortly. In the variant used in this thesis coupling is achieved by exchange of state variable boundary conditions. This is preferable because, as discussed later, the relative error due to statistical sampling in flux quantities is higher than the error in state variables. Although other iterative methods based on both state variable and flux variable exchange exist and may be preferable in some cases, we find that the Schwarz method suffices for our purposes and serves as a good example of implicit techniques for the discussion purposes of this thesis.

Note that compressible formulations may still be used in the continuum subdomain for low speed flows. In fact, preconditioning techniques which allow the use of the compressible formulation at very low Mach numbers have been developed [94]. Such a formulation can, in principle, be used to solve the continuum problem while being coupled to the atomistic simulation via an implicit approach. What should be *avoided* is a time–explicit coupling procedure for solving essentially incompressible steady state problems. This becomes especially acute when the continuum subdomain is significantly larger than the atomistic subdomain, i.e. situations for which hybrid schemes should practically be applied.

On the other hand, Schwarz–type implicit techniques based on the incompressible physics of the flow require a fair number of iterations for convergence ($O(10)$). These iterations require the re–evaluation of the atomistic solution. This is an additional computational cost that is not shared by explicit time coupling. At this time, the choice between a explicit formulation or a Schwarz–type implicit formulation for incompressible unsteady problems is not clear and may be problem dependent. Despite the fact that as L grows the advantage seems to shift towards Schwarz–type methods, recall that from Equation (1.1), unless time coarse–graining techniques for the atomistic subdomain are developed, large, low–speed, unsteady problems are currently too expensive to be feasible by either method. These issues are investigated further in Chapter 5.

An additional consideration must be made regards the choice of state variable or flux variable based coupling formulations vis-á-vis noise concerns related to the atomistic solution. The flux–based formulation suffers from adverse signal to noise ratios in connection with the averaging required for imposition of boundary conditions from the atomistic subdo-

main to the continuum subdomain. In the case of an ideal gas it has been shown in [50] that, for the same number of samples, flux (shear stress, heat flux) averaging exhibits relative noise E_f, which scales as,

$$E_f \approx \frac{E_{sv}}{Kn} \tag{1.2}$$

where E_{sv} is the relative noise in the corresponding state variable (velocity, temperature) which varies as $1/\sqrt{(\text{number of samples})}$. Here $Kn = \lambda/L$ is the Knudsen number based on the characteristic length scale of the transport gradients, L, and λ is the mean free path which is expected to be much smaller than L since, by assumption, a continuum subdomain is present. It thus appears that coupling using flux variables will be significantly disadvantaged in this case since $1/Kn^2$ times the number of samples required by state–variable averaging is required to achieve comparable variance reduction in the matching region where $Kn \ll 1$.

In the remainder of this Section, the Schwarz alternating method and time explicit coupling methods are described further.

The Schwarz Alternating Method

The Schwarz alternating method is a coupling approach borrowed from the field of domain decomposition [74]. The basic features of this coupling method are illustrated in Figure 1-3. Within this coupling framework, an overlap region facilitates information exchange between the continuum and atomistic subdomains in the form of Dirichlet boundary conditions. A steady state continuum solution is first obtained using boundary conditions taken from the atomistic subdomain solution. At the first iteration this latter solution can be a guess. A steady state atomistic solution is then found using boundary conditions taken from the continuum subdomain. This exchange of boundary conditions corresponds to a single Schwarz iteration. Successive Schwarz iterations are repeated until convergence, i.e. until the solution in the two subdomains are identical in the overlap region. The Schwarz procedure is guaranteed to converge for elliptic problems [61], and has recently been shown to converge for finite but sufficiently small Reynolds numbers [62]. The significant advantage of the exchange of boundary conditions in the above described manner is that time scales can

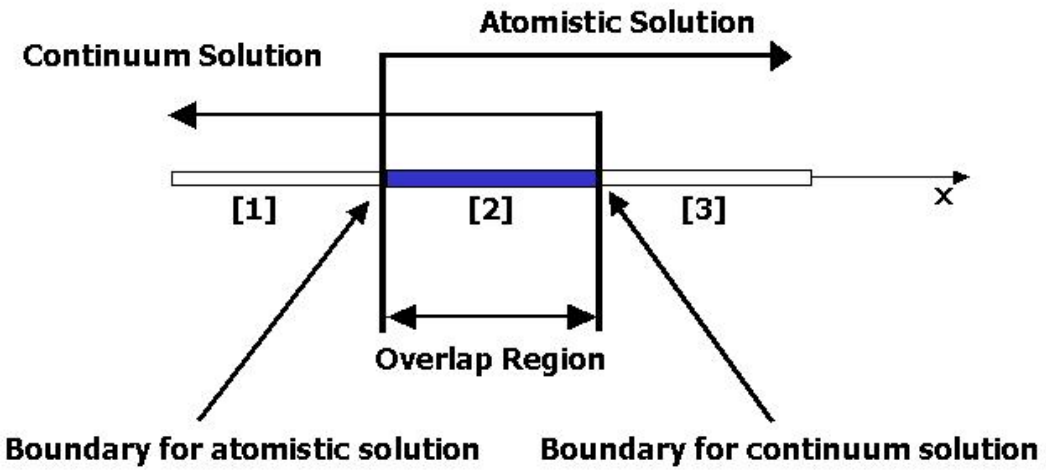

Figure 1-3: The Schwarz alternating method in 1–dimension.

be decoupled since only steady state solutions are required from each subdomain. Hence the atomistic and continuum subdomains can be advanced at a locally optimal time step. Most importantly, steady solutions to large problems (for which explicit time integration at the atomistic scale is impractical) are feasible since the time required for the atomistic subdomain to reach steady state is small and hence integration of the atomistic subdomain to this time is possible.

The use of the Schwarz method for hybrid schemes was first described by Hadjiconstantinou and Patera [47] and was used to couple a Molecular Dynamics description of a dense fluid with a Navier–Stokes continuum flow solver. More recently Aktas and Aluru [2] use the Schwarz method for the simulation of flow through micro machined filters. These filters have sufficiently small passages such that an atomistic description is required to simulate the flow through them. Depending on the geometry and number of filter stages the authors report computational savings ranging from 2 to 100.

The use of the Schwarz method to obtain an implicit solution to steady state problems is not only significantly more efficient than an explicit time march, but also allows continued time integration of the atomistic subdomain for variance reduction purposes. This is particularly important for low speed flows where the signal to noise ratio is significant. Additionally the Schwarz coupling approach will have lower susceptibility to noise as only state–variable averaging is required.

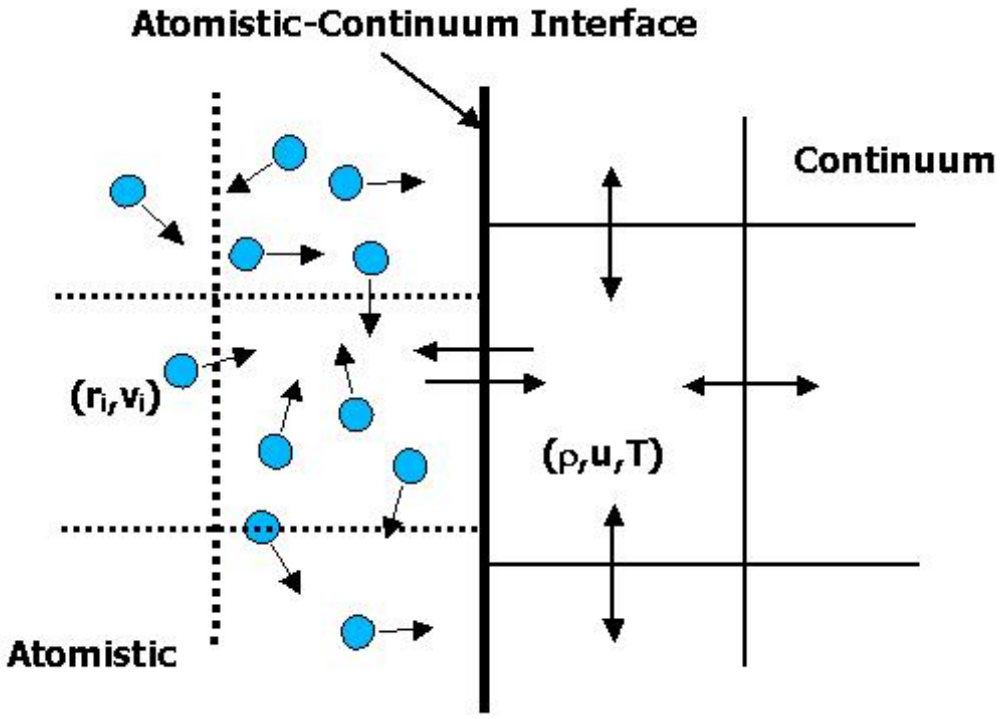

Figure 1-4: Atomistic–continuum coupling using flux conservation. The atomistic subdomain is simulated using direct simulation Monte Carlo (DSMC) in this example. Adapted from [56].

Explicit Coupling Method

Atomistic–continuum coupling may also be achieved by explicit time integration of fluxes across the atomistic–continuum interface. This is illustrated schematically in Figure 1-4. The atomistic fluxes are imposed on the continuum subdomain by the summation of mass, momentum and energy of particles that cross the atomistic–continuum interface. Similar bookkeeping is performed to impose the continuum fluxes on the atomistic subdomain by utilizing particle reservoirs that overlap with the continuum subdomain. Particle reservoirs are discussed in Section 1.2.2.

The Adaptive Mesh and Algorithm Refinement (AMAR) compressible hybrid formulation by Garcia et al. [36] pioneered the use of mesh refinement as a natural framework for explicit time coupling of atomistic and continuum fluxes. In AMAR the typical continuum mesh refinement capabilities are supplemented by an algorithm refinement (continuum to atomistic) based on continuum breakdown criteria. This seamless transition is both theoretically and practically very appealing. Using the Adaptive Mesh Refinement (AMR)

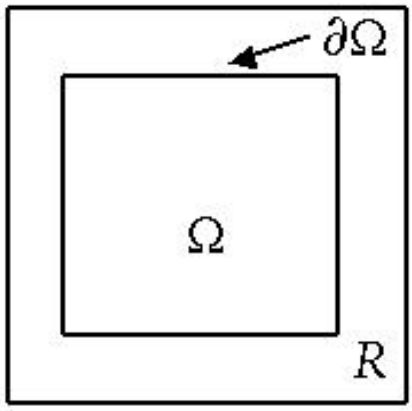

Figure 1-5: Continuum to atomistic boundary condition imposition using reservoirs.

capabilities provided by the Structured Adaptive Mesh Refinement Application Infrastructure (SAMRAI) developed at the Lawrence Livermore National Laboratory [84], the above adaptive framework has been implemented in a fully three-dimensional, massively parallel form in which multiple atomistic patches can be introduced or removed as needed. Additional details of this AMAR hybrid scheme are provided in Chapter 6.

While explicit coupling helps realize the computational savings of the hybrid formulation in a spatial sense, the temporal coupling between the atomistic and continuum formulations limit the total integration time that can be achieved unless significant computational resources are available.

1.2.2 Continuum to Atomistic Boundary Condition Imposition

The most popular approach for imposing continuum boundary conditions on an atomistic simulation is by using "particle reservoirs" $\mathcal{R}$, surrounding an atomistic region Ω as shown in Figure 1-5. The reservoir serves as a region in which the dynamics of the atomistic simulation particles are altered to ensure the appropriate boundary conditions appear on $\partial\Omega$.

The use of reservoirs to impose continuum boundary conditions on atomistic descriptions of dilute gases has received significant attention [36]. In a dilute gas, the non–equilibrium velocity distribution function in the continuum limit has been characterized [22]

and is known as the Chapman–Enskog distribution. The use of this distribution results in a robust, accurate and theoretically elegant approach. Typical implementations [36] require the use of particle generation and initialization within $\mathcal{R}$. Particles that move into Ω within the atomistic time step are added to the simulation whereas particles remaining in $\mathcal{R}$ are discarded. Additional details are covered in Section 4.2.

The same does not hold for liquids however where not only the particle velocities but also the atomic structure needs to be imposed. No theoretical results exists for the non–equilibrium distribution function of these quantities. Nevertheless Li et al. [60] used a Chapman–Enskog distribution to impose boundary conditions to generate a dense–fluid shear flow. In this approach, particles crossing $\partial\Omega$ acquire velocities that are drawn from a Chapman–Enskog distribution parametrized by the local values of the required velocity and stress boundary condition. Although this approach was only tested for a Couette flow, it appears to give reasonable results (within atomistic fluctuations). In a different approach, Flekkoy et al. [33] use external forces to impose boundary conditions. More specifically, in the reservoir region they apply an external field of such magnitude that the total force on the fluid particles in the reservoir region is the one required by momentum conservation. There is no theoretical description however that specifies how such a force should be distributed amongst the individual particles. Also it is not clear whether this method can be used to model flows with components normal to $\partial\Omega$; the authors only present results for Couette and Poiseuille flows with flow velocities parallel to $\partial\Omega$.

An additional issue for liquid simulations is that of terminating the atomistic domain Ω or reservoir $\mathcal{R}$ such that the fluid state inside Ω is not significantly affected. Hadjiconstantinou and Patera [47] proposed the use of fully periodic boundary conditions around the reservoir $\mathcal{R}$. This approach has minimum impact on particle dynamics inside Ω provided $\mathcal{R}$ is large. Unfortunately the number of simulation particles grows rapidly with $\mathcal{R}$ and therefore the approach incurs additional computational cost. Flekkoy et al. [33] terminate their reservoir region by using an ad–hoc weighting factor for the force distribution on particles within $\mathcal{R}$ such that particles are prevented from leaving the reservoir region. It is not clear however what effect these forces have on the local fluid state (it is well known that even in a dilute gas gravity driven flow exhibits significant non–continuum effects [63]). In more recent work Delgado–Buscalioni and Coveney [29] follow the approach by [33] but distribute

Scheme	System	Approximation	Coupling
Aktas and Aluru [2]	Gas	Steady, incompressible, viscous	Schwarz
Garcia et.al. [36]	Gas	Unsteady, compressible, viscous	Explicit
Hadjiconstantinou [47]	Liquid	Steady, incompressible, viscous	Schwarz
Hash and Hassan [51]	Gas	Steady, compressible, viscous	Explicit

Table 1.1: Summary of existing hybrid schemes.

the external forces uniformly among all particles in the overlap region.

1.3 Questions Posed by the Current Research

A summary of recently proposed hybrid schemes are listed in Table 1.1 categorized according to the fluid system (liquid or gas) modeled, the specific flow regime considered and the atomistic–continuum coupling approach.

While hybrid formulations for liquid systems have many outstanding implementation issues, the current work will be focused on gaseous systems as non–continuum effects first appear in these flows as the characteristic length scale of interest decreases. The use of a hybrid scheme for gaseous flows is therefore justified at the typical scales of current engineering interest. These flows are typically viscous and incompressible. The first half of this thesis investigates generalized hybrid scheme formulation and implementation issues using the Schwarz alternating method for low speed gaseous flows. The following questions will be addressed:

1. General boundary condition imposition on dilute gas atomistic simulations can be performed using the Chapman–Enskog velocity distribution as described earlier. What specific implementation issues must be addressed to ensure accurate and efficient use of this approach for viscous, incompressible hybrid formulations? The most recent work in this regard [2] based on the Schwarz coupling method uses a Maxwellian velocity distribution and a "feedback control mechanism" to impose a steady Stokes continuum flow field on the atomistic simulation. This approach, although successful in quasi one–dimensional flows, is not very general. Additionally, it is well known that using a Maxwellian distribution to impose hydrodynamic boundary conditions, if un-

corrected, will lead to slip (discrepancy between the imposed and observed boundary conditions).

2. Can the Schwarz method be extended to couple unsteady incompressible flows? If so, how? Would a time explicit approach be better?

3. What strategies can be used to reduce the computational cost associated with simulating unsteady flows using hybrid formulations?

The final half of this thesis is devoted to developing extensions to the compressible AMAR hybrid formulation developed by Garcia et al. [36]. This hybrid formulation utilizes a second order unsplit Godunov method to solve the continuum Euler equations and direct simulation Monte Carlo (DSMC) for the atomistic description. The following questions will be addressed here:

1. The current implementation of AMAR simulates single gas fluid flows. What modifications are required in the atomistic and continuum solvers to accommodate two gaseous species?

2. How can the effect of atomistic fluctuations be theoretically and practically accounted for?

3. The AMAR scheme allows for novel algorithm refinement in addition to mesh refinement at the smallest level of an adaptive mesh hierarchy. What refinement criteria should be used to signal the use of an atomistic description such as to ensure accurate and efficient fluid feature tracking?

1.4 Technical Approach

The initial 3 questions will be addressed by presentation of a general formulation followed by test examples for verification purposes. The atomistic and continuum numerical schemes used in the hybrid formulation will be developed first and verified independently of the hybrid scheme. The direct simulation Monte Carlo (DSMC) method is used as the atomistic simulation approach of choice while the incompressible Navier–Stokes equations are solved

using a finite element discretization. Code for these routines are custom written to allow for easy modification within a hybrid scheme. The code development is performed under FORTRAN 77 and a LINUX RedHat operating system environment. Test simulations are run on a single processor INTEL PENTIUM processor at 550 MHz.

The final 3 questions are addressed utilizing the computational resources available at the Lawrence Livermore National Laboratory. The AMAR hybrid scheme is built on an an object oriented framework using C++ and is compiled to run on multiple processors. Test simulations were conducted on a distributed COMPAQ cluster using 1 GHz EV68 Alpha processors.

1.5 Thesis Contributions

The work conducted in this thesis has made significant contributions to the field of hybrid atomistic–continuum formulations. In particular,

- A viscous, incompressible hybrid formulation using the Schwarz alternating method and Chapman–Enskog distribution based particle reservoirs has been developed and verified using a 2–dimensional driven cavity test problem. The use of the Chapman–Enskog distribution to impose continuum boundary conditions on atomistic simulations provides an order of magnitude error reduction over current hybrid formulations using the Maxwellian distribution.

- The Schwarz coupling method for incompressible flows has been extended to couple unsteady flows. This hybrid formulation has been demonstrated using a 1–dimensional impulsively started Couette flow test problem.

- The atomistic simulation for the unsteady hybrid formulation has been accelerated using limited ensemble time integration while retaining the same variance reduction.

- The Adaptive Mesh and Algorithm Refinement (AMAR) compressible hybrid scheme has been successfully extended to simulate binary gas species and has been verified using a binary gas shock test problem.

- Robust and efficient refinement criteria have been developed based on density gradient and concentration gradient based parameters to track fluid interfaces for a number of test cases including moving shock waves, concentration diffusion and the Richtmyer–Meshkov instability. A theoretical framework which accounts for the effect of atomistic fluctuations has also been developed.

1.6 Thesis Organization

The direct simulation Monte Carlo and the finite element numerical scheme used in this work are derived in Chapter 2 and Chapter 3 respectively. Results from test examples to help verify these formulations (independent of the hybrid scheme) are also presented here. The Schwarz method applied to low speed, steady, viscous, incompressible flows is described next in Chapter 4. The use of particle reservoirs to impose continuum boundary conditions on the atomistic simulation is also described in this Chapter. Chapter 5 describes extension of the Schwarz method to unsteady flows and strategies for accelerating the atomistic subdomain time integration. An explicitly coupled high speed, compressible hybrid scheme using Adaptive Mesh and Algorithm Refinement (AMAR) is detailed in Chapter 6. Criteria for adaptive tracking of fluid interfaces are described here and verified using test cases for shock waves and concentration diffusion. Finally a summary and suggestions for future work are discussed in Chapter 7.

Chapter 2

Direct Simulation Monte Carlo

The aim of this Chapter is to describe the Direct Simulation Monte Carlo (DSMC) atomistic solver used in the hybrid formulations developed in Chapters 4, 5 and 6. The DSMC method was developed by Bird in the 1960's [18] and has been used extensively to model rarefied gas flows. A more comprehensive introduction to DSMC can be found in [20]. The DSMC routines described here were verified independently of a hybrid scheme using Couette flow simulations at finite Knudsen numbers where velocity slip and temperature jump phenomena become important.

2.1 Introduction

The DSMC method is based on the assumption that a small number of representative "computational particles" can accurately capture the bulk macroscopic dynamics and thermodynamics of a complete system of gas atoms or molecules. This assumption holds for the case of a dilute gas which is a good approximation to a real gas when the ratio of the mean atomistic spacing δ to atomistic collision cross–section d is such that $\delta/d \gg 1$. Empirical results show that a minimum of 20 DSMC particles per cubic mean free path is usually sufficient to capture the relevant physics [20]. In this case each DSMC particle corresponds to $N_{ef} = nV/N$ real atoms in the physical system where V is the system volume, n is the number density and N is the total number of DSMC particles. N is typically 2 orders of magnitude smaller than the actual number of gas atoms contained in the same volume and is a significant source for DSMC's computational savings over Molecular Dynamics (MD)

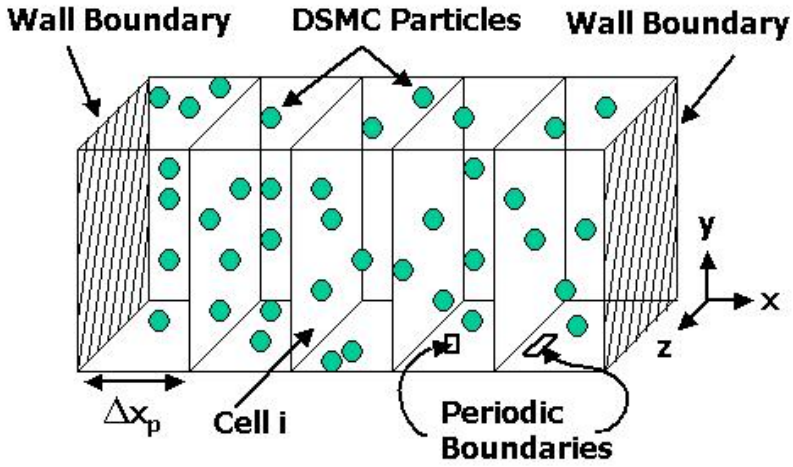

Figure 2-1: A sample computational domain for DSMC atomistic simulation.

simulations.

A sample computational domain for an atomistic simulation using DSMC is shown in Figure 2-1. The domain shown here is bounded by two walls and is periodic in the xy and xz planes. In DSMC the particle positions and velocities ($\mathbf{r}_i, \mathbf{v}_i\ , i = 1...N$) are advanced in time by a two–step process of advection and collision which corresponds to a splitting method of solution for the underlying Boltzmann equation. Particle advection is ballistic with time step Δt_p chosen to be a fraction of the mean collision time. Collisions are performed between randomly chosen particle pairs within small cells of size Δx_p. This approach has been shown to produce correct solutions to the Boltzmann equation in the limit $\Delta x_p,\ \Delta t_p \rightarrow 0$ [92]. Note that the motion of DSMC particles is inherently 3–dimensional even though a single coordinate direction is discretized in Figure 2-1. If the particle reaches a boundary in the simulation domain the positions and velocities are adjusted such that the specified boundary conditions is imposed (see below). The flow solution is determined by averaging the individual particle properties over space and time.

Recent studies [49, 37] have shown that for steady flows, or flows which are evolving at time scales that are long compared to the atomistic relaxation times, a finite time step leads to a truncation error that manifests itself in the form of time step–dependent transport coefficients; this error has been shown to be of the order of 5% when the time step is of the order of a mean free time and goes to zero as Δt_p^2. Quadratic dependence of the error in the transport coefficients on the collision cell size Δx_p was shown in [6].

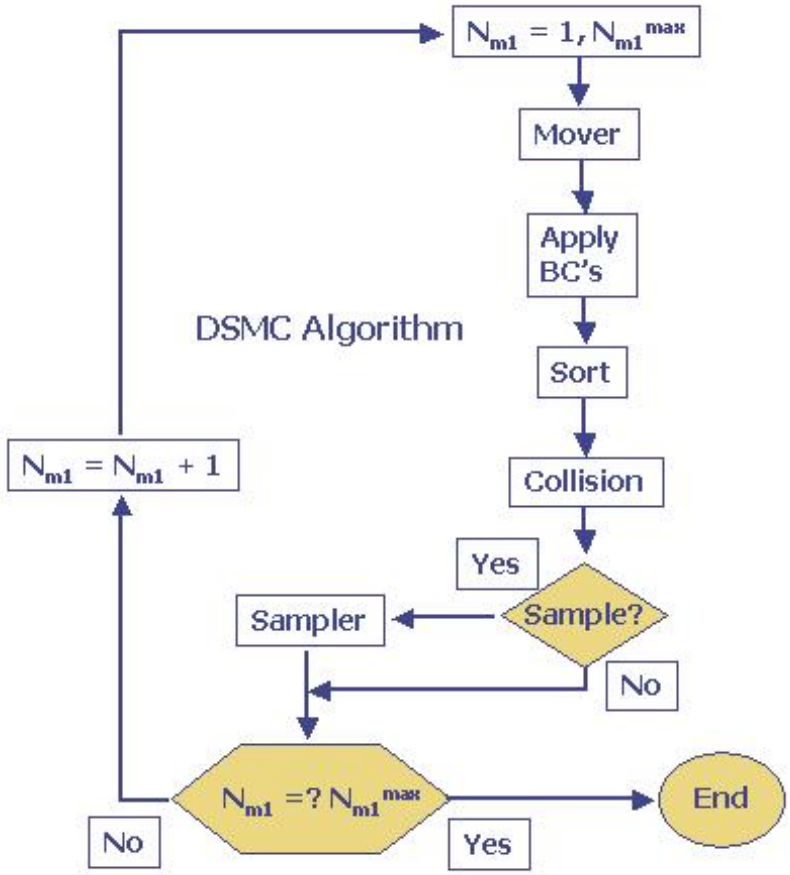

Figure 2-2: Block schematic of the DSMC algorithm. Note: "BCs" refer to boundary conditions.

2.2 DSMC Algorithm

The DSMC algorithm is best described with reference to the block schematic shown in Figure 2-2. Here N_{m1} corresponds to the DSMC time step counter and N_{m1}^{max} is the total number of DSMC time steps. Each block of the algorithm will be described briefly below.

2.2.1 Mover

Here each particle i is advanced in space with time step Δt_p according to,

$$\mathbf{r}_i(t + \Delta t_p) = \mathbf{r}_i(t) + \mathbf{v}_i(t)\Delta t_p \tag{2.1}$$

2.2.2 Apply Boundary Conditions

The particle positions r_i are then checked to determine if a boundary of the computational domain was crossed. DSMC provides flexibility in imposing a variety of boundary conditions ranging from periodic, reflection, velocity and thermal walls. Periodic boundary conditions are imposed by adding or subtracting the appropriate domain dimension to the particle position coordinate $\mathbf{r}_i$ based on the periodic face through which the particle exited the domain. Reflection boundaries are imposed by switching the particle velocity component normal to the reflection boundary. Certain combinations of periodic, reflection and velocity boundary conditions would clearly conflict and hence good judgment should be exercised to ensure chosen combinations are not mutually incompatible. In all cases the time of flight spent by a particle after leaving the computational domain should be used to determine the particle's subsequent motion after being returned into the computational domain.

Thermal boundary conditions are imposed by choosing particle velocities from a biased Maxwellian distribution [38]. For the example in Figure 2-1 with the wall boundaries held at temperature T_w say, the particle velocities after wall collision are obtained from the following velocity distribution functions,

$$P_{v_x}(v_x) = \pm\frac{m}{k_b T_w} v_x e^{-mv_x^2/2k_bT_w} \tag{2.2}$$

$$P_{v_y}(v_y) = \sqrt{\frac{m}{2\pi k_b T_w}} e^{-mv_y^2/2k_bT_w} \tag{2.3}$$

$$P_{v_z}(v_z) = \sqrt{\frac{m}{2\pi k_b T_w}} e^{-mv_z^2/2k_bT_w} \tag{2.4}$$

where m is the particle mass, k_b is the Boltzmann constant and the $\pm$ sign in Equation (2.3) corresponds to the left and right wall respectively. Additional wall velocities in the tangential direction can also be imposed on the particles by shifting the origin of the distributions accordingly. Further description of boundary condition imposition is covered in [38] together with details of routines to generate the velocity distributions using random number generators.

2.2.3 Sort

Particles are next sorted in computational cells in order to process collisions. While this process is generally straightforward it incurs a major computational expense. Routines for minimizing this cost through efficient use of data arrays are detailed in [38] and will not be covered here.

2.2.4 Collision

In DSMC, collisions are binary and occur only between particles that reside within a single computational cell. In the current implementation a hard sphere model is assumed for particle collisions which in turn defines the collision probability between particles $P_{coll}(i,j)$ as,

$$P_{coll}(i,j) = \frac{|\mathbf{v}_i - \mathbf{v}_j|}{\sum_{m=1}^{N_c} \sum_{n=1}^{m-1} |\mathbf{v}_m - \mathbf{v}_n|} \tag{2.5}$$

where N_c is the number of particles per cell. The double summation in the denominator of Equation (2.5) is expensive however, and would cause the DSMC simulation cost to grow quadratically with the number of particles. An alternate acceptance–rejection scheme is used instead, in which collision partners are selected according to the following steps [38]:

1. Select collision candidate pairs i, j at random.

2. Calculate their relative speed, $v_r = |\mathbf{v}_i - \mathbf{v}_j|$.

3. Accept pair for collision if $v_r \geq v_r^{max}\mathcal{R}$ where v_r^{max} is the maximum relative speed in the cell and $\mathcal{R}$ is a uniform deviate in [0, 1).

4. If the pair is accepted determine particle post–collision velocities.

5. After collision is processed or if the pair is rejected, return to step 1.

In step 4 the following relations can be obtained for the pre– and post– collision particle velocities (see Figure 2-3) by using the conservation of momentum and energy,

$$\mathbf{v_1} = \mathbf{v_{cm}} + \frac{m_2}{m_1+m_2}\mathbf{v_r} \tag{2.6}$$

$$\mathbf{v_2} = \mathbf{v_{cm}} - \frac{m_1}{m_1+m_2}\mathbf{v_r} \tag{2.7}$$

$$\mathbf{v_1^*} = \mathbf{v_{cm}} + \frac{m_2}{m_1+m_2}\mathbf{v_r^*} \tag{2.8}$$

$$\mathbf{v_2^*} = \mathbf{v_{cm}} - \frac{m_1}{m_1+m_2}\mathbf{v_r^*} \tag{2.9}$$

where $\mathbf{v_{cm}} = (m_1\mathbf{v_1} + m_2\mathbf{v_2})/(m_1+m_2)$ is the velocity of the center of mass which remains unchanged after collision and $\mathbf{v_r}, \mathbf{v_r^*}$ are the pre– and post– collision particle relative velocities, the magnitude of which also remain unchanged after collision. The direction of the post collision relative velocity is calculated by using the result that all directions are equally likely, i.e. that the angles θ, ϕ in Equation (2.10) are uniformly distributed over the unit sphere,

$$\mathbf{v_r^*} = v_r[(\sin\theta\cos\phi)i + (\sin\theta\sin\phi)j + \cos\theta k] \tag{2.10}$$

The azimuthal angle ϕ is uniformly distributed between 0 and 2π and is chosen as $\phi = 2\pi\mathcal{R}$ and the vertical angle θ is chosen according to the probability density $P_\theta(\theta)d\theta = 0.5\sin\theta d\theta$ [38].

Finally the total number of collisions in a cell during a time Δt_p is given by,

$$M_{coll} = \frac{N_c(N_c-1)N_{ef}\pi d^2\langle v_r\rangle\Delta t_p}{2V_c} \tag{2.11}$$

where V_c is the volume of the cell and $\langle v_r\rangle$ is the average relative velocity. Since collision candidates are selected through an acceptance–rejection scheme where the ratio of total accepted to total candidates is proportional to $\langle v_r\rangle/v_r^{max}$, the number of candidates that should be selected for collision is given by,

$$M_{cand} = \frac{N_c(N_c-1)N_{ef}\pi d^2 v_r^{max}\Delta t_p}{2V_c} \tag{2.12}$$

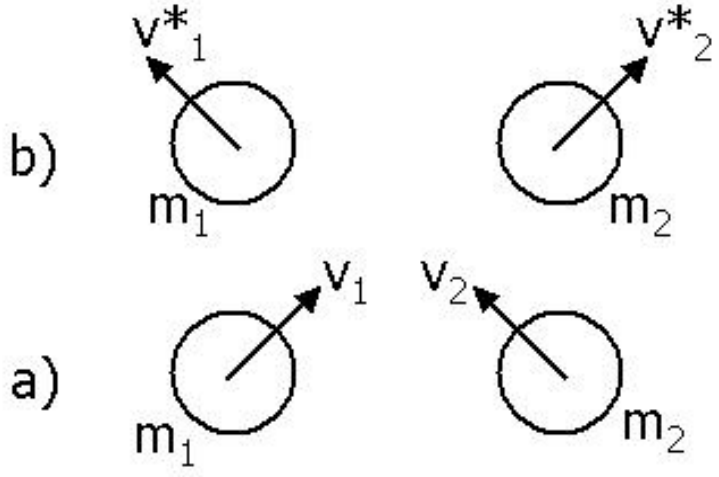

Figure 2-3: Schematic of DSMC particle collisions. a) Pre–collision velocities, b) Post–collision velocities.

Note that while hard–sphere dynamics are assumed for the collision model in this study, alternative models such as the variable hard sphere and variable soft sphere [20] have been developed that capture real gas effects. These can be easily incorporated with minimum additional effort.

2.2.5 Sampler

The sampling routines average the particle positions and velocities to calculate the cell density, velocity, and temperature. Sampling can be set to occur at pre–determined intervals. This completes a single iteration of the DSMC algorithm.

2.3 Velocity Slip and Temperature Jump in Micro–Channels

In order to verify the DSMC algorithm described in Section 2.2 an atomistic simulation of velocity slip and temperature jump in micro–channels was conducted. A brief description of these phenomena is provided first. Details of the simulation parameters are then presented together with sample results and conclusions.

2.3.1 Introduction

Maxwell [64] was the first to predict the phenomenon of velocity slip; i.e. the difference between the velocity of a gas close to the wall and the velocity of the wall in the presence of shear. This difference can be expressed as follows,

$$u_{gas}|_{wall} - U_{wall} = \alpha \frac{2 - \sigma_v}{\sigma_v} \lambda \left. \frac{du}{d\eta} \right|_{wall} \tag{2.13}$$

where σ_v is the momentum accommodation coefficient, equal to zero for specular reflections and equal to 1 for diffuse reflections [14], and η is the coordinate normal to the wall. The thermal slip at the wall is given by a similar expression,

$$T_{gas}|_{wall} - T_{wall} = \beta \frac{2\gamma}{\gamma + 1} \frac{2 - \sigma_T}{\sigma_T} \frac{\lambda}{Pr} \left. \frac{dT}{d\eta} \right|_{wall} \tag{2.14}$$

where σ_T is the energy accommodation coefficient, γ is the ratio of specific heats, and Pr is the gas Prandtl number. These expressions have been used extensively to provide simple corrections to the boundary conditions employed in the Navier–Stokes equations without the need for detailed atomistic simulations. As the characteristic length scale of engineering components continues to diminish further such relationships need to be re–evaluated. In what follows we will take $\sigma_v = \sigma_T = 1$ since this does not detract from the generality of our conclusions; consequently, our simulations will be performed with perfectly accommodating walls.

The coefficients α and β introduce corrections to the original results of Maxwell ($\alpha = \beta = 1$) that were obtained through an approximate method [23]. The theoretical models derived by Ohwada et al. [68] and Sone et al. [83] predict $\alpha = 1.11$ and $\beta = 1.13$. These values will be used for comparison with the DSMC results presented below.

In accordance with Bhattacharya et al. [17], Equations (2.13) and (2.14) can be re–written in terms of a non–dimensional slip length (l_s) and jump length (l_j) as follows,

$$l_s = \alpha Kn \tag{2.15}$$

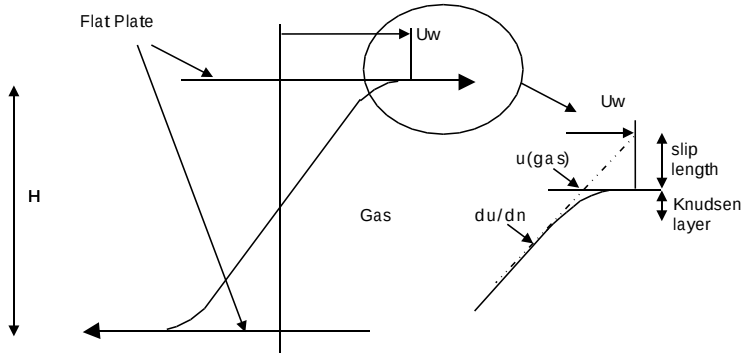

Figure 2-4: Couette flow schematic.

$$l_j = \beta \frac{2\gamma}{Pr(\gamma+1)} Kn \tag{2.16}$$

where,

$$l_s = \frac{u_{gas} - U_{wall}}{H \frac{du}{d\eta}} \tag{2.17}$$

$$l_j = \frac{T_{gas} - T_{wall}}{H \frac{dT}{d\eta}} \tag{2.18}$$

and the Knudsen number, Kn, is defined as the ratio of the mean free path $\lambda = (\sqrt{2}\pi n\sigma^2)^{-1}$ to the channel height H. Here n is the number density and σ the atomistic diameter. With these definitions for slip length and jump length, the gradients $du/d\eta$ and $dT/d\eta$ are determined from the velocity and temperature profiles outside the Knudsen layer [23]. Values for gas velocity u_{gas} and gas temperature T_{gas} are also obtained from profiles outside the Knudsen layer. This is illustrated in Figure 2-4 for $du/d\eta$ and u_{gas}.

2.3.2 Simulation Results

We simulated gaseous Argon (atomic mass $m = 6.63 \times 10^{-26}$ kg, hard sphere diameter $\sigma = 3.66 \times 10^{-10}$ m) at atmospheric conditions ($P = 1.013 \times 10^5$ Pa and average temperature $\overline{T} = 273$ K). This choice of species was due to historical and convenience reasons: the hard sphere diameter for Argon is well known to reproduce equilibrium and non–equilibrium properties accurately. Argon is historically used in the majority of DSMC studies because it provides instant availability to a substantial literature of simulation and experimental results for code validation. The present simulations use a minimum of 3 DSMC cells per mean free path and 50 particles per cell. A time step of 0.2 times the mean collision time was used to advance the simulation.

A wide range of Knudsen numbers is investigated. Figure 2-5 and Figure 2-6 shows the velocity slip results for $M = 0.1$ and $M = 0.01$ respectively expressed in terms of slip length. These results indicate the theoretical prediction [68] holds for $Kn \to 0$ and is accurate for $Kn \lesssim 0.1$.

The temperature jump results are shown in Figure 2-7 in terms of the temperature jump length. Similar to velocity slip, the theoretical results [83] are also found accurate for $Kn \lesssim 0.1$.

2.3.3 Conclusions

The following conclusions are reached in this study:

1. The DSMC results for velocity slip and temperature jump agree with the corresponding theoretical hard sphere model results [68, 83] for Knudsen numbers $Kn \lesssim 0.1$.

2. No discernible difference is observed between the slip length results for $M = 0.1$ and $M = 0.01$.

3. Both slip length and jump length simulation results are lower than the theoretical results for $Kn \gtrsim 0.1$. A factor ≈ 2 difference is seen at $Kn = 1.0$ with larger deviations at higher Kn.

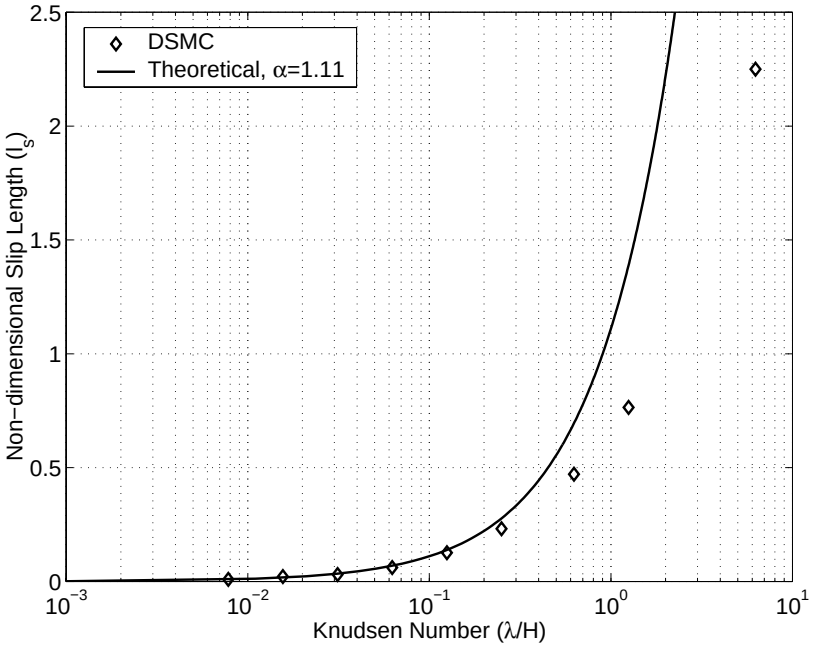

Figure 2-5: Velocity slip variation with Knudsen number for $M = 0.1$.

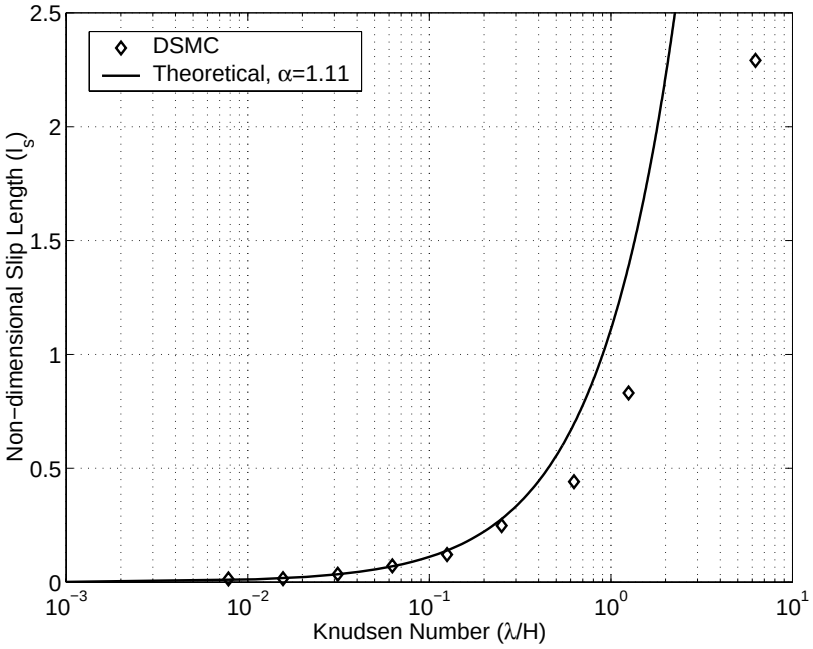

Figure 2-6: Velocity slip variation with Knudsen number for $M = 0.01$.

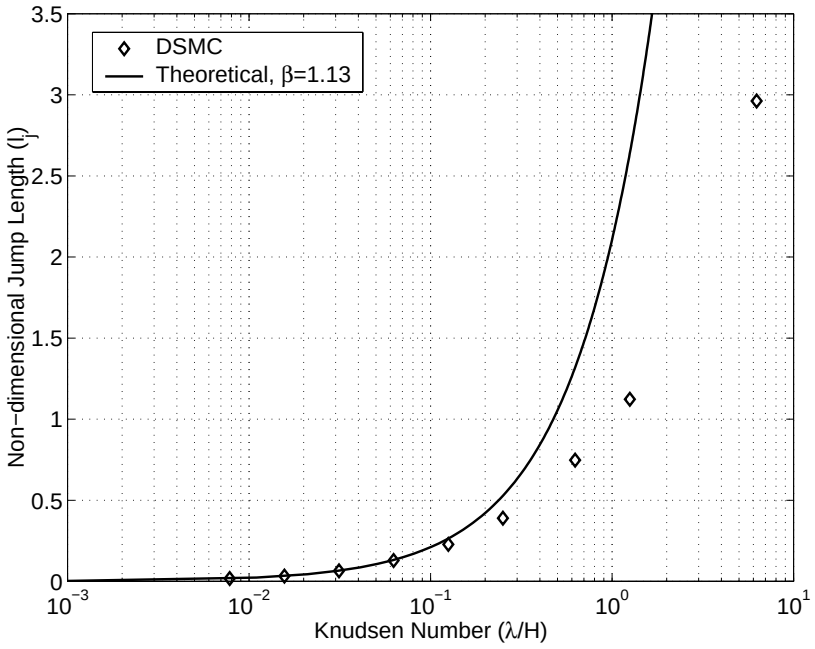

Figure 2-7: Temperature jump variation with Kn. Wall temperatures are 273 ± 5K.

4. The deviation of the DSMC results from the theoretical results for $Kn \gtrsim 0.1$ is consistent with, but also smaller than the deviation seen in the molecular dynamics (MD) simulation results obtained by Bhattacharya et al. [16] and the DSMC and MD simulation results of Morris et al. [67]. This may be due to the lower viscous heating in the present simulations. The previous MD and DSMC simulations also use Lennard–Jones pair potentials and variable hard–sphere models respectively. In both cases the mean free path is extracted in terms of the viscosity which may also lead to the differences [40].

5. The deviation between the theoretical results and simulations for $Kn \gtrsim 0.1$ is expected since the former considers a semi–infinite domain subject to a constant gradient. As Kn increases beyond 0.1 (i.e. as the channel width H decreases) molecules undergo more frequent collisions with the bounding walls. The net effect is a reduction in the mean free path λ as suggested by Morris et al. [67]. Hence by Equations (2.15) and (2.16) the corresponding slip lengths are also reduced.

Chapter 3

Finite Element Method

The purpose of this Chapter is to describe the finite element continuum solver used for the incompressible hybrid scheme developed in Chapter 4. The solver is based on the 2–dimensional, steady, incompressible Navier–Stokes equations. The formulation of the finite element solver is described first; it is verified using a driven cavity test problem. Good agreement is found with published results.

3.1 Introduction

An excellent introduction to the finite element method and its application to fluid flows can be found in Huebner [58]. In the finite element method the physical flow domain is discretized into a number of elements inside which the continuum field variables are approximated by piecewise continuous functions. For a systematic formulation, these approximating functions or interpolations are defined in terms of nodal variables. Nodes often occupy locations on the element boundary but may also be defined in the interior of the discretizing element. The continuum field at any point is defined uniquely once the nodal values are determined. Huebner [58] outlines a clear methodology for solving for the nodal values in 6 steps:

1. Discretize the continuum field equations

2. Determine the interpolation functions

3. Determine the element equations

4. Assemble the element equations to obtain the system equations

5. Impose boundary conditions

6. Solve the system equations

Each of these steps will be discussed briefly below:

3.1.1 Step 1: Discretize the continuum

The finite element method provides great flexibility to discretize complex flow geometries. Many different element types exist for both 2–dimensional and 3–dimensional domains. For the purpose of the current work a standard 2–dimensional triangular element with 6 nodes as shown in Figure 3-1 is chosen. The u and v velocity is defined at all 6 nodes of the element while the pressure P is defined only at nodes 1,2 and 3. An element defined by this particular choice of node variables is referred to as a Taylor–Hood element. The nodes of the element are defined with respect to a natural coordinate system (ξ,η). In this case the (ξ,η) coordinate pairs for nodes 1 through 6 are: $(0,1),(0,0),(1,0),(0,0.5),(0.5,0),(0.5,0.5)$ respectively. Natural coordinates help simplify the integration procedure required to obtain the element equations (described later in Section 3.1.3). Elements defined in terms of natural coordinates in this way are termed isoparametric.

3.1.2 Step 2: Determine the Interpolations Functions

The velocity and pressure fields within the Taylor–Hood element can be interpolated according to Equations (3.1)–(3.3). The index i refers to a particular node, and u_i,v_i and P_i

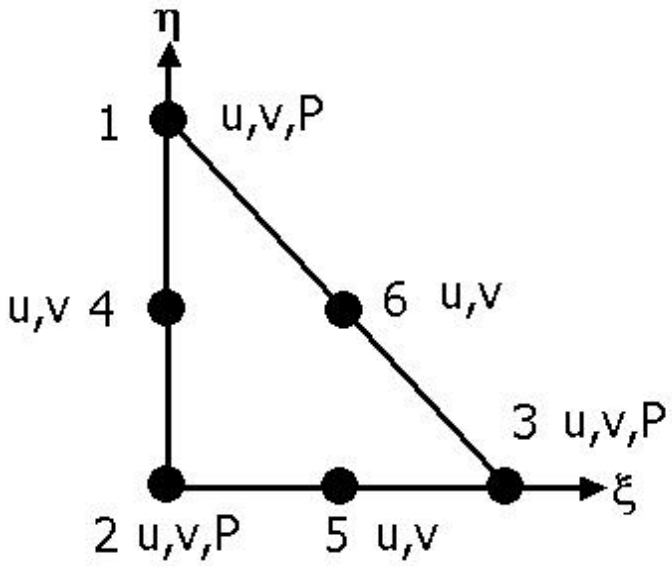

Figure 3-1: Taylor–Hood finite element.

are the nodal values of the u, v velocities and pressure P respectively.

$$u^{(e)} = \sum_{i=1}^{6} N_i^u(\xi,\eta)u_i \tag{3.1}$$

$$v^{(e)} = \sum_{i=1}^{6} N_i^v(\xi,\eta)v_i \tag{3.2}$$

$$P^{(e)} = \sum_{i=1}^{3} N_i^P(\xi,\eta)P_i \tag{3.3}$$

The expressions for the interpolation functions N_i^u, N_i^v and N_i^P are given in Equations (3.4)–(3.12). Note the interpolation functions for the u, v velocities N_i^u and N_i^v are equivalent and are referred to as N_i. As seen in these expressions the velocity field has a quadratic interpolation while the pressure field has a linear interpolation. This follows from the need established by several researchers [99, 54, 11] for the velocity interpolation to be one order higher than the pressure interpolation. Olson and Tuann [70] show that spurious rigid–body

modes occur in the element coefficient matrix unless this requirement is met.

$$N_1 = \eta(2\eta - 1) \tag{3.4}$$

$$N_2 = (1 - \xi - \eta)(1 - 2\xi - 2\eta) \tag{3.5}$$

$$N_3 = \xi(2\xi - 1) \tag{3.6}$$

$$N_4 = 4\eta(1 - \xi - \eta) \tag{3.7}$$

$$N_5 = 4\xi(1 - \xi - \eta) \tag{3.8}$$

$$N_6 = 4\xi\eta \tag{3.9}$$

$$N_1^P = \eta \tag{3.10}$$

$$N_2^P = 1 - \xi - \eta \tag{3.11}$$

$$N_3^P = \xi \tag{3.12}$$

3.1.3 Step 3: Determine the Element Equations

In Step 3 the element equations for the incompressible, steady, Navier–Stokes equations are derived. These equations for momentum and mass conservation are given in Equations (3.13)–(3.15) below.

$$\rho\left(u^n\frac{\partial u}{\partial x} + v^n\frac{\partial u}{\partial y}\right) = \frac{\partial(\tau_{xx} - P)}{\partial x} + \frac{\partial \tau_{xy}}{\partial y} \tag{3.13}$$

$$\rho\left(u^n\frac{\partial v}{\partial x} + v^n\frac{\partial v}{\partial y}\right) = \frac{\partial \tau_{xy}}{\partial x} + \frac{\partial(\tau_{yy} - P)}{\partial y} \tag{3.14}$$

$$\frac{\partial u}{\partial x} + \frac{\partial v}{\partial y} = 0 \tag{3.15}$$

Here, $\tau_{xx} = 2\mu\left(\frac{\partial u}{\partial x}\right)$, $\tau_{yy} = 2\mu\left(\frac{\partial v}{\partial y}\right)$, $\tau_{xy} = \mu\left(\frac{\partial u}{\partial y} + \frac{\partial v}{\partial x}\right)$, μ is the viscosity and u^n and v^n are approximate solutions to the x and y velocity components to be determined by successive iteration (see Section 3.1.6).

The solution to the system of equations follows the method of weighted residuals using a Bubnov–Galerkin approach [58]. In this method the momentum equations are integrated over each element using the interpolation function for velocity as a weighting function. The continuity equation is weighted by the interpolation function for pressure. This can be

written as follows,

$$\int_{\Omega_e}\left[-\rho\left(u^n\frac{\partial u}{\partial x}+v^n\frac{\partial u}{\partial y}\right)+\frac{\partial(\tau_{xx}-P)}{\partial x}+\frac{\partial\tau_{xy}}{\partial y}\right]N_i d\Omega = 0 \tag{3.16}$$

$$\int_{\Omega_e}\left[-\rho\left(u^n\frac{\partial v}{\partial x}+v^n\frac{\partial v}{\partial y}\right)+\frac{\partial\tau_{xy}}{\partial x}+\frac{\partial(\tau_{yy}-P)}{\partial y}\right]N_i d\Omega = 0 \tag{3.17}$$

$$\int_{\Omega_e}\left[\frac{\partial u}{\partial x}+\frac{\partial v}{\partial y}\right]N_i^P d\Omega = 0 \tag{3.18}$$

This velocity–pressure formulation is favored due to its easy extension to 3–dimensions and its ability to incorporate physical boundary conditions. After substituting for N_i and N_i^P using Equations (3.4)–(3.12) the resulting element equations can be re–written in matrix form as follows:

$$\begin{bmatrix} [C_{11}]+[C_{22}] & [0] & [0] \\ [0] & [C_{11}]+[C_{22}] & [0] \\ [0] & [0] & [0] \end{bmatrix}\begin{Bmatrix} \{u\} \\ \{v\} \\ \{P\} \end{Bmatrix}+$$

$$\begin{bmatrix} [2K_{11}+K_{22}] & [K_{12}] & [L_1] \\ [K_{12}]^T & [K_{11}+2K_{22}] & [L_2] \\ [L_1]^T & [L_2]^T & [0] \end{bmatrix}\begin{Bmatrix} \{u\} \\ \{v\} \\ \{P\} \end{Bmatrix}= \begin{Bmatrix} \{R_u\} \\ \{R_v\} \\ \{0\} \end{Bmatrix} \tag{3.19}$$

where,

$$C_{11} = \int_{\Omega^e}\rho u^n N\left[\frac{\partial N}{\partial x}\right]d\Omega^e \tag{3.20}$$

$$C_{22} = \int_{\Omega^e}\rho v^n N\left[\frac{\partial N}{\partial y}\right]d\Omega^e \tag{3.21}$$

$$K_{11} = \int_{\Omega^e}\mu\left[\frac{\partial N}{\partial x}\right]\left[\frac{\partial N}{\partial x}\right]d\Omega^e \tag{3.22}$$

$$K_{22} = \int_{\Omega^e}\mu\left[\frac{\partial N}{\partial y}\right]\left[\frac{\partial N}{\partial y}\right]d\Omega^e \tag{3.23}$$

$$L_1 = -\int_{\Omega^e}\left[\frac{\partial N}{\partial x}\right][N^P]d\Omega^e \tag{3.24}$$

$$L_2 = -\int_{\Omega^e}\left[\frac{\partial N}{\partial y}\right][N^P]d\Omega^e \tag{3.25}$$

The RHS terms correspond to the surface tractions and are given by,

$$R_u = \int \overline{\tau_{xx}}[N]d\Gamma \tag{3.26}$$

$$R_v = \int \overline{\tau_{yy}}[N]d\Gamma \tag{3.27}$$

$$\overline{\tau_{xx}} = (\tau_{xx} - P)n_x + \tau_{xy}n_y \tag{3.28}$$

$$\overline{\tau_{yy}} = (\tau_{yy} - P)n_y + \tau_{xy}n_x \tag{3.29}$$

The integrands in Equations (3.20)–(3.25) are expressed in terms of natural coordinates ξ and η while the integral is defined over physical space. To convert the complete expression to natural coordinates the coordinate transformation jacobian J is required such that,

$$\int_{\Omega^e} f(\xi,\eta)d\Omega^e = \int_{-1}^{+1}\int_{-1}^{+1} f(\xi_i,\eta_i)|J|d\xi d\eta \tag{3.30}$$

where $f(\xi,\eta)$ represents a given integrand and the jacobian is given by,

$$J = \begin{bmatrix} \frac{\partial x}{\partial \xi} & \frac{\partial y}{\partial \xi} \\ \frac{\partial x}{\partial \eta} & \frac{\partial y}{\partial \eta} \end{bmatrix} \tag{3.31}$$

The partial derivatives for x and y in Equation 3.31 are determined in terms of corresponding derivatives for the velocity interpolation functions N_i using the expressions in Equations (3.32)–(3.33).

$$x = \sum_{i=1}^{6} N_i(\xi,\eta)x_i \tag{3.32}$$

$$y = \sum_{i=1}^{6} N_i(\xi,\eta)y_i \tag{3.33}$$

The evaluation of the integrals is simplified by use of Gauss–Legendre quadrature. Here the integral is replaced by a summation of the integrand evaluated at finite points weighted by known coefficients W_i. For Taylor–Hood triangle elements integrand polynomials up to 5th order can be evaluated exactly using summations over just 3 points (in this case over nodes 4,5 and 6). This is summarized in Equation (3.34):

$$\int_{\Omega^e} f(\xi,\eta)d\Omega^e = \sum_{i=4}^{6} f(\xi_i,\eta_i)W_i|J| \tag{3.34}$$

where the weights $W_4 = W_5 = W_6 = 1/3$.

3.1.4 Step 4: Assemble the element equations to obtain the system equations

After the individual element equations are determined they must be combined to form the global system equations. This assembly is performed by summing the contributions of all element equation entries for a given node (and field variable) across the solution domain. This procedure is simplified by the use of a connectivity matrix that maps the local element nodes to the global system nodes. The resulting global system of equations can be written in a simplified form as shown in Equation (3.35).

$$[C(u^n, v^n)] \begin{Bmatrix} \{u\} \\ \{v\} \\ \{P\} \end{Bmatrix} + [K] \begin{Bmatrix} \{u\} \\ \{v\} \\ \{P\} \end{Bmatrix} = \begin{Bmatrix} \{R_u\} \\ \{R_v\} \\ \{0\} \end{Bmatrix} \tag{3.35}$$

3.1.5 Step 5: Impose Boundary Conditions

Once the global equations are assembled boundary conditions must be imposed before inverting Equation (3.35). The velocity–pressure formulation provides flexibility to impose both Dirichlet and Neumann velocity conditions. To impose a Dirichlet condition on the n^{th} degree of freedom in Equation (3.35), the n^{th} equation in the matrix is replaced by the Dirichlet constraint equation. Neumann conditions are prescribed directly in terms of the right hand side expressions for R_u and R_v in Equations (3.26)–(3.26) respectively.

The pressure field in an incompressible formulation contains an arbitrary additive constant. A single pressure node in the domain can therefore be specified a constant value, say atmospheric pressure, to appropriately set this constant.

3.1.6 Step 6: Solve the System of Equations

The solution of Equation (3.35) after imposing boundary conditions is performed by an iterative process using a "method of successive substitution" [41]. Rewriting the solution

vector $\{\{u\},\{v\},\{P\}\}$ at iteration $(n+1)$ as $\{\{u^{n+1}\},\{v^{n+1}\},\{P^{n+1}\}\} = \mathbf{U}^{n+1}$ and the right hand side surface tractions $\{\{R_u\},\{R_v\},\{0\}\}$ as $\mathbf{R}$ then Equation (3.35) can be written as,

$$[C(u^n, v^n)]\mathbf{U}^{n+1} + [K]\mathbf{U}^{n+1} = \mathbf{R} \tag{3.36}$$

To initialize the iterative process the velocities u^0, v^0 are set identically to 0.0. Hence the first iteration velocity field corresponds to the solution of a Stokes flow problem $[K]\mathbf{U}^1 = \mathbf{R}$. Using this method, convergence of the velocity field has been found to occur within 5 iterations for flow Reynolds numbers in the range $0 - 10,000$ [41].

3.2 Driven Cavity Test Problem

The finite element formulation detailed above is verified using a driven cavity test problem. Results are presented and compared against those in the literature for Reynolds numbers $Re = 0, 100$ and 400.

3.2.1 Introduction

The 2–dimensional, viscous, steady, incompressible flow in a driven cavity has been used for many years as the model problem to test new numerical schemes and solution methods [45, 93, 42, 86, 3]. Earlier work was reviewed by Burggraf [21] who used a vorticity–stream function formulation and finite difference discretization of the Navier–Stokes equations to solve for flows with Re up to 400. He showed the formation of a large primary vortex in the center of the cavity and smaller secondary vortices at the lower corners. Ghia et al. [42] obtained solutions up to $Re = 10,000$ using a coupled strongly implicit multigrid method also using a vorticity–stream function formulation. Their work is the most comprehensive study of cavity flow to date [57].

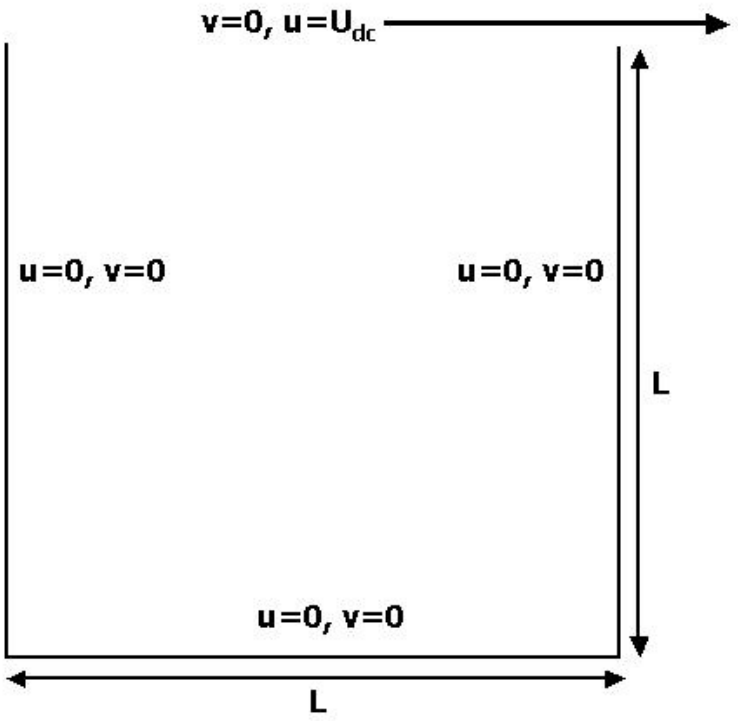

Figure 3-2: Boundary conditions for the 2–dimensional driven cavity test problem.

3.2.2 Boundary Conditions

The boundary conditions for the driven cavity problem are shown in Figure 3-2. The top boundary moves from left to right at velocity $u = U_{dc}$. All other u, v velocity components are held at zero. There are no Neumann boundary conditions imposed hence the right hand side surface tractions in Equation (3.36) are identically zero. The pressure level is set by constraining the middle node on the lower boundary to atmospheric pressure (1.013×10^5 N/m^2).

3.2.3 Computational Grid

All tests were performed for a square cavity size $L = 1 \times 10^{-6}$m using a regular cartesian grid as shown in Figure 3-3. This grid has a total of 800 triangular elements with 41 nodes in both the x and y directions. This corresponds to a total of 1681 velocity nodes and 441 pressure nodes. The grid spacing h is 5×10^{-8}m.

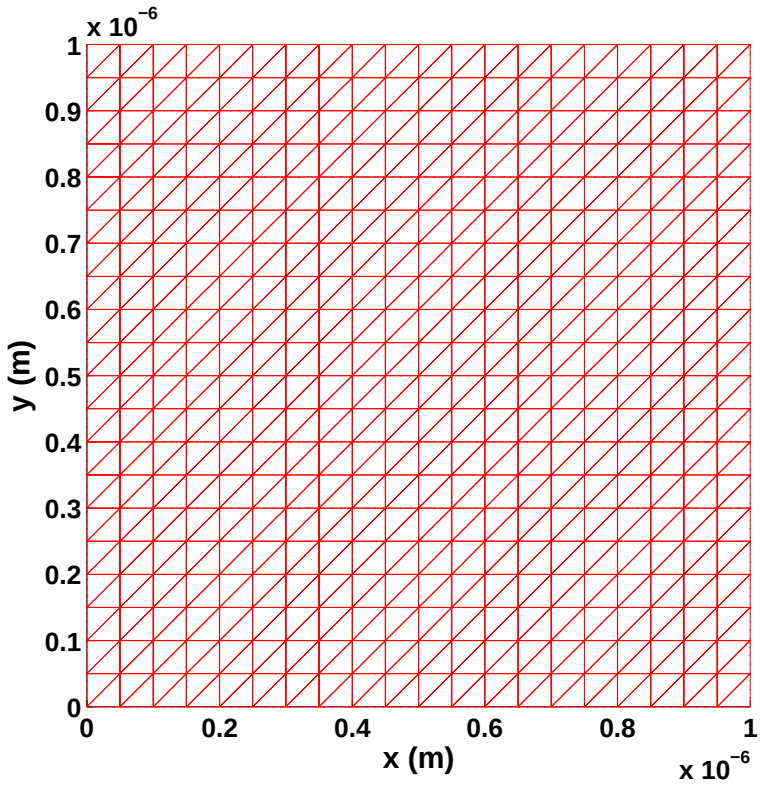

Figure 3-3: Grid for driven cavity test problem.

3.2.4 Results

Tests were conducted for $Re = 0, 100$ and 400 where the Reynolds number Re is defined by Equation (3.37) below,

$$Re = \frac{\rho U_{dc} L}{\mu} \tag{3.37}$$

Here the upper boundary velocity $U_{dc} = 50\,\mathrm{m/s}$, cavity height $L = 1 \times 10^{-6}\mathrm{m}$, fluid viscosity $\mu = 2.08 \times 10^{-5}\,\mathrm{kg/(ms)}$ and density $\rho = 41.62, 41.62, 166.48\,\mathrm{kg/m^3}$ respectively. The viscosity and density values chosen here do not correspond to that of a specific fluid but are chosen to achieve the given Reynolds number.

The $Re = 0$ test corresponds to a Stokes flow solution obtained by setting the convective terms to zero ($[C] = 0$) and solving $[K]\mathbf{U}^1 = \mathbf{R}$. This also corresponds to a solution with viscosity $\mu \gg 1$. Note this Stokes flow solution is also recovered as the first iterate solution in the method of successive substitution (Section 3.1.6) for the $Re = 100$ and $Re = 400$

Reynolds Number	Reference	x/L	y/L
0	e	0.5000	0.7500
100	a	0.6188	0.7375
	b	0.6172	0.7344
	c	0.6167	0.7417
	d	0.6196	0.7373
	e	0.6240	0.7250
400	a	0.5563	0.6000
	b	0.5547	0.6055
	c	0.5571	0.6071
	d	0.5608	0.6078
	e	0.5740	0.6000

Table 3.1: Comparison of the location of primary vortex centers in driven cavity flow. a, Vanka [89], b, Ghia et al. [42], c, Schreiber and Keller [80], d, Hou et al. [57], e, Current work. This table is adapted from Hou et al. [57].

tests. A total of 5 iterations were used to converge the solution for the flow at these higher Reynolds numbers. The velocity and pressure results from the tests are shown as contour plots in Figure 3-4 through Figure 3-12. These results compare well graphically with the contour plots by Burggraf [21].

The location of the primary vortex center (obtained using contour plots of the speed distribution) are compared against values in the literature in Table 3.1. The results from the current work differ from previous results on average by 2%.

The y variation of the u velocity at $x/L = 0.5$ is plotted in non–dimensional form and compared with results from Burggraf [21] in Figures (3-13),(3-14) and (3-15) for $Re = 0, 100$ and 400 respectively. Generally good qualitative and quantitative agreement is found.

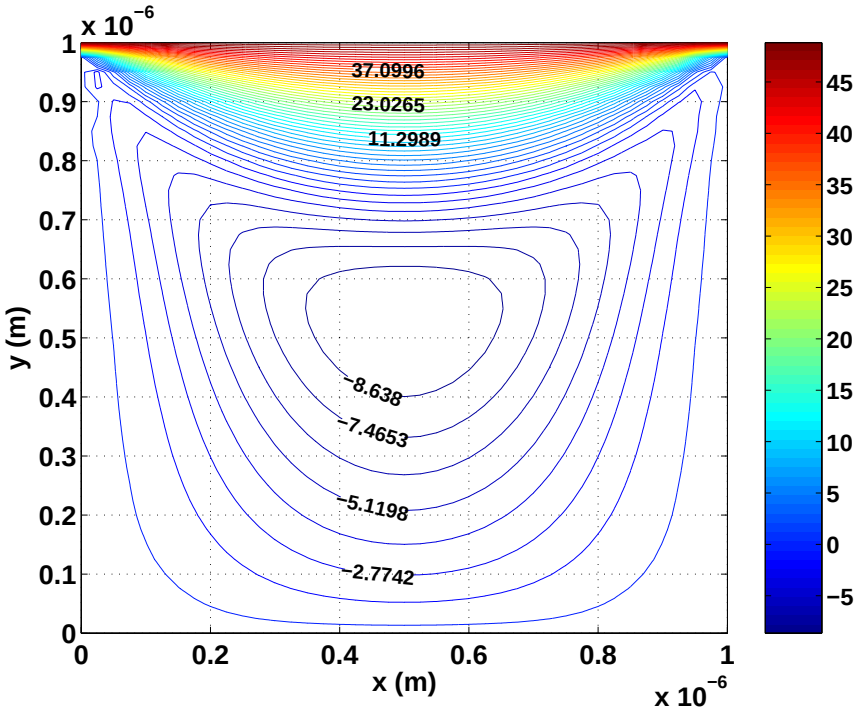

Figure 3-4: Driven cavity u–velocity contours in m/s. $Re = 0$.

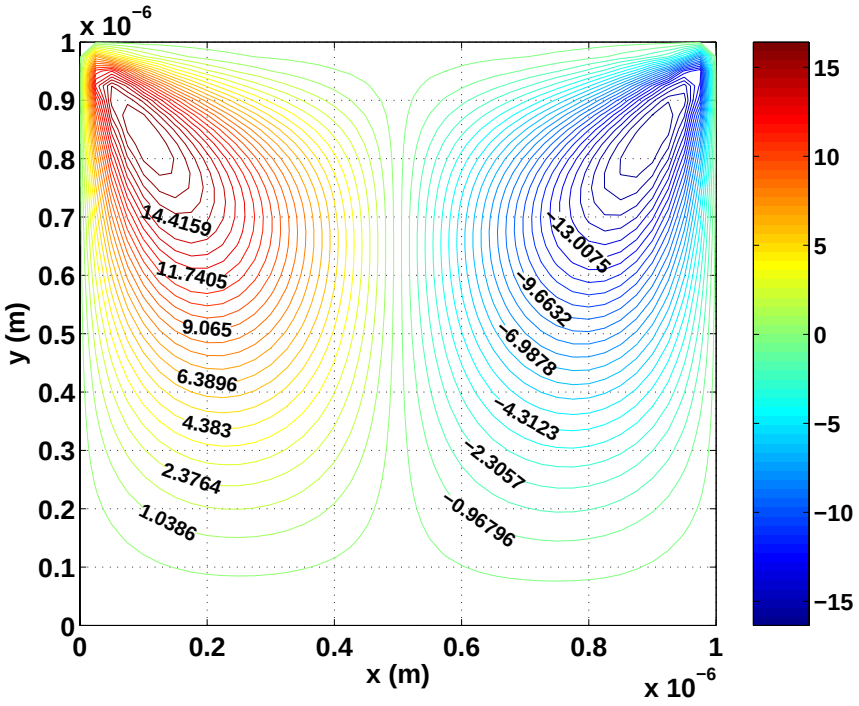

Figure 3-5: Driven cavity v–velocity contours in m/s. $Re = 0$.

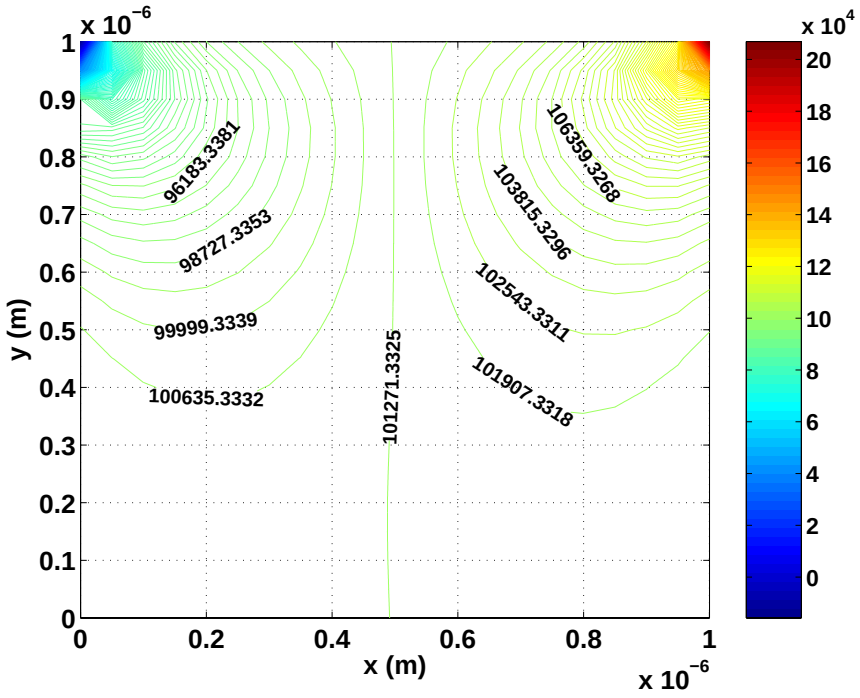

Figure 3-6: Driven cavity pressure contours in $\mathrm{N/m^2}$. $Re = 0$.

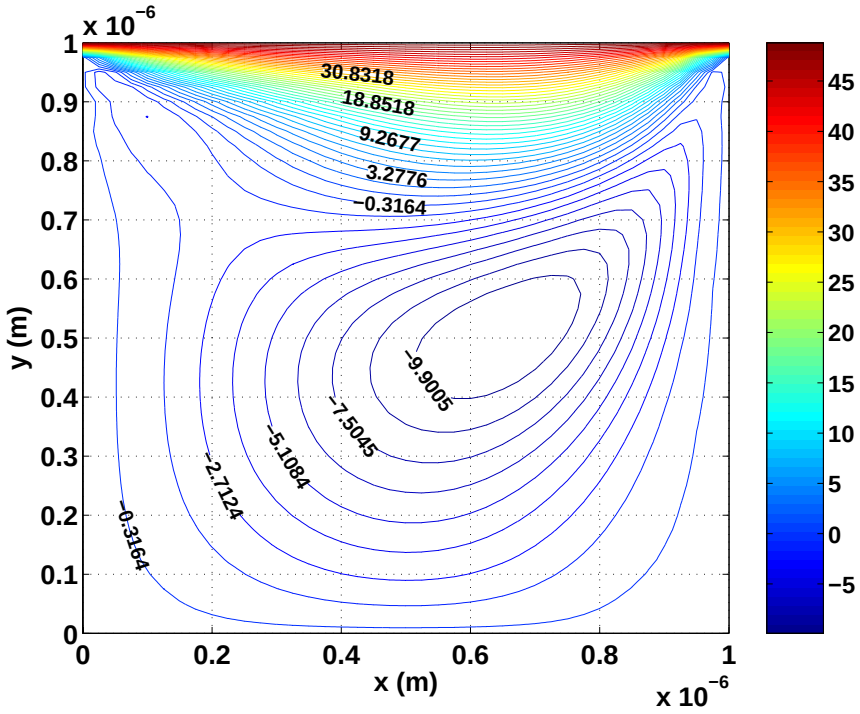

Figure 3-7: Driven cavity u–velocity contours in m/s. $Re = 100$.

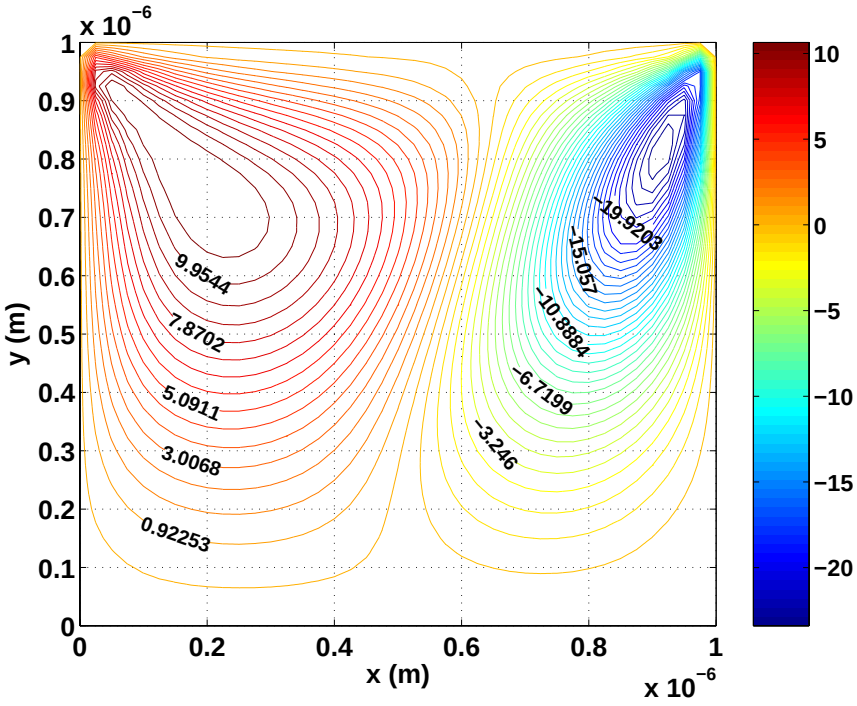

Figure 3-8: Driven cavity v–velocity contours in m/s. $Re = 100$.

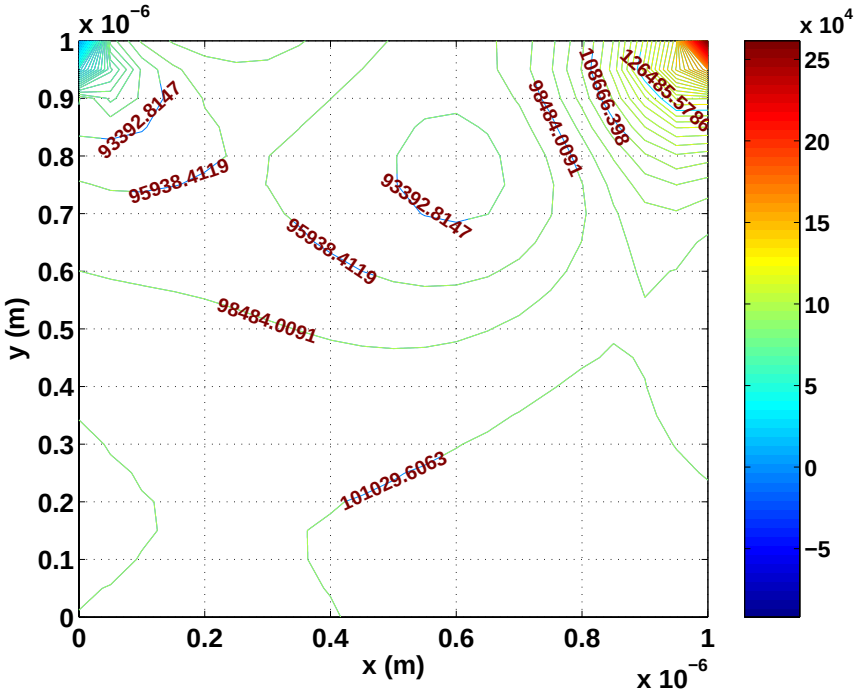

Figure 3-9: Driven cavity pressure contours in $\mathrm{N/m^2}$. $Re = 100$.

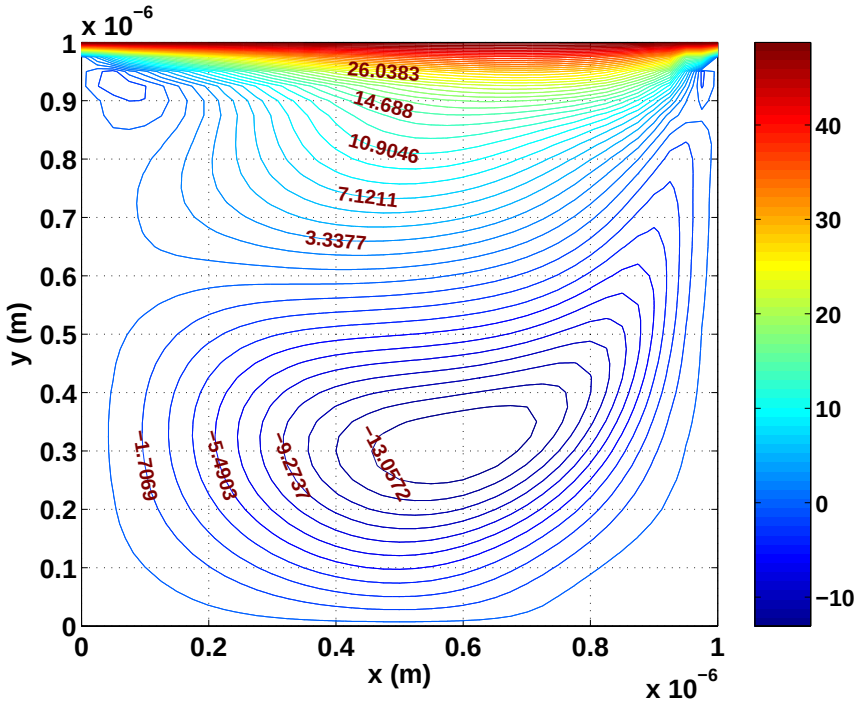

Figure 3-10: Driven cavity u–velocity contours in m/s. $Re = 400$.

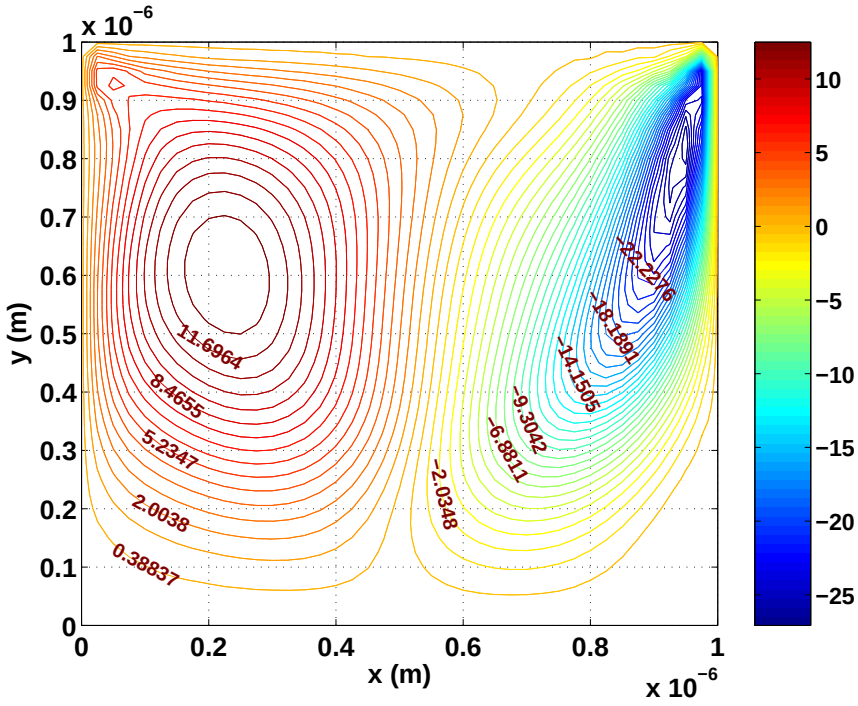

Figure 3-11: Driven cavity v–velocity contours in m/s. $Re = 400$.

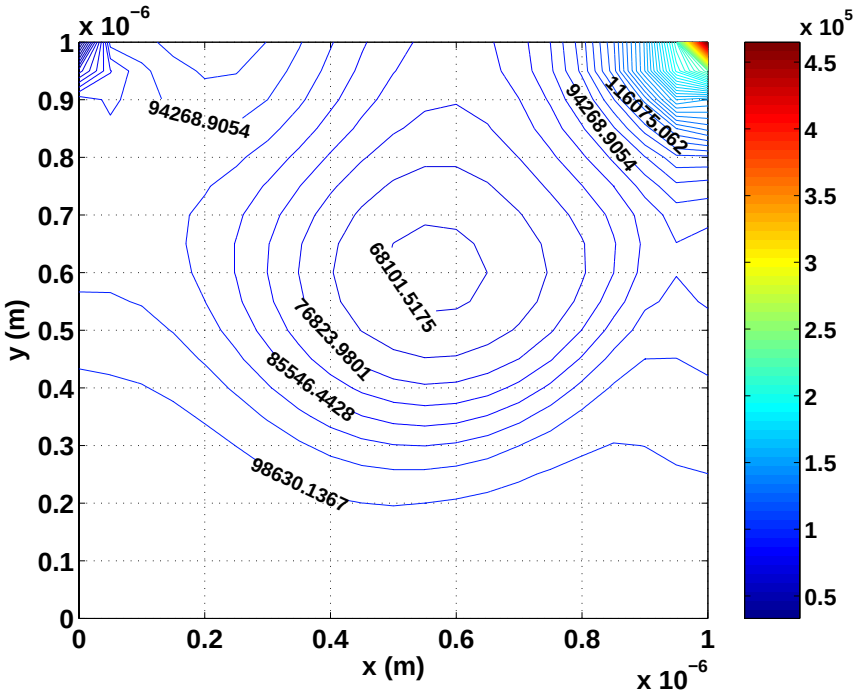

Figure 3-12: Driven cavity pressure contours in $\mathrm{N/m^2}$. $Re = 400$.

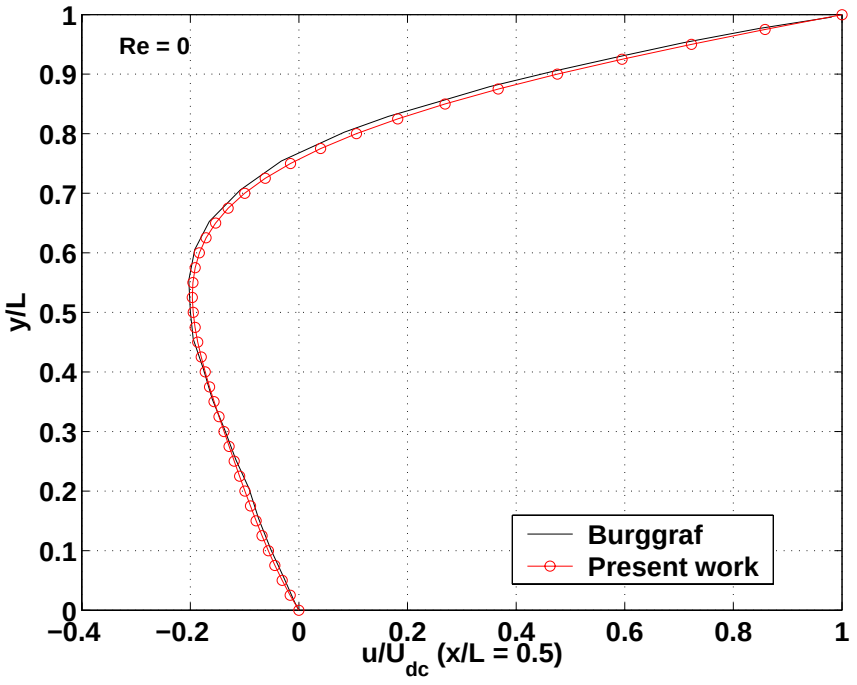

Figure 3-13: Variation of centerline u–velocity with y–coordinate at x/L=0.5. $Re = 0$.

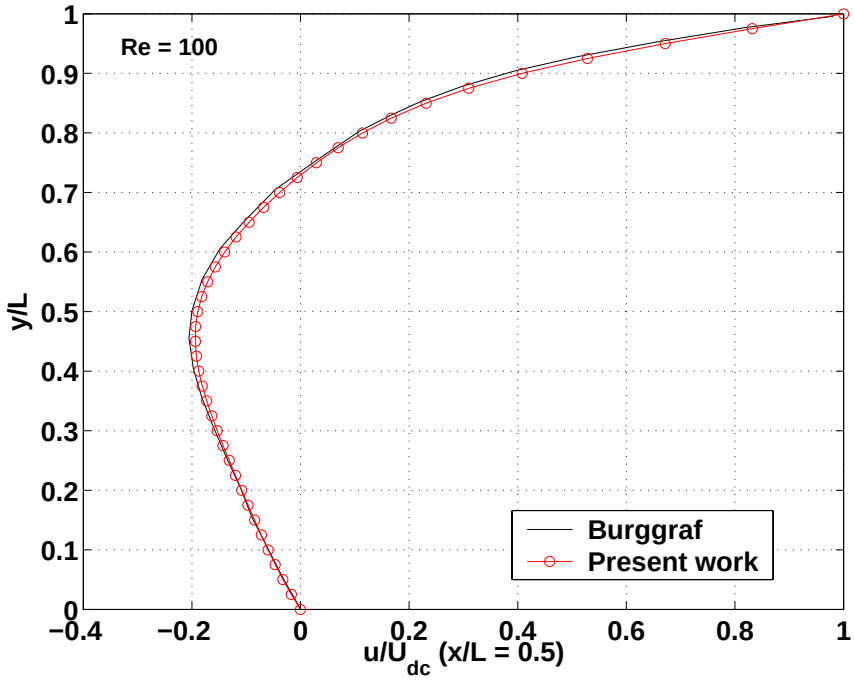

Figure 3-14: Variation of centerline u–velocity with y–coordinate at x/L=0.5. $Re = 100$.

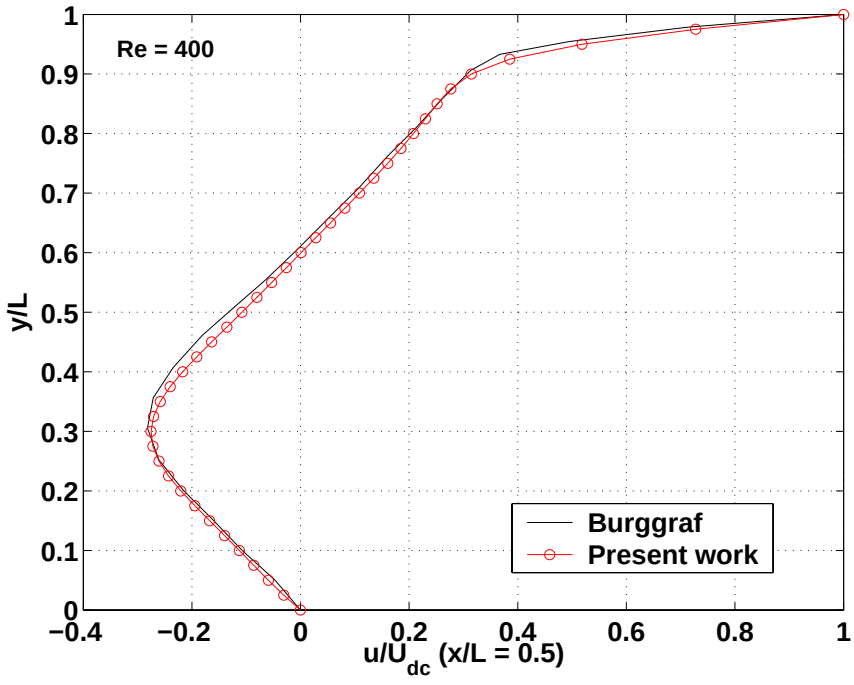

Figure 3-15: Variation of centerline u–velocity with y–coordinate at x/L=0.5. $Re = 400$.

Chapter 4

Schwarz Coupling for Steady Flows

In this Chapter a hybrid scheme for atomistic–continuum coupling of steady incompressible viscous flows is developed. This scheme uses the Schwarz alternating method to reach a steady solution through the iterative exchange of Dirichlet boundary conditions between the atomistic and continuum subdomains. The Schwarz methodology allows for time scale decoupling of the integration routines of both subdomains as only the steady state solutions in each are required during boundary condition exchange. Continuum to atomistic boundary condition imposition is performed using the Chapman–Enskog velocity distribution function in conjunction with particle reservoirs. The direct simulation Monte Carlo method and the finite element formulation described earlier are used to solve the atomistic and continuum subdomain flows respectively. The hybrid scheme is verified by solving a 2–dimensional driven cavity flow.

4.1 Introduction

The hybrid solution methodology using the Schwarz alternating method belongs to a class of domain decomposition methods that employ overlapping subdomains [85]. Consider the solution of a linear elliptic partial differential equation (PDE) for the domain $\Omega = \Omega_1 \cup \Omega_2$ in Figure 4-1. This can be written as

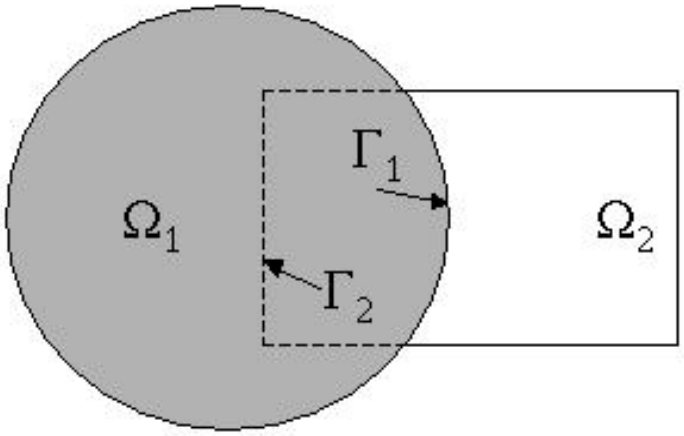

Figure 4-1: Schwarz's original figure. Adapted from [85].

$$\begin{aligned} \mathbf{Lu} &= \mathbf{f} \text{ in } \Omega, \\ \mathbf{u} &= \mathbf{g} \text{ on } \partial\Omega \end{aligned} \tag{4.1}$$

where $\mathbf{L}$ is a linear operator and $\partial\Omega$ is the boundary of Ω. The alternating Schwarz method starts with an initial guess u_2^0 for the values in Ω_2, then iteratively for $n = 1, 2, 3, ...$, solves the boundary value problem [85],

$$\begin{aligned} \mathbf{Lu_1^n} &= \mathbf{f} \text{ in } \Omega_1, \\ \mathbf{u_1^n} &= \mathbf{g} \text{ on } \partial\Omega_1 \backslash \Gamma_1 \\ \mathbf{u_1^n} &= \mathbf{u_2^{n-1}}|_{\Gamma_1} \text{ on } \Gamma_1 \end{aligned} \tag{4.2}$$

for u_1^n. This is followed by solution of the boundary value problem,

$$\begin{aligned} \mathbf{Lu_2^n} &= \mathbf{f} \text{ in } \Omega_2, \\ \mathbf{u_2^n} &= \mathbf{g} \text{ on } \partial\Omega_2 \backslash \Gamma_2 \\ \mathbf{u_2^n} &= \mathbf{u_1^n}|_{\Gamma_2} \text{ on } \Gamma_2 \end{aligned} \tag{4.3}$$

where $\Gamma_\mathbf{i}$ is part of the boundary $\Omega_\mathbf{i}$ that is interior to Ω and $\partial\Omega_\mathbf{i} \backslash \Gamma_\mathbf{i}$ represents all of the points on $\partial\Omega_\mathbf{i}$ that are not on $\Gamma_\mathbf{i}$. The Schwarz alternating method was first introduced by

Schwarz in 1870 [81] not as a numerical scheme, but rather to prove existence of a solution to Equation (4.1) in a domain in which there was no known analytical solution [85]. More recently the Schwarz method has been shown to converge for elliptic equations [61].

An illustration of the Schwarz alternating method to solve for the velocity in a pressure driven Poiseuille flow is shown graphically in Figures 4-2,4-3,4-4 adapted from [46]. Starting with a zero guess for the solution in domain 2, the first solution in domain 1 can be obtained. This provides the first boundary condition for a solution in domain 2 (Figure 4-2). The new solution in domain 2 provides an updated second boundary condition for domain 1 (Figure 4-3). This process is repeated until the solution in the overlap region matches. As seen in Figure 4-4 the solution across the complete domain rapidly approaches the steady state solution. The boundary condition iteration detailed above for continuum–continuum formulations can be applied to a heterogeneous atomistic–continuum formulation provided the solution in the overlap region is equivalent in both formulations [46]. Hadjiconstantinou and Patera [46] were the first to demonstrate the Schwarz alternating method for such an atomistic–continuum domain decomposition.

The Schwarz approach relies on the robust imposition of boundary conditions on the two subdomains. Although in continuum domains imposition of boundary conditions is well understood, in atomistic simulations this is not as straightforward. The problem arises from the fact that macroscopic boundary conditions do not uniquely determine the atomistic state since they correspond to the first few moments of an atomistic distribution function. Fortunately for gases the non–equilibrium distribution function corresponding to the continuum region is known and is referred to as the Chapman–Enskog distribution. The generation of particle velocities with this distribution is described in detail next.

4.2 Continuum to Atomistic Boundary Condition Imposition

The continuum boundary conditions are imposed on the atomistic domain utilizing particle reservoirs as shown in Figure 1-5. Particles are created in the reservoir with a spatial distribution that satisfies the continuum density field (described shortly in Section 4.2.1 and a velocity drawn from a Chapman–Enskog distribution. The imposition of density gradients derived from an incompressible solution is slightly subtle. It is required because the

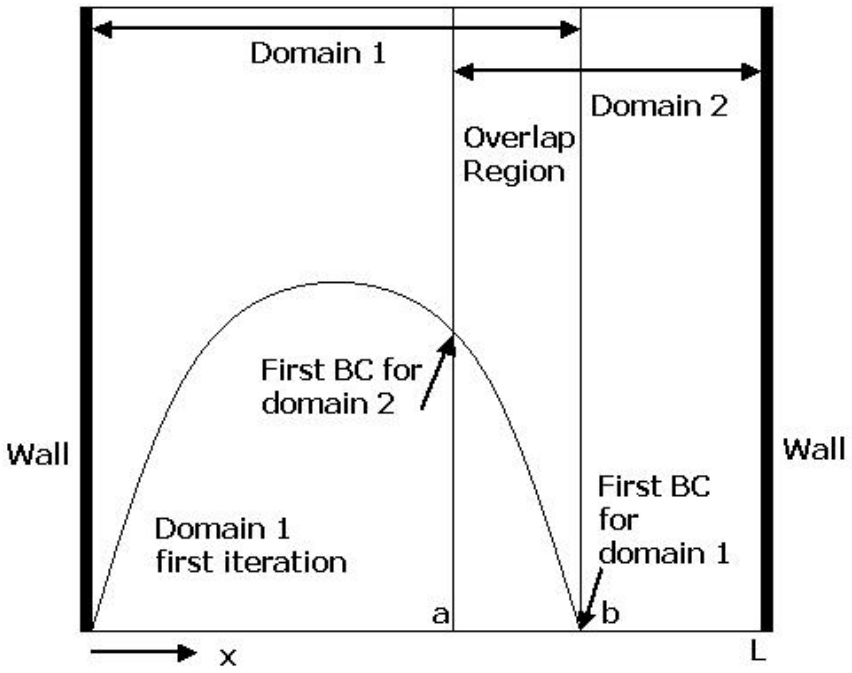

Figure 4-2: Schematic illustrating the Schwarz alternating method for Poiseuille flow. Solution at the first Schwarz iteration. Adapted from [46].

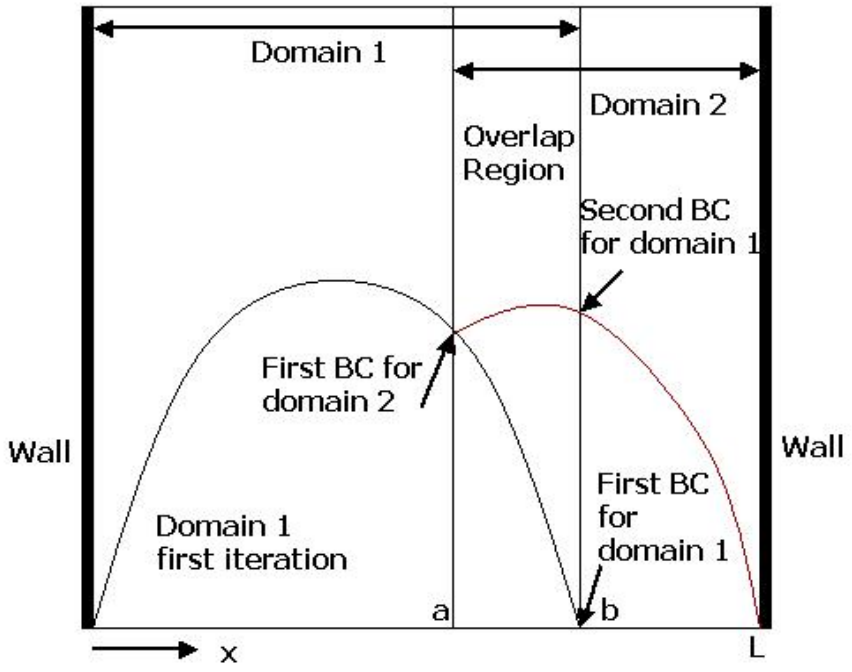

Figure 4-3: Schematic illustrating the Schwarz alternating method for Poiseuille flow. Solution at the second Schwarz iteration. Adapted from [46].

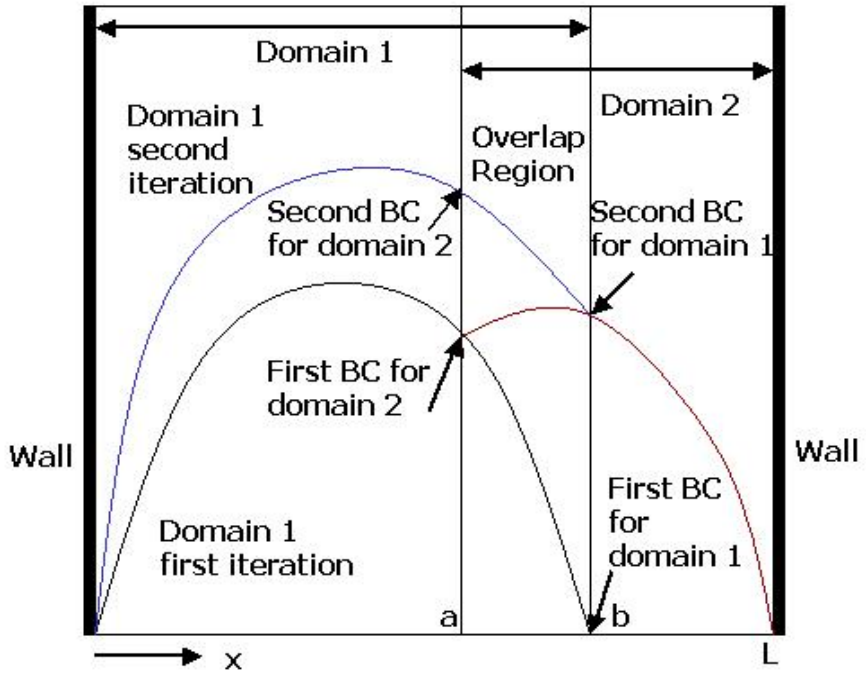

Figure 4-4: Schematic illustrating the Schwarz alternating method for Poiseuille flow. Solution at the third Schwarz iteration. Adapted from [46].

atomistic simulation, being always compressible requires the presence of density (pressure) gradients for flow to exist. The density field extracted from the pressure field of the continuum solution using the ideal gas law is found to work well. Note that isothermal conditions are assumed in this case.

The Chapman–Enskog velocity distribution function $f(\mathcal{C})$ can be written as [35],

$$f(\mathcal{C}) = f_0(\mathcal{C})\Gamma(\mathcal{C}) \tag{4.4}$$

where, $\mathcal{C} = \mathbf{C}/(2kT/m)^{1/2}$ is the normalized thermal velocity,

$$f_0(\mathcal{C}) = \frac{1}{\pi^{2/3}} e^{-C^2} \tag{4.5}$$

and,

$$\begin{aligned}\Gamma(C) = 1 &+ (q_x C_x + q_y C_y + q_z C_z)\left(\frac{2}{5}C^2 - 1\right) \\ &- 2(\tau_{xy}C_xC_y + \tau_{xz}C_xC_z + \tau_{yz}C_yC_z) \\ &- \tau_{xx}(C_x^2 - C_z^2) - \tau_{yy}(C_y^2 - C_z^2) \end{aligned} \tag{4.6}$$

with,

$$q_i = -\frac{\kappa}{P}\left(\frac{2m}{kT}\right)^{1/2}\frac{\partial T}{\partial x_i} \tag{4.7}$$

$$\tau_{ij} = \frac{\mu}{P}\left(\frac{\partial v_i}{\partial x_j} + \frac{\partial v_j}{\partial x_i} - \frac{2}{3}\frac{\partial v_k}{\partial x_k}\delta_{i,j}\right) \tag{4.8}$$

where q_i and τ_{ij} are the dimensionless heat flux and stress tensor respectively with μ, κ, P and $\mathbf{v} = (v_1, v_2, v_3)$ being the viscosity, thermal conductivity, pressure and mean fluid velocity respectively. Each particle i created in the reservoir at location $\mathbf{r}_i$, is convected with a velocity drawn from the Chapman–Enskog distribution defined by the continuum velocity and temperature field value at $\mathbf{r}_i$. Particles that enter the atomistic subdomain are retained for processing by DSMC routines. Particles that remain in the reservoir are discarded.

A scheme to spatially distribute particles in reservoirs to match imposed continuum density gradients is described next. This is followed by outline of an "Acceptance–Rejection" method to generate the Chapman–Enskog distribution. A Poiseuille flow test problem is then solved to demonstrate the efficacy of particle reservoirs for continuum boundary condition imposition.

4.2.1 Particle Generation in Reservoirs According to Imposed Continuum Density Gradients

A procedure to generate particle x, y, z coordinates according to imposed continuum density gradients was developed by Garcia [39].

Consider a linear density variation in a cell with dimensions ℓ_x, ℓ_y, ℓ_z and with ρ_0 being

the density at the center,

$$\rho(x, y, z) = \rho_0 + a_x(x - \ell_x/2) + a_y(y - \ell_y/2) + a_z(z - \ell_z/2) \tag{4.9}$$

and $a_\alpha = \partial\rho/\partial\alpha$. The total number of particles to be generated within a cell can be obtained by integrating $\rho(x, y, z)$ and dividing by the mass of a single particle. The location of the particles are then chosen at random as follows. The probability that a particle has a position $\tilde{x} = x/\ell_x$ is given by [39],

$$P(\tilde{x}) = 1 + \gamma_x(\tilde{x} - 1/2) \tag{4.10}$$

where $\gamma_x \equiv \ell_x a_x/\rho_0$ is the non–dimensional density gradient. By writing an expression for the cumulative distribution function F as

$$F(\tilde{x}) = \int_0^{\tilde{x}} P(\tilde{x})\, d\tilde{x} = \frac{1}{2}\gamma_x\tilde{x}^2 + \left(1 - \frac{1}{2}\gamma_x\right)\tilde{x} \tag{4.11}$$

and solving for $\tilde{x}$ in terms of F, it can be shown that

$$\tilde{x} = \gamma_x^{-1}\left[(\gamma_x/2 - 1) + \left[(\gamma_x/2 - 1)^2 + 2\gamma_x F\right]^{1/2}\right] \tag{4.12}$$

and that when $\gamma_x \approx 0$,

$$\tilde{x} \approx \gamma_x^{-1}\,|\gamma_x/2 - 1|\left(\frac{\gamma_x F}{(\gamma_x/2 - 1)^2}\right) = \frac{F}{1 - \gamma_x/2} \tag{4.13}$$

Hence to chose the particle x position, a random uniformly distributed value between 0 and 1 is first chosen for F. The corresponding $\tilde{x}$ is calculated using Equation (4.12) (or Equation (4.13) if $\gamma_x \approx 0$) and the particle position is set as $x = \tilde{x}\ell_x$. It can be shown further that $y = \tilde{y}/\ell_y$ can then be generated by replacing $\gamma_y/P(\tilde{x})$ in the place of γ_x in Equations (4.12) and (4.13). Finally $z = \tilde{z}/\ell_z$ is selected by replacing γ_x by $\gamma_z/P(\tilde{x}, \tilde{y})$ where $P(\tilde{x}, \tilde{y}) = 1 + \gamma_x(\tilde{x} - 1/2) + \gamma_y(\tilde{y} - 1/2)$.

4.2.2 Generation of Velocities from a Chapman–Enskog Distribution

The "Acceptance–Rejection" scheme [30] described by Garcia and Alder [35] is utilized to generate Chapman–Enskog distribution velocities for this work. In this scheme an amplitude parameter $A = 1 + 30B$ is first chosen where $B = max(|\tau_{ij}|, |q_i|)$. Next a trial velocity $\mathcal{C}_{try}$ is drawn from the Maxwell–Boltzmann equilibrium distribution function f_0 given by Equation 4.5. Note f_0 is a normal (Gaussian) distribution that can be generated using standard numerical techniques [72]. The trial velocity $\mathcal{C}_{try}$ is accepted if it satisfies $A\mathcal{R} \leq \Gamma(\mathcal{C}_{try})$ where $\mathcal{R}$ is a uniform deviate in $[0, 1)$. Otherwise a new trial velocity $\mathcal{C}_{try}$ is drawn. The final particle velocity is given by

$$\mathbf{c} = (2kT/m)^{1/2}\mathcal{C}_{try} + \mathbf{v} \tag{4.14}$$

4.2.3 Poiseuille Flow Test Problem

The reservoir boundary condition imposition technique is validated in this Section using a continuum field corresponding to a pressure driven Poiseuille flow. This test was chosen because an analytical solution is known. Boundary conditions can therefore be imposed and checked to an arbitrary degree of accuracy. A continuum solution is adequate here since the atomistic subdomain is far from any walls and thus no non–equilibrium effects beyond the Chapman–Enskog distribution will be present. The computational domain for this flow is shown in Figure 4-5. The DSMC atomistic subdomain has size $12\lambda \times 12\lambda$ while the reservoir region has a uniform width of 4λ.

The DSMC simulation is conducted using gaseous Argon with atomic mass $m = 6.63 \times 10^{-26}$kg and hard sphere diameter $\sigma = 3.66 \times 10^{-10}$m at temperature $T = 273$K. This specific system has a kinematic viscosity $\nu = 1.1688665 \times 10^{-5}\text{m}^2/\text{s}$. A total of 576 DSMC cells were used (24 in each coordinate direction) and an average of 17280 DSMC particles (30 particles per cell).

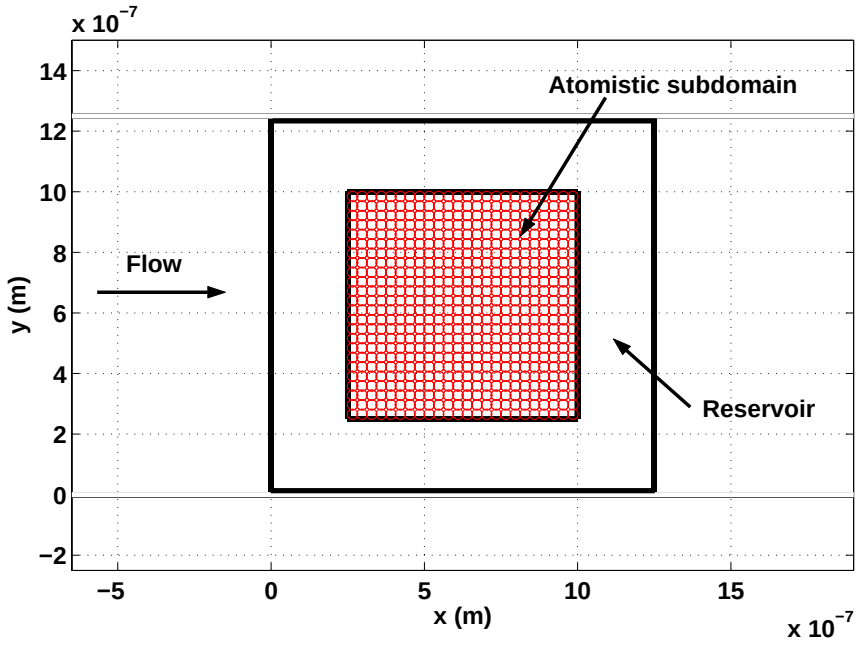

Figure 4-5: Geometry used to impose continuum boundary conditions on the atomistic subdomain using particle reservoirs.

The continuum velocity field for Poiseuille flow is given by solution of,

$$\mu \frac{\partial^2 u}{\partial y^2} = \frac{\partial P}{\partial x} \tag{4.15}$$

where μ is the fluid viscosity and P is the pressure. The analytic solution to the velocity profile is parabolic and is given by,

$$u = \frac{1}{2\mu} \frac{\partial P}{\partial x} \left(y^2 - Hy \right) \tag{4.16}$$

where H is the channel width and the velocity gradient $\partial u/\partial y$ is given by,

$$\frac{\partial u}{\partial y} = \frac{1}{2\mu} \frac{\partial P}{\partial x} \left(2y - H \right) \tag{4.17}$$

A value of $(-15.36 \times 10^{12})/(\text{ms})$ was chosen for the $(1/(2\mu))\partial P/\partial x$ prefactor in Equations (4.16) and (4.17) so that a centerline velocity of 6m/s is obtained. This in turn yields a pressure gradient $\partial p/\partial x = -6.4 \times 10^8 \text{N/m}^3$. The corresponding number density gradient $\partial n/\partial x = (1/kT)\partial p/\partial x = -1.7 \times 10^{29}/\text{m}^4$. This corresponds to a variation of the density along the channel of $\Delta n/n_0 = 0.008$ which is small. This allows us to neglect the

acceleration effects due to the pressure drop.

DSMC particles are created in the reservoir utilizing the procedure outlined in Section 4.2.1 such that the x coordinate locations are distributed to match the number density gradient obtained above. The particle y-coordinate location is distributed uniformly in the reservoir as there is no density gradient along this direction. For a given x, y location the DSMC particle velocities are then drawn from a Chapman–Enskog distribution defined by values of u and $\partial u/\partial y$ given by Equations (4.16) and (4.17). Particles created in the reservoir are advected during the "Move" routine described in Section 2.2 for a single DSMC time step. Those particles that enter the DSMC subdomain are sorted for collision purposes. Particles that remain in the reservoir, or enter the reservoir from the DSMC subdomain are discarded.

DSMC simulation results for the velocity profile at 3 stations $x = 0.36 \times 10^{-6}, 0.51 \times 10^{-6}, 0.67 \times 10^{-6}$m are shown in Figure 4-6. Good comparison is seen with the continuum result. Figure 4-7 shows the $u(y)$ mean velocity profile (averaged at each x–plane) with one standard deviation error bars. The atomistic result is within 2% of the continuum solution.

Figure 4-8 plots the convergence history for the Poiseuille flow test averaged over 225,000, 450,000 and 1,350,000 iterations respectively. The square root decay of the error with number of DSMC samples corresponds to the variance reduction of the statistical fluctuations. The error of the imposition method is small and is masked by this noise.

4.3 Driven Cavity Test Problem

The complete hybrid scheme is validated using the driven cavity test problem described in Section 3.2 over the domain outlined in Figure 4-9. The flow in the atomistic subdomain is solved using the DSMC algorithm developed in Chapter 2. Argon gas with atomic mass $m = 6.63 \times 10^{-26}$kg and hard sphere diameter $\sigma = 3.66 \times 10^{-10}$m was used for all simulations. The continuum subdomain is solved using the finite element solver based on the steady, incompressible Navier–Stokes equations described in Chapter 3.

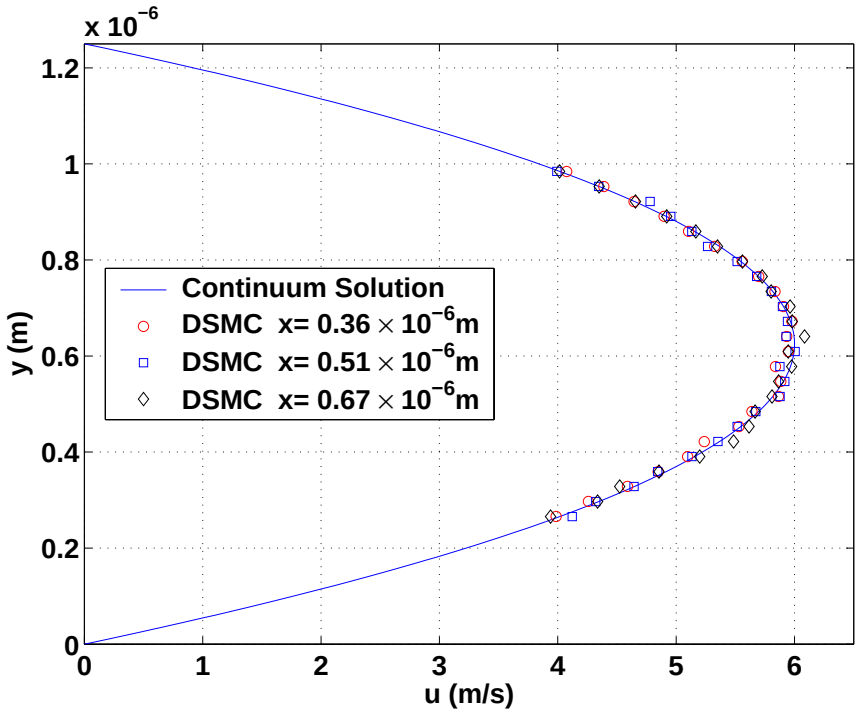

Figure 4-6: Comparison of the atomistic solution at selected x–locations with the continuum solution for Poiseuille flow. Note that acceleration effects due to the density (pressure) drop along the channel are small.

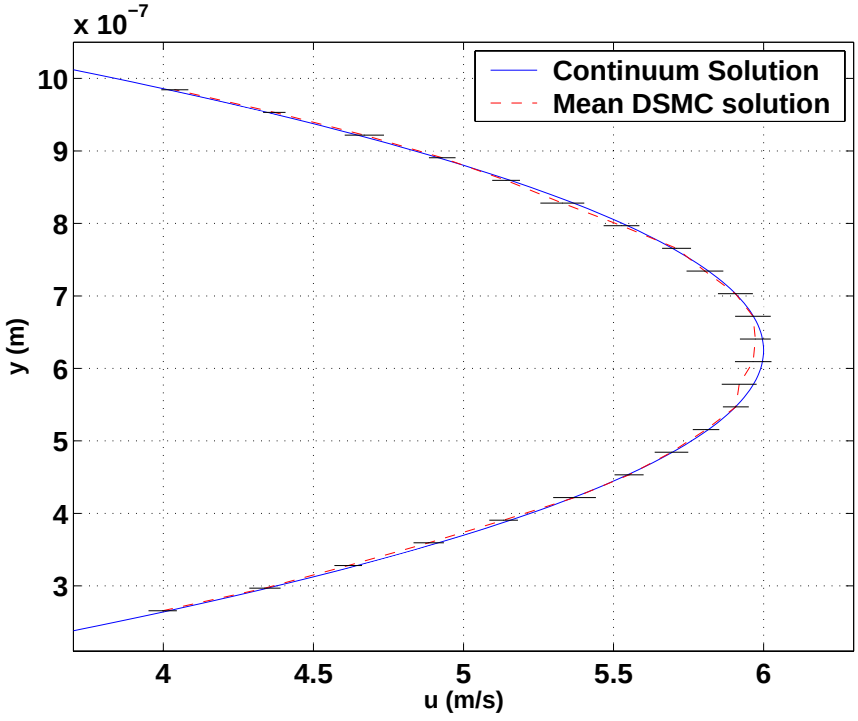

Figure 4-7: Comparison of the mean atomistic solution averaged along x–planes with the continuum solution for Poiseuille flow. Horizontal lines indicate ±1 standard deviation error bars.

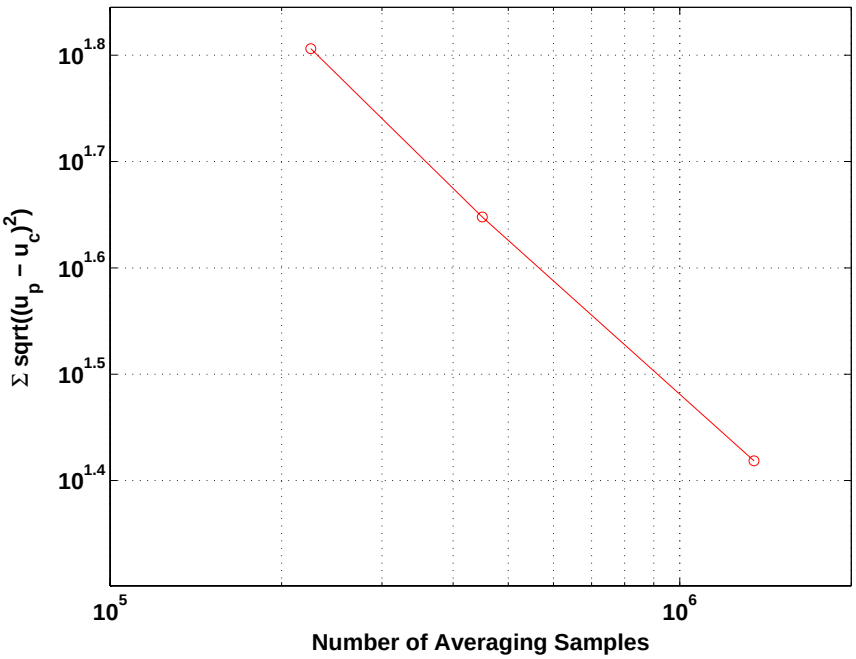

Figure 4-8: Convergence of the atomistic solution u_p to the continuum solution u_c with number of DSMC iterations. The summation is taken over the whole domain.

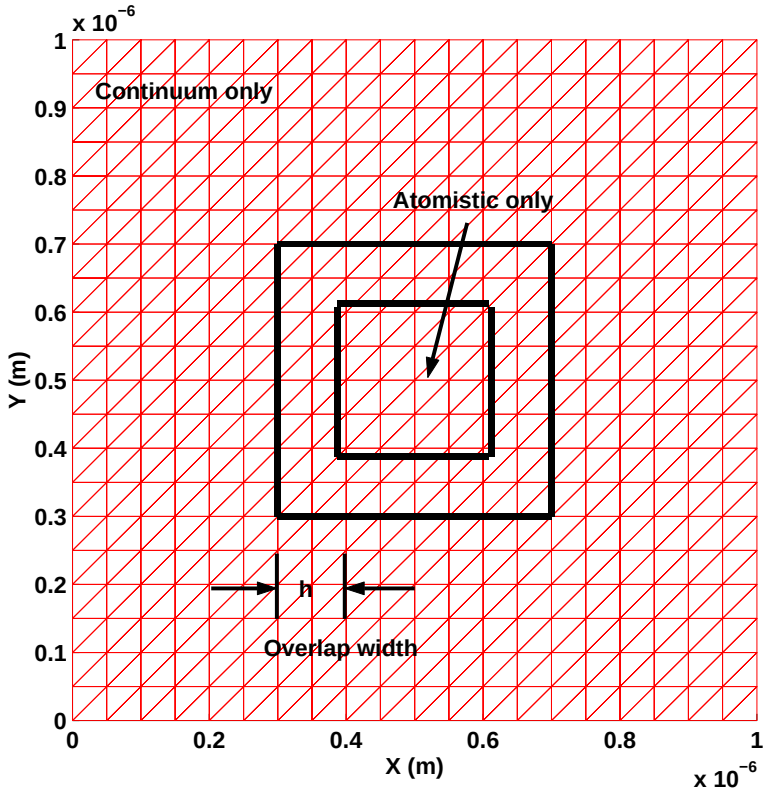

Figure 4-9: Continuum and atomistic sub-domains for driven cavity test problem.

4.3.1 Continuum to Atomistic Boundary Condition Imposition

The imposition of continuum subdomain boundary conditions on the atomistic subdomain is facilitated by a particle reservoir in the overlap region as shown in Figure 4-10. Particles are created at locations x, y within the reservoir with spatial distributions chosen according to the overlying continuum cell mean density and density gradients as described in Section 4.2.1. A continuum cell for this purpose is formed by a pair of finite element triangles. The mean density and density gradients are defined at the cell center via interpolation of the nodal pressures N_i^P using Equations 3.10– 3.12. Note the density field is obtained here from the pressure solution using the ideal gas relation as mentioned in Section 4.2. Unlike the Poiseuille flow test case in Section 4.2.3 density gradients exist in both the x and y directions for the driven cavity flow. The particle velocities $\mathbf{c_x}, \mathbf{c_y}$ are drawn from a Chapman–Enskog velocity distribution generated using the mean and gradient of velocities interpolated from cell nodes using the same quadratic interpolation functions (Equations (3.4)– (3.9)) used by the finite element solver. After particles are created in the reservoir they are convected for a single DSMC time step. Particles that enter DSMC cells are incorporated into the standard convection/collision routines of the DSMC algorithm. Particles that remain in the reservoir are discarded. Particles that leave the DSMC domain are also deleted from the computation.

4.3.2 Atomistic to Continuum Boundary Condition Imposition

The atomistic boundary conditions are imposed on the continuum subdomain more directly. The DSMC cell velocities obtained by time averaging particle velocities can be specified directly as Dirichlet conditions on the corresponding finite element nodes (see Section 3.1.5). As shown in Figure 4-10, the centers of the DSMC cells are aligned along the nodes of the finite element cells. While this alignment is not a requirement for the scheme, this helps avoid interpolation errors which may be significant due to atomistic solution fluctuations.

A correction to nodal velocities to ensure mass conservation is also performed [48]. The DSMC cell velocities normal to the atomistic subdomain boundary and which overlap with

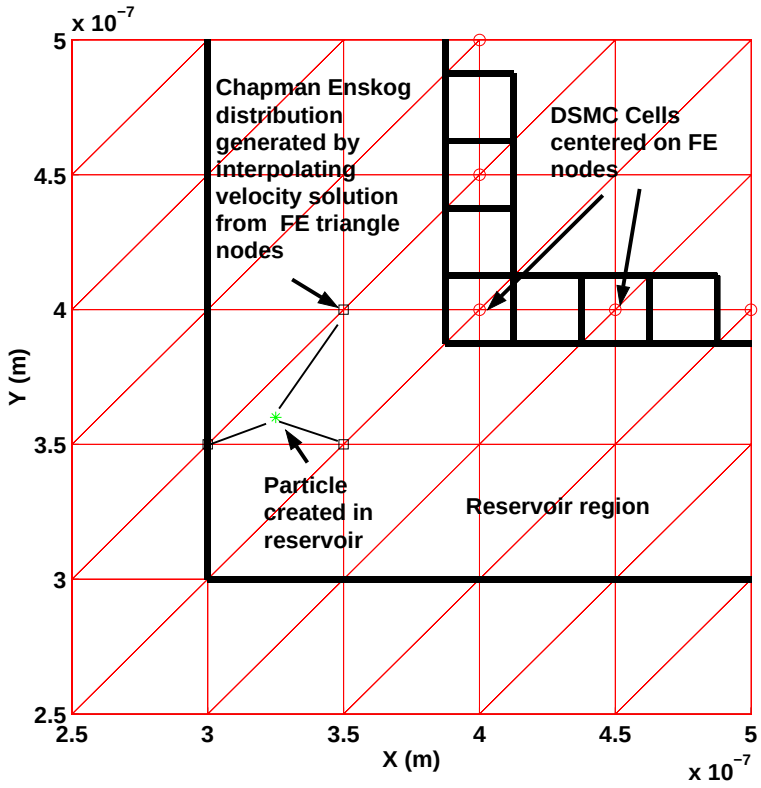

Figure 4-10: Particle reservoir in the overlap region.

the continuum element nodes $\mathbf{v_i^b}.\mathbf{n}$ are altered such that,

$$\mathbf{v_i^b}.\mathbf{n}^{corrected} = \mathbf{v_i^b}.\mathbf{n} \pm \left| 1/N_b \sum_{i=1}^{N_b} \mathbf{v_i^b}.\mathbf{n} \right| \tag{4.18}$$

where N_b is the total number of normal velocity nodes along the boundary. The sign for the summation term is chosen opposite to the sign of the unit normal $\mathbf{n}$. The discrepancy in mass flux is essentially removed equally across all normal velocity components.

4.3.3 Results

The hybrid solution is expected to recover the fully continuum solution since the atomistic subdomain is far from solid boundaries and from regions of large velocity gradients. This test therefore provides a consistency check for the hybrid scheme. Standard Dirichlet velocity boundary conditions for a driven cavity problem were applied on the continuum subdomain; the u velocity component on the left, right and lower walls were held at zero while the upper

Property	Value
Total domain width L_x	1×10^{-6} m
Total domain height L_y	1×10^{-6} m
Finite element nodes in L_x	41
Finite element nodes in L_y	41
Overlap region width h	1.0×10^{-7} m
Reservoir region width	8.75×10^{-8} m
Atomistic domain origin l_{xo}	3.875×10^{-7} m
Atomistic domain origin l_{yo}	3.875×10^{-7} m
Atomistic domain width l_x	2.25×10^{-7} m
Atomistic domain height l_y	2.25×10^{-7} m
DSMC cells in l_x	9 (2.5 cells/λ)
DSMC cells in l_y	9 (2.5 cells/λ)
Number of particles per cell	50
Argon mean free path λ	6.258×10^{-8} m
DSMC time step Δt_p	3.7×10^{-11} s
Imposed flow velocity at $y = L_y$	50 m/s
Reynolds number based on L_x	4.3
Mean temperature T	273K
DSMC time steps per Schwarz iteration	500000
No. of time steps before averaging	50000

Table 4.1: Baseline simulation parameters for the driven cavity test problem.

wall u velocity was set to 50 m/s, the v velocity component on all boundaries was set to zero. Despite the high velocity, the flow is essentially incompressible and isothermal. The pressure is scaled by setting the middle node on the lower boundary at atmospheric pressure (1.013×10^5 Pa). Additional parameters used in the simulation are listed in Table 4.1.

A zero velocity solution in the atomistic subdomain was used as an initial guess. The DSMC simulations were advanced for a total of 500,000 (18.5μs) time steps per Schwarz iteration with averaging beginning after 50,000 (1.85μs) time steps.

The convergence of the u and v velocity along the $y = 0.425 \times 10^{-6}$m plane and $x = 0.425 \times 10^{-6}$m plane respectively as a function of Schwarz iterations is plotted in Figures 4-11 and 4-12. Good comparison is achieved between the fully continuum numerical solution and the coupled hybrid solution. The continuum u velocity solution is reached to within $\pm 10\%$ at the 3rd Schwarz iteration and to within $\pm 2\%$ at the 10th Schwarz iteration. Similar convergence of the v velocity field is also observed. For a more global indication of convergence the L^2 norm of the velocity and pressure variables at each Schwarz iteration

is plotted in Figure 4-14. The velocity L^2 norm shows rapid decay and convergence. The pressure L^2 norm also shows a general decay but indicates that further iterations are required for convergence.

While the above test problem was not selected to demonstrate computational savings, substantial savings are expected in practical applications where the reduction in cost achieved by the use of the continuum description significantly outweighs the increase in cost due to the small number ($O(10)$) of Schwarz iterations required. Additional contributions to computational efficiency include the drastically reduced time to which the atomistic subdomain needs to be simulated before it reaches a steady state, and the improved computer performance for calculations with small memory requirements [2].

4.3.4 Factors Governing Convergence

A range of tests were conducted to assess the effect of Maxwell–Boltzmann based equilibrium distribution particle reservoirs (i.e., equivalent to ignoring gradient information in the overlying continuum solution), the number of DSMC time steps per Schwarz iteration and the overlap region width on the convergence of the coupling scheme. Results from these tests are plotted in Figure 4-14 and Figure 4-13. The following observations can be made from these plots:

1. The velocity and pressure error norms are one order of magnitude larger when a Maxwell–Boltzmann reservoir is used.

2. Halving the number of DSMC time steps per Schwarz iteration (via advancing the DSMC solution to 275,000 time steps and averaging after 50,000) has an insignificant effect on the convergence of the velocity L^2 norm. The pressure L^2 norm tracks the baseline solution for 3 Schwarz iterations but then fluctuates above the baseline solution.

3. Convergence of the velocity field is only weakly coupled to the overlap region width h in the range 0.8λ–1.6λ considered. A similar conclusion was reached by Aktas and Aluru [2]. The pressure field shows greater sensitivity to h but no significant differences in convergence can be seen.

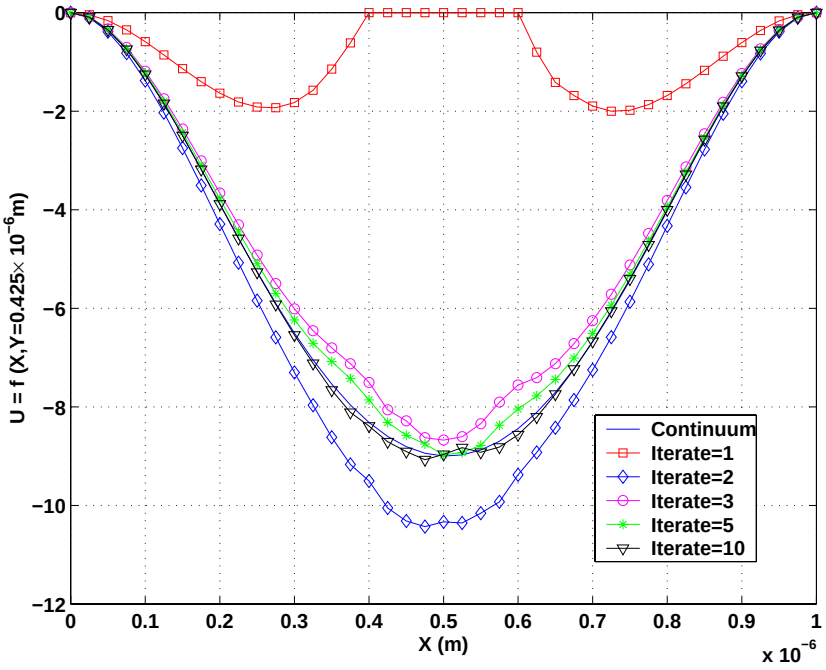

Figure 4-11: Convergence of the u velocity component with successive Schwarz iterations.

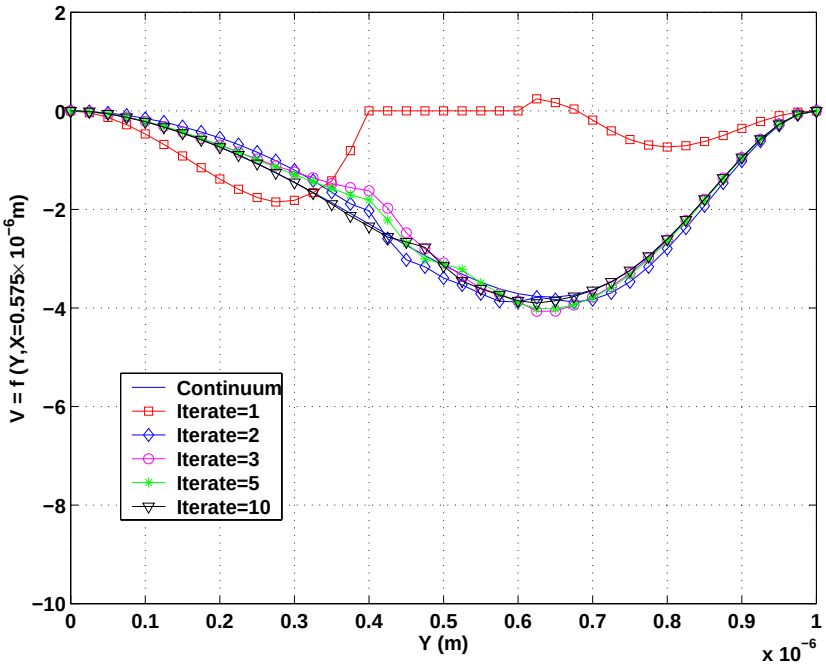

Figure 4-12: Convergence of the v velocity component with successive Schwarz iterations.

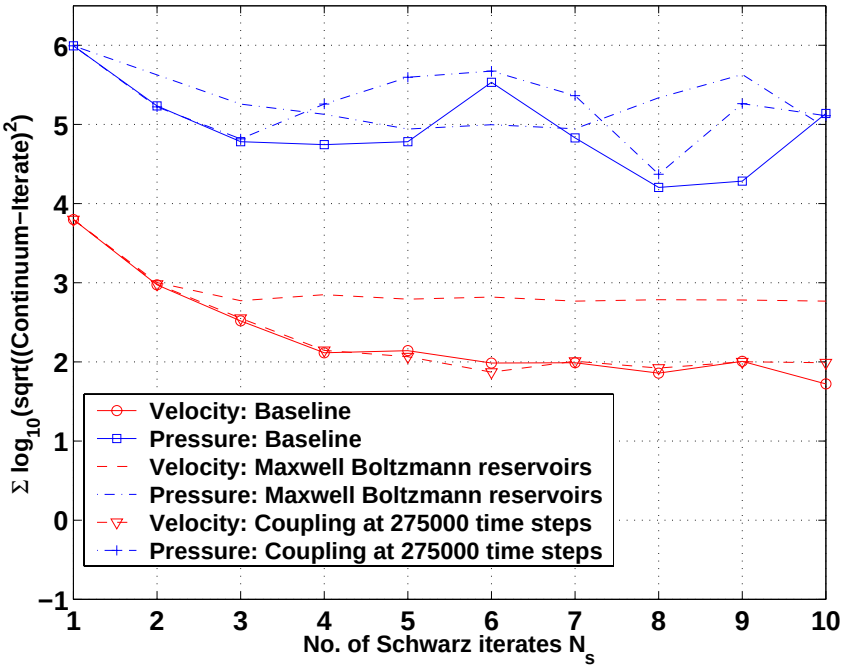

Figure 4-13: Comparison of the convergence of the velocity and pressure fields with Schwarz iterations. The velocity norm is constructed using the sum of both u and v velocities. The summation is taken over the complete domain.

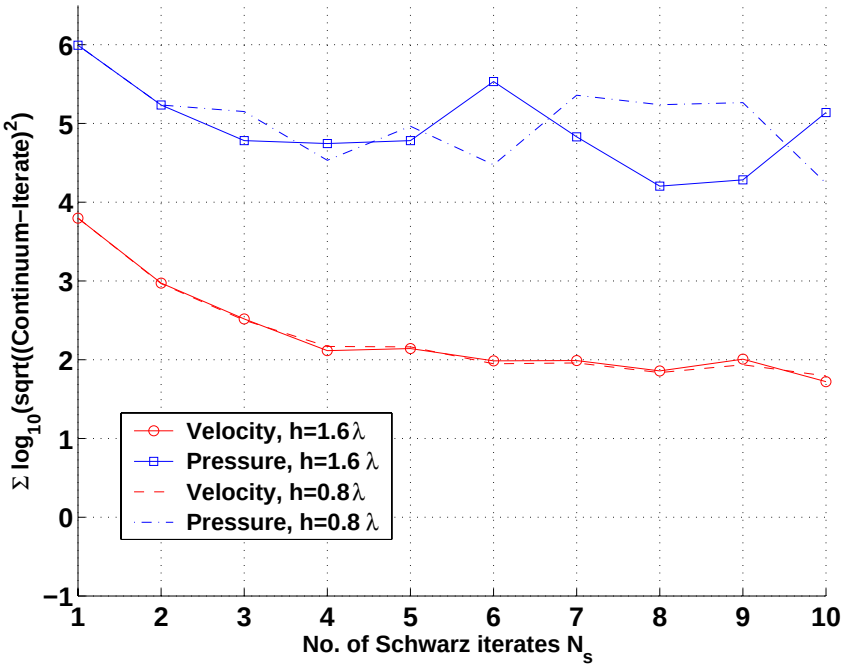

Figure 4-14: Comparison of the convergence of the velocity and pressure fields with Schwarz iterations. The velocity norm is constructed from the sum of both u and v velocities. The summation is taken over the complete domain.

4.4 Conclusions

A hybrid atomistic–continuum scheme has been developed to couple a steady, incompressible Navier–Stokes description of a continuum field with an atomistic description of a dilute gas. Coupling of the atomistic–continuum subdomains is achieved by exchange of boundary conditions via a Schwarz alternating method. Continuum subdomain boundary conditions are imposed on the atomistic subdomain using particle reservoirs based on the Chapman–Enskog velocity distribution. The atomistic subdomain boundary conditions are imposed on the continuum subdomain via simple averaging. The following conclusions have been reached in this study:

1. The use of Chapman–Enskog distributions significantly improves the accuracy of the solution compared to Maxwell–Boltzmann equilibrium distributions.

2. The Schwarz coupling scheme applied to a two–dimensional driven cavity flow at Reynolds number 4.3 converges to within $\pm 2\%$ of the fully continuum solution after 10 Schwarz iterations.

Chapter 5

Schwarz Coupling for Unsteady Flows

In this Chapter a hybrid atomistic–continuum formulation for unsteady, incompressible flows is developed using a coupling approach based on the Schwarz alternating method. An impulsive Couette flow test problem is used to validate the hybrid scheme. Finally, a method to help reduce computational costs through limited ensemble averaging is presented.

5.1 Introduction

In Chapter 1 the importance of avoiding time explicit coupling methods for *steady* incompressible flows was highlighted. The time implicit Schwarz coupling method has a clear advantage here. For the case of *unsteady* incompressible flows however, the question of the most appropriate coupling approach is not clear and may be problem dependent. Unless time coarse–graining techniques are developed for integrating the atomistic solution, large, low–speed, unsteady problems will remain too expensive to be feasible by either method. If we assume that the atomistic computations are feasible by explicit integration to the global time of interest the question of which is the most appropriate coupling approach arises.

We begin by describing a simple hybrid method based on a combined explicit/implicit approach for domain decomposition proposed by Dawson et.al [27] and Dawson and Dupont [28]. The basic approach used here is illustrated with respect to a 1–dimensional example in Figure 5-1. A distinct interface is created between the left subdomain and right subdomain.

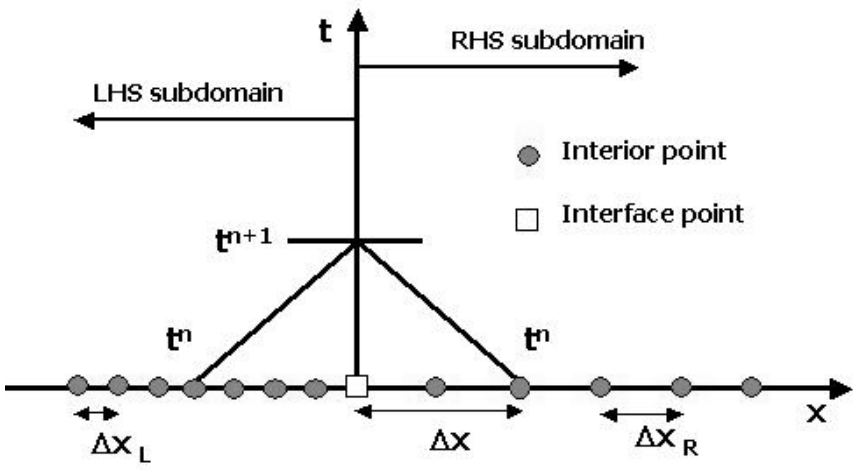

Figure 5-1: Explicit/Implicit domain decomposition stencil.

The solution at the interface point at time t^{n+1} is first obtained explicitly using values borrowed from both subdomains at time t^n. The solution at interior points within the subdomains can then be integrated implicitly to t^{n+1} using the interface value determined at t^{n+1}. The subdomain solutions can then be used to advance the interface to the next time level.

The variation of the maximum error of the explicit/implicit coupling scheme for a hybrid continuum–continuum solution for impulsive Couette flow is shown in Figure 5-2. Note the maximum explicit time step $\Delta t_{explicit}$ to advance the interface is limited by the width Δx of the stencil by the stability condition,

$$\Delta t_{explicit} \leq \frac{\Delta x^2}{2\nu} \tag{5.1}$$

where ν is the kinematic viscosity. Larger time steps are possible however with a larger error penalty. The time step restriction of the explicit/implicit coupling approach although constrained by stability requirements is less severe than that which comes from a fully explicit method [28].

The use of the explicit/implicit coupling technique was considered for atomistic–continuum coupling but was ultimately rejected on grounds of lack of generality when used for solving the more complex Navier–Stokes system. Explicit time marching of Navier–Stokes equations on a sharp interface could also pose severe numerical implementation constraints, in

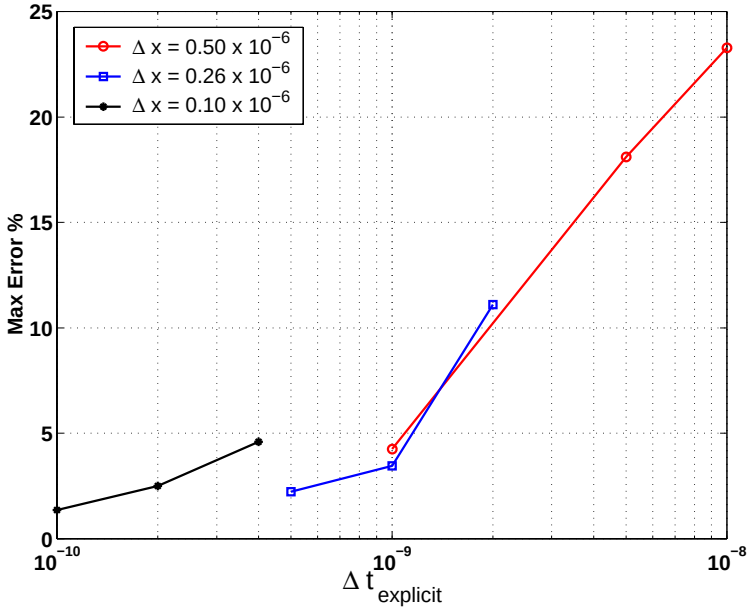

Figure 5-2: Variation of the maximum error of the explicit/implicit hybrid scheme as a function of stencil width Δx (m) and time step $\Delta t_{explicit}$ (s).

particular regarding appropriate pressure and velocity boundary conditions at low Reynolds numbers. The development of a fully implicit Schwarz–type coupling technique was therefore considered instead. As detailed shortly the Schwarz method offers two advantages compared to time explicit coupling approaches. First the time scale decoupling properties of the approach are manifested by the ability to couple only at the time where solutions are required. This not only allows the use of optimal time steps in each subdomain but also the use of acceleration methods such as the limited ensemble approach to gain an efficiency advantage. The second advantage arises from the fact that Schwarz coupling using state variables provides cost savings over traditional flux based coupling schemes vis-á-vis noise concerns related to the atomistic solution as discussed earlier in Section 1.2.1.

5.2 Unsteady Schwarz Coupling

The Schwarz alternating method can be extended to couple time unsteady flows to some time t^n by exchanging boundary condition information similar to steady flow coupling. As shown schematically in Figure 5-3 an overlap region between the subdomains facilitates information exchange in the form of Dirichlet boundary conditions. Unlike the steady flow

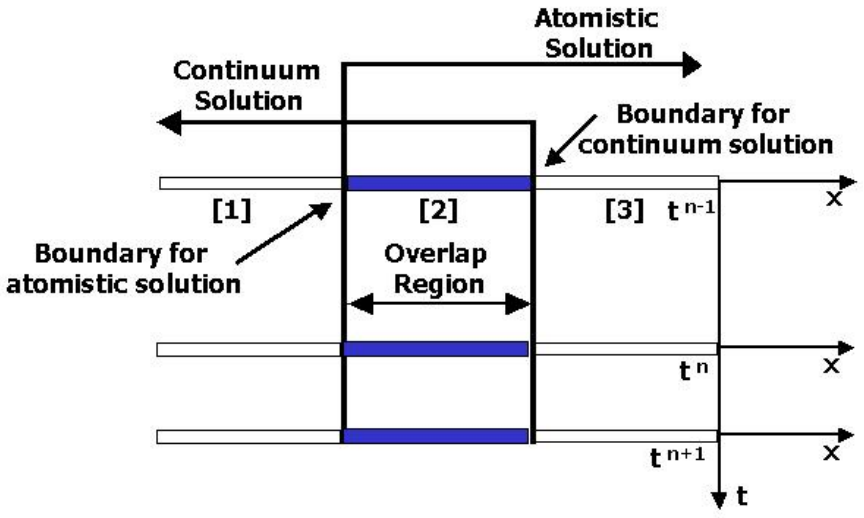

Figure 5-3: Schematic of the unsteady Schwarz alternating method.

case however successive Schwarz iterations are used to converge the solution to a given time t^n. The converged solution at t^n forms the initial condition for subsequent Schwarz iterations to advance the solution to time level t^{n+1}. The unsteady Schwarz scheme still allows for time scale decoupling; each subdomain can be advanced at the local most favorable time step and the choice of t^{n+1} is arbitrary. The computational cost of performing multiple Schwarz iterations per time level is thus partially offset by the ability to implicitly advance to the time of interest without the need for explicit coupling at previous times. Note the steady Schwarz method can be considered a particular instance of the unsteady Schwarz method as $t^n \rightarrow \infty$, or steady state.

The algorithm schematic for the unsteady Schwarz scheme is shown in Figure 5-4. An outer time step iteration loop 1 is added to the Schwarz iteration performed within loop 2. Implementation of the unsteady Schwarz method requires 2 additional constructs not present in the steady scheme; a) ensemble averaging of the unsteady atomistic subdomain solution and b) time interpolation of solutions between atomistic and continuum subdomains to allow for different time steps in these subdomains.

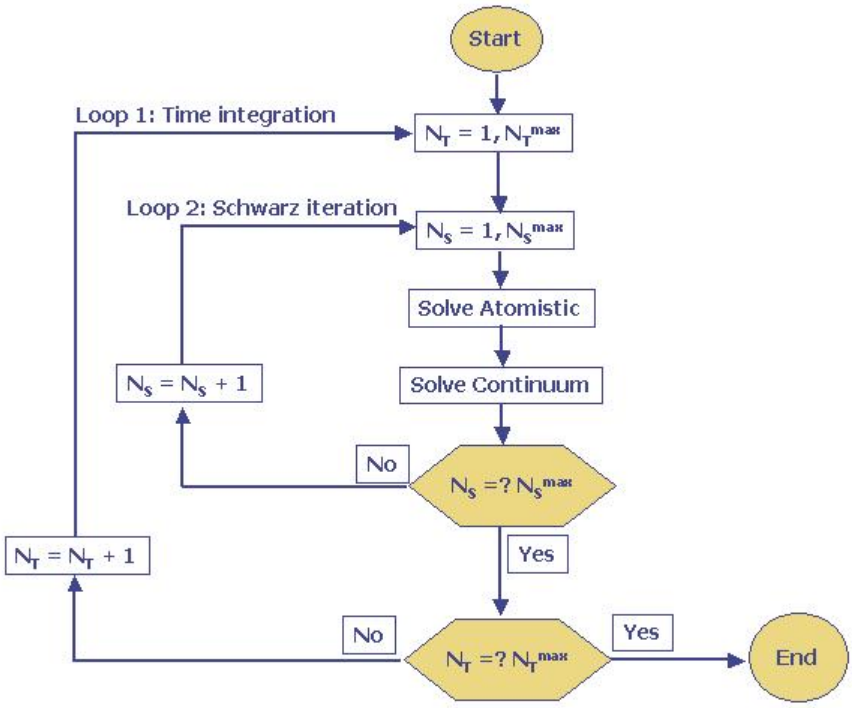

Figure 5-4: Unsteady Schwarz algorithm schematic. N_T is the time step integration counter and N_s is the Schwarz iteration counter.

5.2.1 Particle Ensembles

In the steady flow case time averaging of the atomistic solution after the latter has reached steady state was performed to help reduce the effect of statistical fluctuations. The relative statistical error for an averaged quantity defined by the ratio RMS/mean, where RMS is the root mean square value, decreases as

$$\text{RMS/mean} = \frac{1}{\sqrt{N_c N_T^{max}}} \tag{5.2}$$

where N_c is the average number of particles in a cell and N_T^{max} is the total number of samples taken [32]. However, if the samples taken are not statistically independent (for example, if time–averaging the time between samples is shorter than the correlation time) N_T^{max} is the number of *independent* samples.

For unsteady flows time averaging is not feasible for reducing the statistical error as the hydrodynamic field is evolving as a function of time. An alternative approach is to use an ensemble of calculations. For a time–unsteady flow, the solution at any given time t^n is then

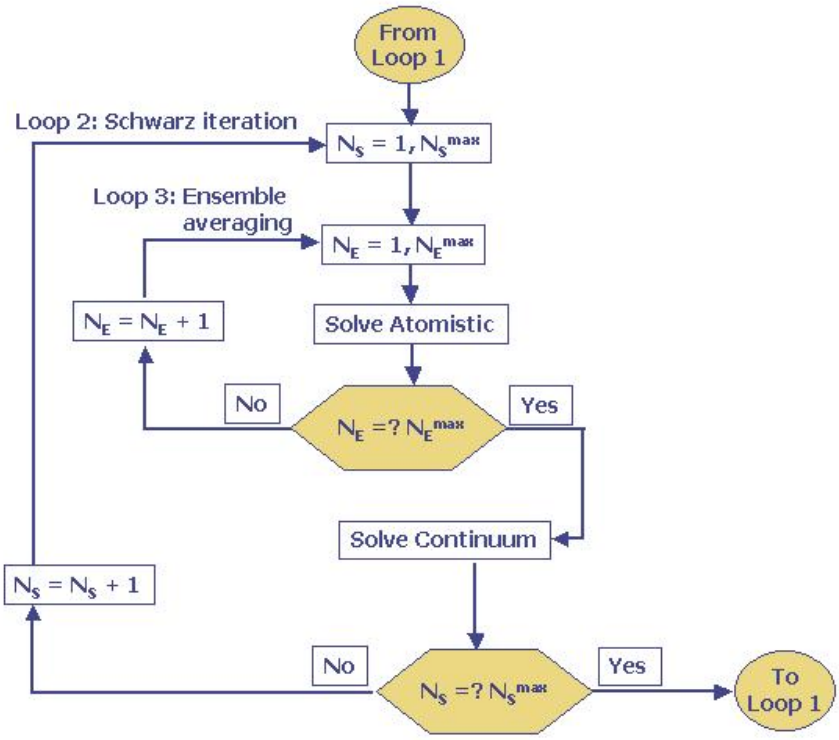

Figure 5-5: Unsteady Schwarz algorithm schematic. N_s is the Schwarz iteration counter and N_E is the ensemble averaging counter. Loop 1 corresponds to the time iteration loop in Figure 5-4.

obtained by averaging over the ensemble of identical calculations. Ensemble averaging is essential to ensure the atomistic solution is accurately determined. The associated statistical error now decays as $1/\sqrt{N_c N_E^{max}}$ where N_E^{max} is the total number of ensembles.

For the unsteady hybrid scheme, particle ensemble averaging routines are embedded within the Schwarz iteration loop as shown in the algorithm schematic in Figure 5-5.

5.2.2 Time Interpolation

A distinctive advantage of steady Schwarz coupling is its ability to decouple time scales; the time step for the continuum subdomain Δt_c is often larger than the time step for the atomistic subdomain Δt_p. Similar time scale decoupling is also possible using unsteady Schwarz coupling. For the case where $\Delta t_c > \Delta t_p$, the boundary values from the continuum solutions must be interpolated to the atomistic subdomain as shown schematically in Figure 5-6, to ensure the atomistic subdomain solution has the most accurate continuum boundary conditions during advance to any time level t^{n+1}. Note that during time advance

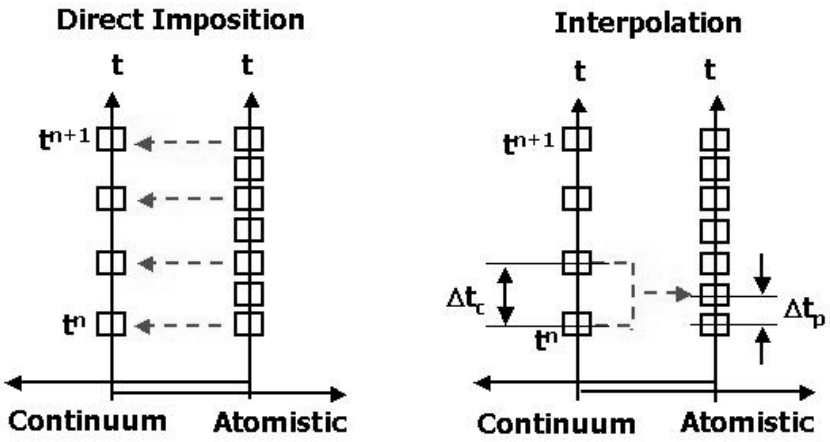

Figure 5-6: Interpolation of boundary conditions.

of the continuum subdomain, direct imposition of the atomistic subdomain boundary condition is possible provided the continuum subdomain time step is an integer multiple of the atomistic subdomain time step.

The effectiveness of linear time interpolation of the continuum boundary condition is assessed next using a hybrid continuum–continuum scheme using unsteady Schwarz coupling. The continuum–continuum domain decomposition helps evaluate the time interpolation routines independent of the ensemble averaging required for an atomistic–continuum formulation and hence in the absence of statistical fluctuations which make quantitative comparison difficult. The impulsive Couette flow shown in Figure 5-7 is used as a test problem. The wall at $x = L$ moves with velocity V_o at time $t = 0$ while the wall at $x = 0$ is held stationary. The hybrid scheme consists of 2 continuum subdomains I and II extending from $x = 0, b$ and from $x = a, L$ respectively with overlap width h.

The resulting flow is obtained by solution of a diffusion equation for y–momentum,

$$\frac{\partial v}{\partial t} - \nu \frac{\partial^2 v}{\partial x^2} = 0 \; x \in (0, L), \; t \in (0, T) \tag{5.3}$$

where $\nu = \mu/\rho$ is the kinematic viscosity. This equation can be solved numerically using an implicit backward difference scheme (i.e. Backward Euler),

$$\partial_{t,\Delta t} v_i^n - \partial^2_{x,\Delta x} v_i^n = 0 \tag{5.4}$$

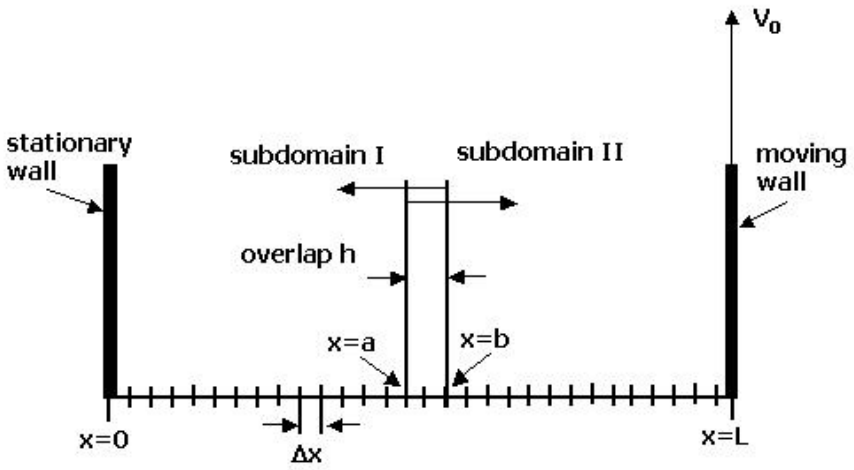

Figure 5-7: Computational domain for the impulsively started Couette flow test problem.

where,

$$\partial_{t,\Delta t} v(x,t) = \frac{v(x,t) - v(x,t-\Delta t)}{\Delta t} \tag{5.5}$$

$$\partial^2_{x,\Delta x} v(x,t) = \frac{v(x-\Delta x,t) - 2v(x,t) + v(x+\Delta x,t)}{\Delta x^2} \tag{5.6}$$

Here Δt is the time step and Δx is the spatial discretization. Equation (5.4) is used in both subdomains I and II. In this test problem, subdomain II is advanced at 1/10th the time step of subdomain I. The LHS boundary condition for subdomain II, $v_{II}(a,t)$ is linearly interpolated from the subdomain I solution as follows,

$$v_{II}(a,t^k) = v_I(a,t^i) + \frac{(k-pi)}{p}\left(v_I(a,t^{i+1}) - v_I(a,t^i)\right) \text{ where } t^i < t^k \leq t^{i+1} \tag{5.7}$$

Here $p = \Delta t_I / \Delta t_{II}$, and i, k are the indices of the time step used in subdomains I and II respectively. The RHS boundary condition for subdomain I, $v_I(b,t)$ is obtained by direct imposition of the subdomain II solution as follows,

$$v_I(b,t^i) = v_{II}(b,t^k) \text{ where } k = pi \tag{5.8}$$

Additional constants for the impulsive Couette flow test are listed in in Table 5.1.

Property	Value
Overlap width h	0.06×10^{-6} m
Boundary a	0.94×10^{-6} m
Boundary b	1.00×10^{-6} m
Domain Length L	2.00×10^{-6} m
Wall velocity V_0	30 m/s
Kinematic viscosity	$1.1688665 \times 10^{-5}\text{m}^2/\text{s}$
Subdomain I time step	$\Delta t_I = 1 \times 10^{-10}$ s
Subdomain I space step	$\Delta x_I = 2 \times 10^{-8}$ m
Subdomain II time step	$\Delta t_{II} = 1 \times 10^{-11}$ s
Subdomain II space step	$\Delta x_{II} = 2 \times 10^{-8}$ m
Schwarz iterations / Δt_I	10

Table 5.1: Properties of hybrid continuum–continuum scheme used for the impulsive Couette flow test problem.

The velocity profiles predicted by the hybrid scheme are plotted in Figure 5-8 together with a solution obtained by numerical integration of Equation (5.3) in a single domain with $\Delta x = 2 \times 10^{-8}$m and $\Delta t = 1 \times 10^{-11}$s (referred to here as the exact solution). The hybrid scheme velocity profiles are in good agreement with the exact solution. The effect of the overlap region width h on convergence of the $t = 4 \times 10^{-8}$s velocity profile to the exact solution is plotted in Figure 5-9 as a function of the number of Schwarz iterations. The number of Schwarz iterations for convergence decreases by almost a factor of 4 as the overlap region width increases by a factor of 2. Note that the error saturates after a number of iterations. This is due, as discussed below, to the boundary condition interpolation.

The convergence of the velocity profile at time $t = 4 \times 10^{-8}$s to the exact solution as a function of Schwarz iterations and interpolation scheme is plotted in Figure 5-10. The linearly interpolated boundary condition solution converges after approximately 5 Schwarz iterations. The velocity solution using stepwise boundary condition interpolation (i.e. $v_{II}(a, t^k) = v_I(a, t^{i+1})$ for $pi < k \leq p(i+1)$) also converges but with larger deviation. The use of equal time steps $\Delta t = 1 \times 10^{-11}$s in both subdomains, i.e. where direct boundary condition imposition is possible between subdomains $I \rightarrow II$ and $II \rightarrow I$ shows the best performance. This final result verifies consistency of the unsteady Schwarz coupling as the time interpolation between the subdomains is removed. While use of equal time steps in both subdomains results in greater accuracy this must be weighed with the benefit of reduced hybrid simulation cost through time step decoupling. Linear interpolation of

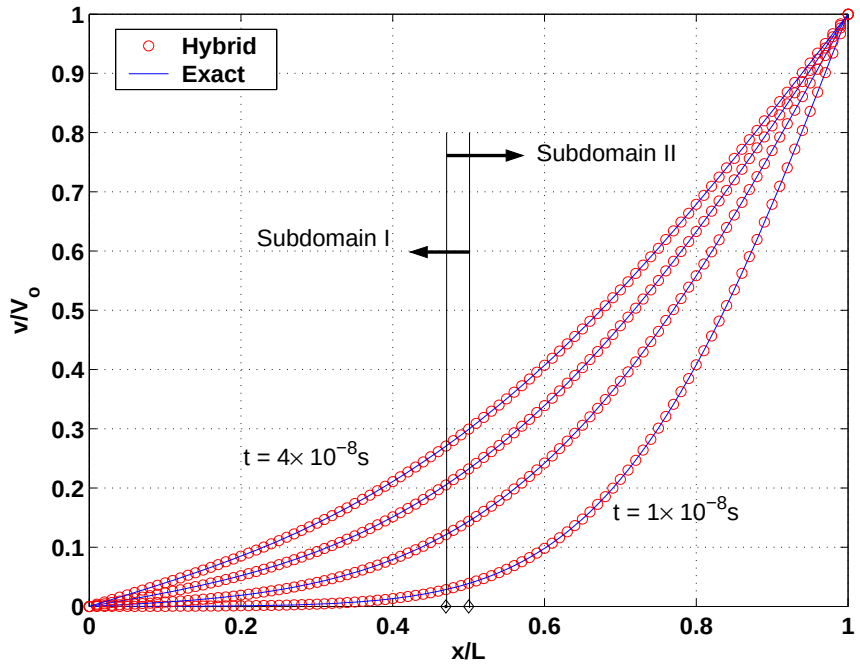

Figure 5-8: Comparison of the hybrid continuum–continuum solution for the impulsively driven Couette test problem with the exact solution. Overlap $h = 6 \times 10^{-8}$m. Profiles are shown for $t = 1 \times 10^{-8}$s to 4×10^{-8}s in steps of 1×10^{-8}s.

the boundary condition provides reasonable balance between the two constraints in this case. Application of unsteady Schwarz coupling to hybrid atomistic–continuum schemes is described next.

5.3 Impulsive Couette Flow Test Problem

A hybrid atomistic–continuum scheme using unsteady Schwarz coupling is validated in this section for the 1–dimensional impulsive Couette flow test problem shown in Figure 5-7. The subdomains I and II correspond to the continuum and atomistic subdomains respectively.

The continuum solution is obtained by solving Equation (5.3) for the y–momentum diffusion using the implicit backward difference scheme detailed in Equation (5.4). The atomistic subdomain is solved using DSMC. The imposition of continuum boundary conditions on the atomistic subdomain is facilitated by particle reservoirs as described for the steady flow case. Particles are created in the reservoir with a uniform distribution in the x–coordinate direction and a velocity drawn from a Chapman–Enskog distribution. The

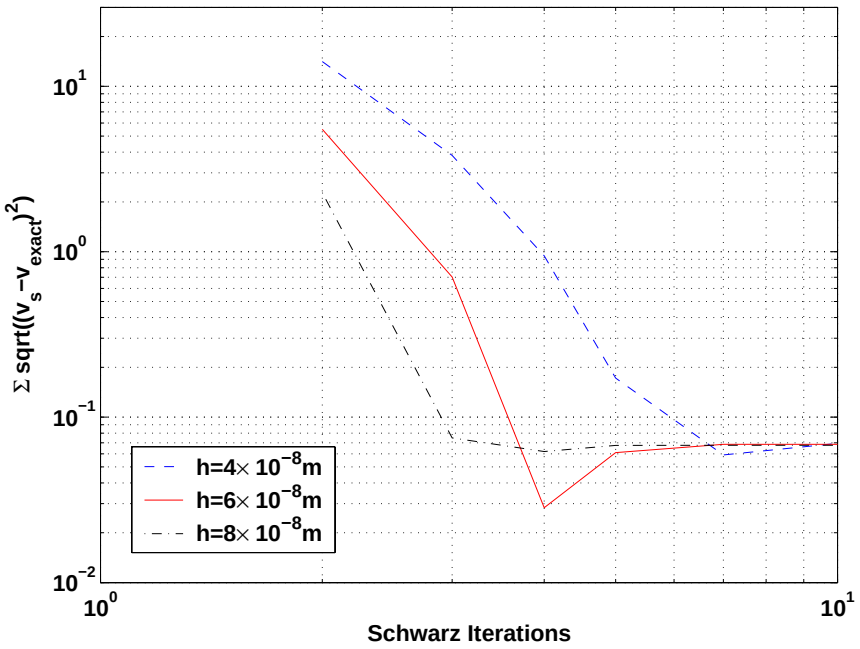

Figure 5-9: Effect of overlap region width on the convergence of the hybrid continuum–continuum scheme. The summation is taken over the complete domain.

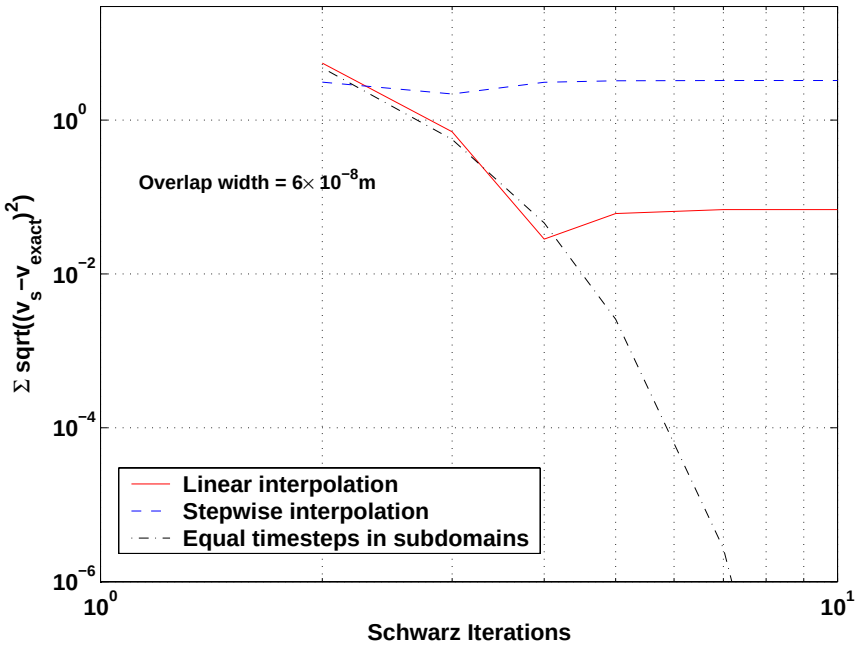

Figure 5-10: Convergence of the hybrid continuum-continuum velocity profile at $t = 4 \times 10^{-8}$s as a function of no. of Schwarz iterations and boundary condition interpolation scheme. The summation is taken over the complete domain.

Property	Value
Kinematic viscosity ν	$1.1688665 \times 10^{-5}\text{m}^2/\text{s}$
Total domain width L	1×10^{-6} m
Continuum subdomain width L_c	0.75625×10^{-6} m
Continuum nodes in L_c	51
Continuum time step Δt_c	1.0×10^{-10} s
Atomistic subdomain width L_a	0.25×10^{-6} m
DSMC cells in L_a	20
No. of particles in each cell	2000
DSMC time step Δt_p	1.0×10^{-11} s
Overlap region width h	6.25×10^{-9} m
Reservoir region width	4.0×10^{-8} m
DSMC time steps per ensemble	100
No. of ensembles	1000
Schwarz iterations per time step	10
Wall velocity V_0	30 m/s

Table 5.2: Unsteady Schwarz simulation parameters for the impulsive Couette flow test problem.

mean particle velocity in the reservoir is obtained by linear time interpolation as detailed in Equation (5.7) and by linear spatial interpolation between the continuum nodes. Imposition of the atomistic boundary conditions on the continuum subdomain follows the use of overlapping continuum nodes and DSMC cell centers similar to the steady flow case. Direct imposition is possible here as the continuum time step is chosen to be an integer multiple of the DSMC time step.

The statistical error of the atomistic solution is reduced by ensemble averaging performed using simulations initiated from different random number seeds. The N_E^{max} ensembles created over a time interval $t^n - t^{n+1}$ are retained and advanced at each subsequent time interval. Additional parameters used in the unsteady simulations are listed in Table 5.2.

Figure 5-11 compares the hybrid solution obtained at times $t = 1 \times 10^{-9}\text{s} = 5.4\tau$ through $t = 4 \times 10^{-9}\text{s} = 21.6\tau$ with the fully atomistic DSMC solution. The hybrid solution shows good comparison and captures the unsteady velocity slip at the wall.

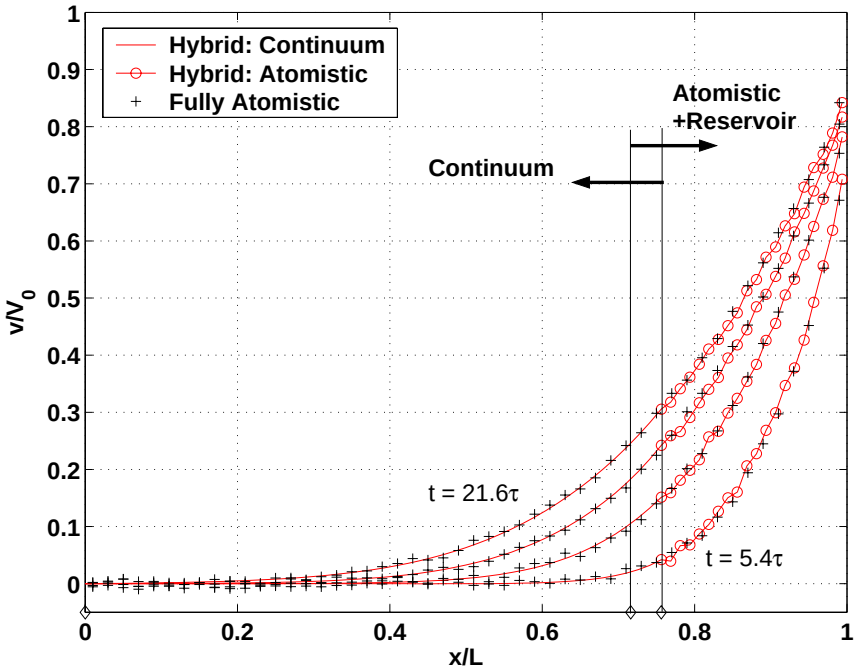

Figure 5-11: Comparison of the unsteady hybrid scheme with the fully DSMC atomistic solution. 10 Schwarz iterations were required to converge the solution at each time level. Velocity profiles are shown for $t = 5.4\tau, 10.8\tau, 16.2\tau$ and 21.6τ respectively, where $\tau = 1.8559 \times 10^{-10}$s is the gas mean collision time.

5.4 Acceleration of Unsteady Hybrid Atomistic–Continuum Schemes

In this Section we develop an acceleration scheme that takes advantage of the time scale decoupling properties of the Schwarz method. The idea behind this method is that a large number of ensemble members is only needed for noise reduction purposes whereas the hydrodynamic behavior of the system is present in *any* of the ensemble members albeit in a noisy form. Thus, since the coupling procedure used here allows for a large gap between sampling times (only when matching occurs, which can be as infrequent as only once in the calculation) it is natural to attempt to use a large number of ensembles only during the sampling phase. This can be achieved by noting that the decorrelation time between different calculations is small compared to the hydrodynamic time scale (especially of the outer problem). Thus if a small number of ensemble members are used for the majority of the time integration and from these systems a larger amount of systems are generated by perturbation at a time which allows for decorrelation, a full decorrelated sample will

exist when required without integrating this full ensemble through time. In the case of our DSMC calculation sufficiently perturbed systems can be generated by simply changing the random number seed but using the same initial configuation. In our nomenclature, in the unsteady Schwarz coupling approach of the previous Section N_E^{max} particle ensembles are created and advanced through each time interval $t^n \rightarrow t^{n+1}$. According to the approach proposed here the ensemble creation within a single time interval $t^n \rightarrow t^{n+1}$ is split into 2 stages, i.e. N_{E1}^{max} ensembles for simulation time $t^n \rightarrow t^{n+\delta}$ and N_{E2}^{max} ensembles for time $t^{n+\delta} \rightarrow t^{n+1}$ such that,

$$N_{E1}^{max}(t^{n+1} - t^{n+\delta})/\Delta t_p + N_{E2}^{max}(t^{n+\delta} - t^n)/\Delta t_p < N_E^{max}(t^{n+1} - t^n)/\Delta t_p \quad (5.9)$$

$$N_{E1}^{max} < N_{E2}^{max} \quad (5.10)$$

where Δt_p is the time step of the atomistic subdomain simulation and $0 < \delta < 1$. Note that N_{E2}^{max} can equal N_E^{max} to allow the same degree of error reduction in the final solution at time t^{n+1}.

The computation cost reduction of the unsteady Schwarz method using limited ensembles in this manner is dependent on the values of δ and N_{E1}^{max} required to maintain accuracy. Results from an initial analysis of the method using a fully atomistic simulation of an impulsive Couette flow are shown in Figure 5-12. For these tests $N_{E2}^{max} = 2000$ and δ is chosen such that $(t^{n+1} - t^{n+\delta})/\Delta t_p = (t^{n+\delta} - t^n)/\Delta t_p = 500$ DSMC time steps. This provides a 26.9τ decorrelation time before sampling of the atomistic solution. Good comparison is obtained for the $N_{E1}^{max} = 100$ simulation. The reduction in error as a function of N_{E1}^{max} is further plotted in Figure 5-13 which shows a slow decay with N_{E1}^{max}. This indicates that a small number of ensembles is required to carry the dynamics forward in time, i.e., N_{E1}^{max} should be kept as small as possible. The choice of parameters for this test using limited ensemble acceleration results in a 47% savings in simulation cost over a non–accelerated unsteady simulation. The limited ensemble approach is incorporated within an unsteady hybrid scheme applied to an impulsive Couette flow test problem next.

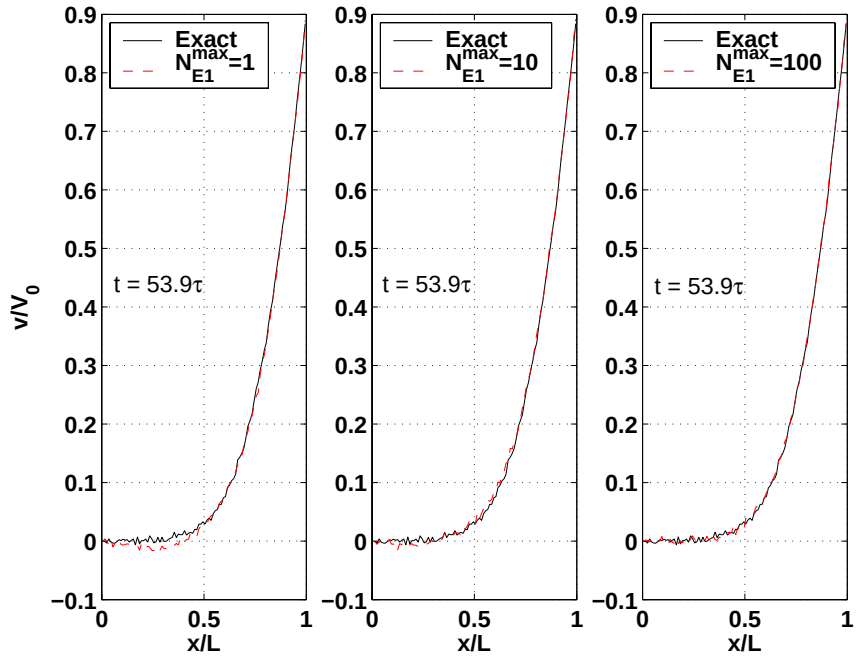

Figure 5-12: Comparison of limited ensemble acceleration using varying number of N_{E1}^{max} ensembles. The velocity profile at $t = 53.9\tau$ is plotted for a fixed $N_{E1}^{max} = 2000$. $\tau = 1.8559 \times 10^{-10}$s is the mean collision time.

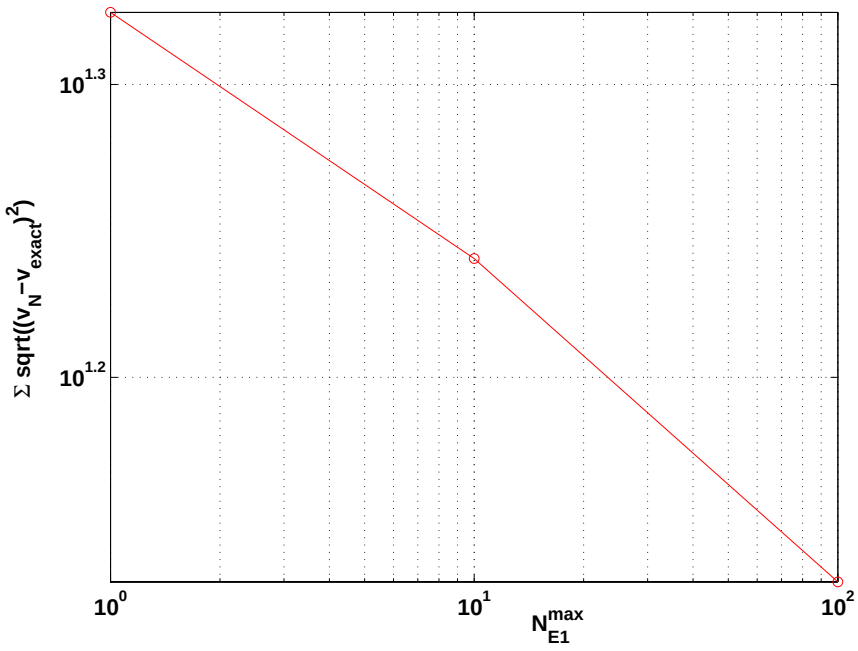

Figure 5-13: Error reduction of limited ensemble acceleration as a function of N_{E1}^{max}. The summation is taken over the complete domain.

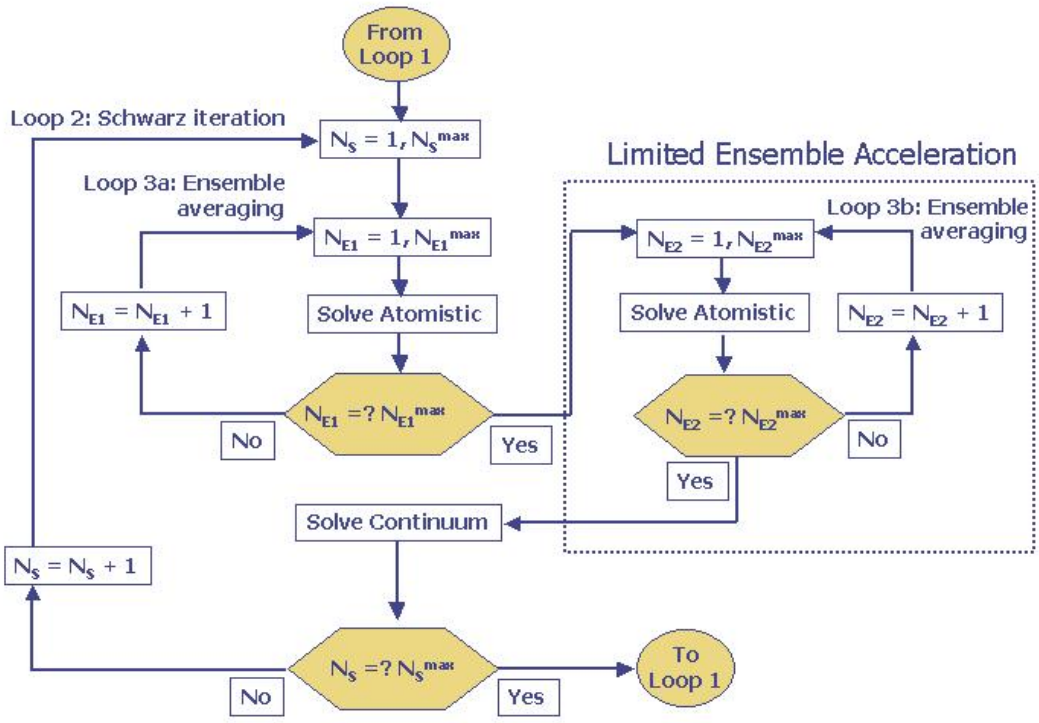

Figure 5-14: Algorithm schematic for limited ensemble acceleration. Loop 1 corresponds to the time iteration loop in Figure 5-4.

5.4.1 Impulsive Couette Flow Test Problem

Limited ensemble acceleration can be incorporated within a hybrid scheme with minor modification to the overall algorithm as shown in Figure 5-14. The ensemble creation loop is split into 2 stages during advance of the atomistic solution calculated by DSMC. The continuum subdomain is solved using the implicit backward difference scheme described in Section 5.2.2. Particle reservoirs are used to impose the linearly time interpolated continuum boundary condition on the atomistic subdomain. The atomistic boundary condition is directly imposed on the continuum subdomain. Parameters for the unsteady simulation are listed in Table 5.3.

Unlike in the non–accelerated unsteady hybrid scheme however, there are now two families of particle ensembles that consist of N_{E1}^{max} and N_{E2}^{max} members respectively where $N_{E2}^{max} > N_{E1}^{max}$. The N_{E2}^{max} members are created by splitting off an additional $(N_{E2}^{max} - N_{E1}^{max})$ members with different random number seeds at time $t^{n+\delta}$ from the N_{E1}^{max} original ensembles as shown graphically in Figure 5-15. This process beginning at time t^n is repeated for N_s^{max}

Property	Value
Kinematic viscosity ν	$1.1688665 \times 10^{-5}\text{m}^2/\text{s}$
Total domain width L	4×10^{-6} m
Continuum subdomain width L_c	3.71×10^{-6} m
Continuum nodes in L_c	186
Continuum time step Δt_c	1.0×10^{-10} s
Atomistic subdomain width L_a	0.30×10^{-6} m
DSMC cells in L_a	15
No. of particles in each cell	2000
DSMC time step Δt_p	1.0×10^{-11} s
No. of ensembles N_{E1}^{max}	100
No. of ensembles N_{E2}^{max}	2000
DSMC time steps per ensemble	500 for both N_{E1}^{max} and N_{E2}^{max}
Reservoir region width	4.0×10^{-8} m
Overlap region width h	1.0×10^{-8} m
Schwarz iterations per time step	10
Wall velocity V_0	30 m/s

Table 5.3: Accelerated unsteady Schwarz simulation parameters for the impulsive Couette flow test problem.

Schwarz iterations. At the final Schwarz iteration N_s^{max} a limited set of the N_{E2}^{max} ensemble members are then advanced forward as the new N_{E1}^{max} ensemble family for the next time interval. The velocities of these new N_{E1}^{max} members are first reset to the t^{n+1} ensemble–averaged solution while retaining their spatial distribution. The process is repeated at each coupling time interval. Note also that in this simulation 10 Schwarz iterations are used to couple the solution at every 1×10^{-8}s (53.9τ) compared to coupling at every 1×10^{-9}s (5.39τ) for the non–accelerated scheme. While this is driven by the need to provide sufficient decorrelation time before sampling of the N_{E2}^{max} ensembles, it also highlights the versatility of the hybrid Schwarz coupling to match solutions at arbitrary times.

The results from the accelerated unsteady hybrid scheme are shown in Figure 5-16. Good comparison is obtained with a fully atomistic solution. The simulation cost of this scheme is compared to a fully atomistic scheme and a non–accelerated unsteady Schwarz scheme in Table 5.4. For the parameters chosen in this example the use of limited ensemble acceleration has helped reduce the total simulation cost of an unsteady hybrid scheme by more than a factor of 2. Of course in applications of practical interest, the atomistic region will be significantly smaller than the continuum region leading to larger savings. In the

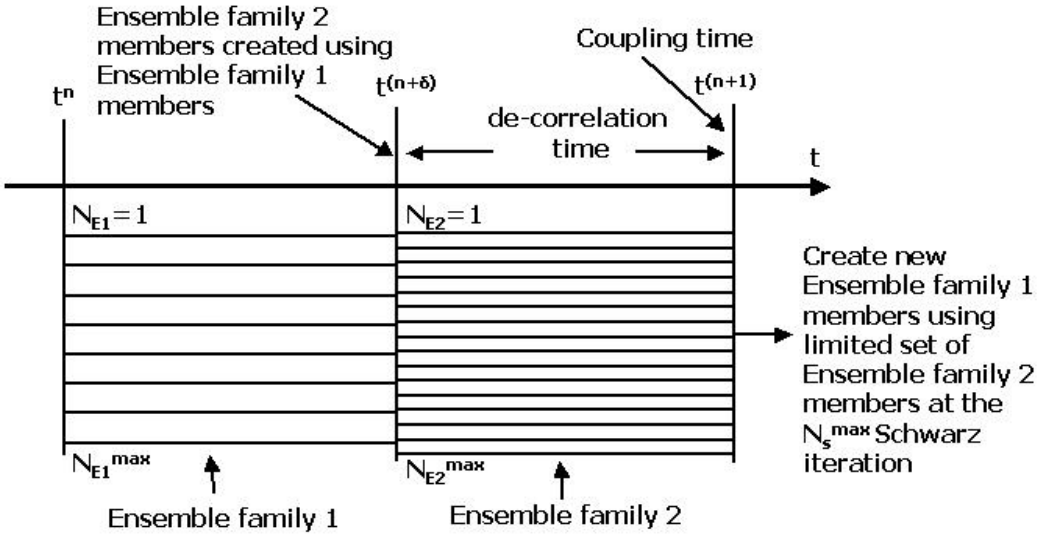

Figure 5-15: Graphical illustration of the limited ensemble acceleration approach.

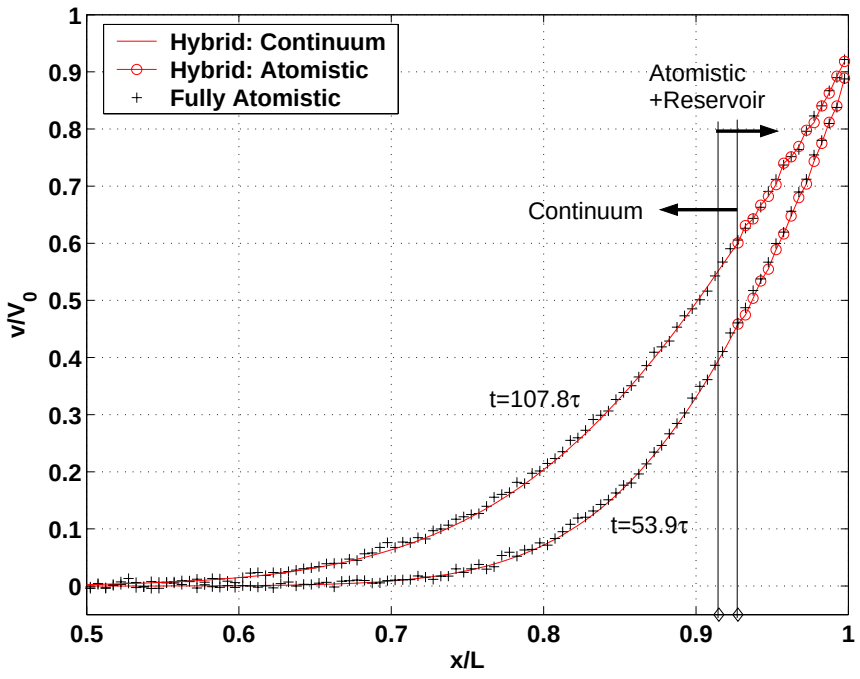

Figure 5-16: Comparison of limited ensemble accelerated unsteady hybrid scheme for impulsive Couette flow with fully atomistic solution. $\tau = 1.8559 \times 10^{-10}$s is the mean collision time.

Property	Atomistic	Hybrid	Hybrid (accelerated)
Atomistic subdomain width L_a	4.00μm	0.3μm	0.3μm
Ensembles N_E^max	2000	2000	$N_{E1}^{max} = 100$, $N_{E2}^{max} = 2000$
DSMC time steps N_{m1}^{max}	1000	1000	500 for both N_{E1}^{max} and N_{E2}^{max}
Schwarz iterations N_s^{max}	0	10	10
Cost ($L_a \times N_{m1}^{max} \times N_E^{max} \times N_s$)	8×10^6	6×10^6	3.15×10^6
Savings (compared to Atomistic)	-	25.0%	60.6%

Table 5.4: Comparison of simulation cost.

same vein, the time scale of evolution of the continuum subdomain will be significantly larger than the atomistic decorrelation time leading to additional savings from the limited ensemble procedure.

Chapter 6

Explicit Coupling

In this Chapter an Adaptive Mesh and Algorithm Refinement (AMAR) based compressible hybrid formulation is described. Atomistic–continuum coupling is achieved by explicit time integration of fluxes. AMAR ensures the atomistic description is applied exclusively in localized regions with high flow gradients and discontinuous material interfaces, i.e. regions where the continuum flow assumptions are typically invalid. Direct Simulation Monte Carlo (DSMC) is used to model the atomistic regions on the finest grid of the adaptive hierarchy. The continuum flow is modeled using the compressible flow Euler equations and is solved using a second order Godunov scheme. The AMAR data structures are supported by a C++ object oriented framework using the Structured Adaptive Mesh Refinement Application Infrastructure (SAMRAI) software library [84]. The AMAR routines and the SAMRAI library were written by members of the Center for Applied Scientific Computing (CASC) at the Lawrence Livermore National Laboratory. Code modifications to incorporate binary gas species and subroutines for adaptive refinement criteria were written additionally for this thesis.

6.1 Introduction

The AMAR compressible hybrid formulation developed by Garcia et al. [36] pioneered the use of mesh refinement as a natural framework for robust explicit coupling of an atomistic fluid representation and a continuum field model using flux matching. Fluxes from the atomistic subdomain are transferred to the continuum subdomain by summation of the

mass, momentum and energy of particles that cross the atomistic–continuum interface. Imposition of fluxes from the continuum subdomain on the atomistic subdomain is facilitated by "buffer cells" similar to particle reservoirs used for Schwarz coupling. This formulation is extended in the present work by a) modifications to the atomistic and continuum models to simulate binary gas mixtures, b) development of a theoretical description for the effect of statistical fluctuations on refinement criteria and c) development of tolerance parameters based on flow field values and gradients for robust continuum to atomistic refinement.

The continuum and atomistic solution methods are described first in the context of the AMAR explicit coupling approach. Reliable and accurate grid and algorithm refinement criteria to track fluid interfaces are discussed next. Finally numerical results are presented for several test cases and compared against theory and other simulations.

6.2 Adaptive Mesh and Algorithm Refinement

This section describes the Adaptive Mesh and Algorithm Refinement (AMAR) explicit coupling methodology in which a continuum algorithm is replaced by an atomistic algorithm at the finest grid scale in a hierarchical adaptive grid refinement (AMR) setting. A detailed description of the AMAR scheme is provided by Garcia et. al. [36]. This work is summarized here for completeness together with a description of the modifications required for simulations of binary gas mixtures.

6.2.1 AMR Algorithm for Continuum Hydrodynamics

The AMAR implementation is built on a structured AMR grid hierarchy where the compressible, two–species Euler equations are solved on every grid level except the finest. Note that AMAR uses the same adaptive meshing and time integration algorithms developed for continuum modeling of hyperbolic hydrodynamics [12, 13].

Consider the governing Euler equations written in conservative form,

$$\frac{\partial \mathbf{U}}{\partial t} + \frac{\partial \mathbf{F_x}}{\partial x} + \frac{\partial \mathbf{F_y}}{\partial y} + \frac{\partial \mathbf{F_z}}{\partial z} = 0 \tag{6.1}$$

where,

$$\mathbf{U} = \begin{pmatrix} \rho \\ p_x \\ p_y \\ p_z \\ \rho E \\ \rho c \end{pmatrix} \qquad \mathbf{F_x} = \begin{pmatrix} \rho u \\ \rho u^2 + P \\ \rho uv \\ \rho uw \\ \rho uH \\ \rho cu \end{pmatrix} \qquad \mathbf{F_y} = \begin{pmatrix} \rho v \\ \rho uv \\ \rho v^2 + P \\ \rho wv \\ \rho vH \\ \rho cv \end{pmatrix} \qquad \mathbf{F_z} = \begin{pmatrix} \rho w \\ \rho uw \\ \rho vw \\ \rho w^2 + P \\ \rho wH \\ \rho cw \end{pmatrix} \tag{6.2}$$

and,

$$P = \rho RT \qquad \rho E = P\frac{1}{\gamma - 1} + \frac{1}{2}\rho|V|^2 \qquad \rho H = P\frac{\gamma}{\gamma - 1} + \frac{1}{2}\rho|V|^2 \tag{6.3}$$

The mass concentration variable c gives the concentration of the first gas species. By definition, $(1-c)$ represents the mass concentration of the second gas species. The concentration variable is purely convected here by the mean flow as governed by the Euler equations.

Discrete time integration is performed using a finite volume approximation to Equation (6.1). This yields a conservative finite difference expression with $\mathbf{U}^n_{ijk}$ appearing as a cell–centered quantity at each time level and $\mathbf{F}^{x,n+\frac{1}{2}}_{i+\frac{1}{2},j,k}$ located at faces between cells at half–time level [55], i.e,

$$\begin{aligned} \mathbf{U}^{n+1}_{ijk} = \mathbf{U}^n_{ijk} \quad - \quad & \Delta t_{\mathrm{c}} \left(\frac{\mathbf{F_x}^{x,n+\frac{1}{2}}_{i+\frac{1}{2},j,k} - \mathbf{F_x}^{x,n+\frac{1}{2}}_{i-\frac{1}{2},j,k}}{\Delta x} + \frac{\mathbf{F_y}^{y,n+\frac{1}{2}}_{i,j+\frac{1}{2},k} - \mathbf{F_y}^{y,n+\frac{1}{2}}_{i,j-\frac{1}{2},k}}{\Delta y} \right. \\ + \quad & \left. \frac{\mathbf{F_z}^{z,n+\frac{1}{2}}_{i,j,k+\frac{1}{2}} - \mathbf{F_z}^{z,n+\frac{1}{2}}_{i,j,k-\frac{1}{2}}}{\Delta z} \right) = 0 \end{aligned} \tag{6.4}$$

A multidimensional second–order version of an unsplit Godunov scheme [24, 25, 78] is used to approximate the fluxes in Equation (6.4). Specific time integration routines for AMAR can be found in [55]. A summary is given below.

Time stepping on an AMR grid hierarchy involves interleaving time steps on individual levels [13]. Each level has its own time step as dictated by its spatial resolution (typically constrained by a CFL condition). The key to achieving a conservative AMR algorithm is

to define a discretization for Equation (6.1) that holds on every level of the grid hierarchy. In particular, the discrete cell volume integrals of **U** and the discrete cell face integrals of **F** must match on the locally–refined AMR grid. Thus, integration of a level involves two steps: solution advance and solution synchronization with other levels. Synchronizing the solution across levels assumes that fine grid values are more accurate than coarse grid values. Thus, coarse values of **U** are replaced by suitable cell volume averages of finer **U** data where levels overlap, and discrete fine flux integrals replace coarse fluxes at coarse–fine grid boundaries. Although the solution is computed differently in overlapping cells on different levels as each level is advanced initially, the synchronization procedure enforces conservation over the entire AMR grid hierarchy.

6.2.2 Atomistic Algorithm

The atomistic algorithm used in AMAR is the direct simulation Monte Carlo (DSMC) method outlined in Chapter 2. The single gas species advection and collision relationships defined in Equation (2.1) and Equations (2.7)–(2.10) also hold for the case of a binary gas mixture. The state of the system is now given by positions and velocities of two particle species s_1 and s_2; $(\mathbf{r}_i^{s_1}, \mathbf{v}_i^{s_1}, i = 1...N^{s_1})$ and $(\mathbf{r}_i^{s_2}, \mathbf{v}_i^{s_2}, i = 1...N^{s_2})$. The system evolves in time using the familiar splitting approach. First particles from both species are moved without interaction according to Equation (2.1) and appropriate boundary conditions are applied to particles that reach the DSMC domain boundary. Second, after all particles have moved, a given number are randomly selected for collisions. Unlike with the single species case, there are now 3 pairs of collision candidates (species 1→species 1, species 1→species 2 and species 2→species 2), with M_{cand}^{11}, M_{cand}^{12}, and M_{cand}^{22} number of collisions per cell respectively,

$$M_{cand}^{11} = \frac{N_c^{s_1}(N_c^{s_1}-1)N_{ef}\pi\sigma_1^2 v_r^{max11}\Delta t_p}{2V_c} \tag{6.5}$$

$$M_{cand}^{12} = \frac{N_c^{s_1}N_c^{s_2}N_{ef}\pi\sigma_{12}^2 v_r^{max12}\Delta t_p}{V_c} \tag{6.6}$$

$$M_{cand}^{22} = \frac{N_c^{s_2}(N_c^{s_2}-1)N_{ef}\pi\sigma_2^2 v_r^{max22}\Delta t_p}{2V_c} \tag{6.7}$$

where $\sigma_{12} = 0.5 \times (\sigma_1 + \sigma_2)$, σ_1, σ_2 are the hard sphere diameters of the species, $N_c^{s_1,s_2}$ are the number of particles per cell, $v_r^{max11,12,22}$ are the species maximum relative speeds, Δt_p is the atomistic time step and V_c is the volume of the cell.

6.2.3 Atomistic–Continuum Coupling

The atomistic–continuum coupling routines used in AMAR are detailed in [96]. The description below is provided for completeness.

The atomistic–continuum coupling routines are best described with reference to the graphical sequence shown in Figure 6-1. During time integration of continuum grid levels, fluxes computed at each cell face are used to advance the solution $\mathbf{U}$ as illustrated in Figure 6-1(b). Continuum values on each level are advanced using a Δt_c appropriate to that level, including those that overlay the DSMC region. When the particle level is integrated, it is advanced to the new time on the finest continuum level using a sequence of particle time steps, Δt_p. The relative magnitude of Δt_p to the finest continuum grid Δt_c depends on the finest continuum grid spacing Δx (typically a few λ) and the particle mean collision time.

Euler solution information is passed to the particles via buffer cells surrounding the DSMC region. At the beginning of each DSMC integration step, particles are created in the buffer cells using the continuum hydrodynamic values (ρ, $\mathbf{u}$, T) and their gradients as illustrated in Figure 6-1(c). Since the continuum solution is advanced first, these values are time interpolated between continuum time steps for the sequence of DSMC time steps needed to reach the new continuum solution time. DSMC buffer cells are one mean free path wide; thus, the time step Δt_p is constrained such that it is extremely improbable that a particle will travel further than one mean free path in a single time step. The particle velocities are drawn from an appropriate distribution for the continuum solver, in this case the Maxwell–Boltzmann distribution for the Euler equations.

During each DSMC time integration step, all particles are moved, including those in the buffer regions as shown in Figure 6-1(d). A particle that crosses the interface between continuum and DSMC regions will eventually contribute to the flux at the corresponding continuum cell face during the synchronization of the DSMC level with the finest continuum

level. After moving particles, those residing in buffer regions are discarded. Collisions among the remaining particles are evaluated and new particle velocities are computed.

After the DSMC region has advanced over an entire continuum grid time step, the continuum and DSMC solutions are synchronized in a manner analogous to the AMR level synchronization process described earlier. First, the continuum values in each cell overlaying the DSMC region interior are set to the conservative averages of data from the particles within the continuum grid cell region as illustrated in Figure 6-1(e). Second, the continuum solution in cells adjacent to the DSMC region is recomputed using a "refluxing" process denoted in Figure 6-1(f). Here a flux correction is computed using a space and time integral of particle flux data,

$$\delta\mathcal{F} = -A\mathbf{F}^{n+\frac{1}{2}} + \sum_{\text{particles}} \mathcal{F}_p \tag{6.8}$$

where A is the signed area of a grid cell face. The sum represents the flux of the conserved quantities carried by particles passing through the continuum cell face during the DSMC updates. Finally,

$$\mathbf{U}^{n+1} = \overline{\mathbf{U}^{n+1}} + \frac{\Delta t_c \delta\mathcal{F}}{\Delta x \Delta y \Delta z} \tag{6.9}$$

is used to update the conserved quantities on the continuum grid where $\overline{\mathbf{U}^{n+1}}$ is the coarse grid solution before computing the flux correction.

In summary, the coupling between the continuum and DSMC methods is performed in three operations. First, continuum solution values are interpolated to create particles in DSMC buffer cells before each DSMC step. Second, conserved quantities in each continuum cell overlaying the DSMC region are replaced by averages over particles in the same region. Third, fluxes recorded when particles cross the DSMC interface are used to correct the continuum solution in cells adjacent to the DSMC region. This coupling procedure makes the DSMC region appear as any other level in the AMR grid hierarchy.

Multiple DSMC parallelepiped regions (i.e., *patches*) are coupled by copying particles from patch interiors to buffer regions of adjacent DSMC patches (see Figure. 6-2). That is, particles in the interior of one patch supply boundary values (by acting as a reservoir) for

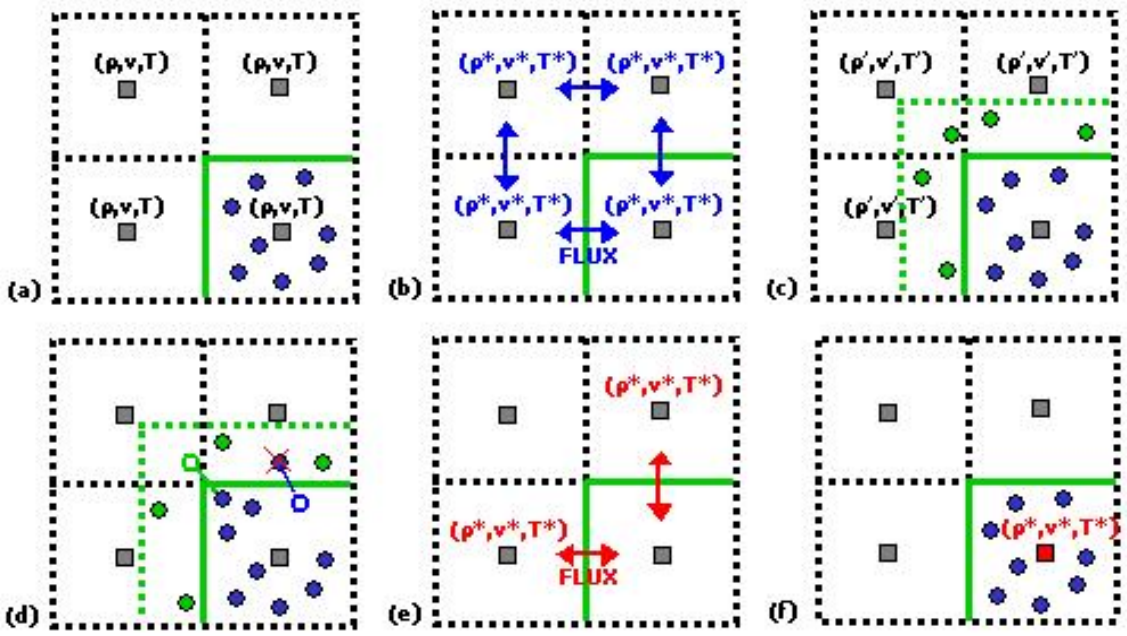

Figure 6-1: Outline of AMAR hybrid: (a) Beginning of a time step; (b) Advance the continuum grid; (c) Create buffer particles; (d) Advance DSMC particles; (e) Refluxing; (f) Reset overlying continuum grid. Adapted from [96].

adjacent particle patches. After copying particles into buffer regions, each DSMC patch may be integrated *independently*, in the same fashion that different patches in a conventional AMR problems are treated after exchanging boundary data.

6.3 Euler–DSMC Code Implementation

The Euler–DSMC AMAR code utilized in this work is composed of elements from the SAMRAI object–oriented framework, developed at the Lawrence Livermore National Laboratory, and numerical routines specific to the application. SAMRAI provides a general, flexible software toolbox for developing multi–physics AMR applications and supports general parallel data management capabilities, including particle representations, on an AMR grid hierarchy [56]. A brief overview is given below [84].

The organization of major algorithmic parts in the hybrid Euler–DSMC code is similar to that of an Euler–only AMR code. However, the hybrid code requires a new level integrator that coordinates DSMC and Euler operations on different hierarchy levels. The new integrator, developed for this project, was constructed from elements in SAMRAI. Figure 6-

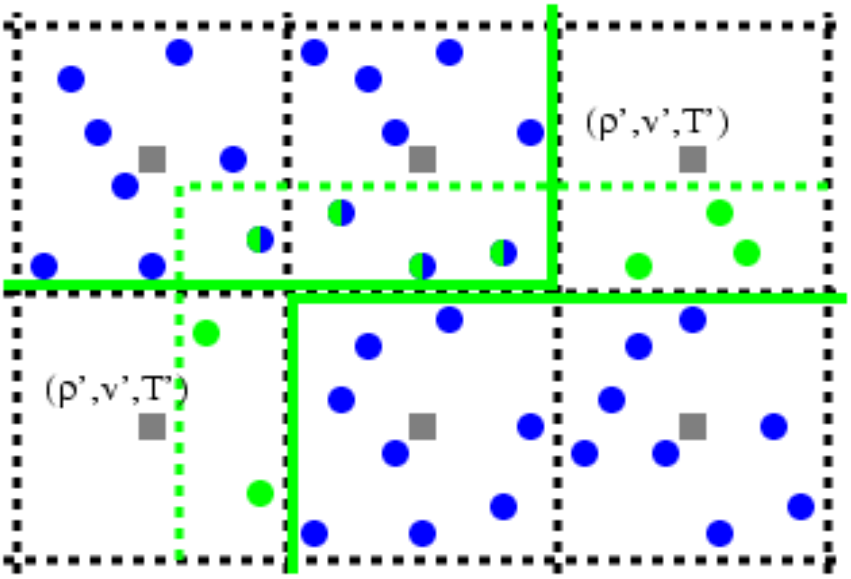

Figure 6-2: Multiple DSMC regions are coupled by copying particles from one DSMC region (upper left) to the buffer region of an adjacent DSMC region (lower right). After copying, regions are integrated independently over the same time increment. Adapted from [96].

3 illustrates the relationships between this and other algorithmic parts. It is interesting to note that all classes appearing in an Euler–only application are used without modification in the hybrid code. Also, the DSMC data structures and numerical routines, developed previous to incorporation in the hybrid application, were introduced without significant modification. Recall that the Euler continuum model and DSMC particle model are vastly different numerical approaches. The Euler model represents compressible fluid flow as a deterministic system of partial differential equations containing a few grid–based variables. DSMC approximates the Boltzmann equation using a representative, stochastic sampling of a collection of particles whose state and motion are essentially grid–less. The DSMC data structures and numerical routines are insulated from SAMRAI abstractions by a "wrapper" interface class. This class serves two important functions. First, it acts as a translator between SAMRAI patch data and the DSMC particle structures. Second, it allows the particles to be manipulated on a distributed parallel machine by SAMRAI. More importantly, the *serial* DSMC routines were coupled to the SAMRAI parallel communication framework without changing the particle structures or routines or recompiling SAMRAI library code. Additional details describing how this is done appear in [56].

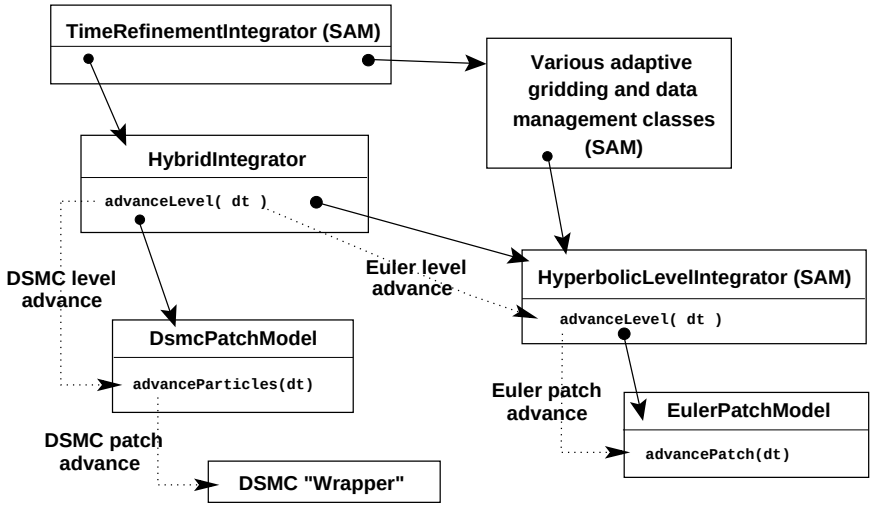

Figure 6-3: Illustration of the coupling of the major algorithmic components in the Euler-DSMC code. Bold arrows indicate where one object owns a reference to another. Dashed arrows indicate control flow for advance operations. Classes from the SAMRAI library are indicated by "(SAM)". Numerical operations on Euler patches are called in the EulerPatchModel class. DSMC numerical routines are called in the DSMCPatchModel class. A DSMC "Wrapper" object holds the DSMC data on each DSMC patch and couples it to the SAMRAI communication routines. Adapted from [56].

6.4 Refinement Criteria

Standard AMR methods assume that continuum field equations are valid at all length scales in the computation. Regions for grid refinement are located using ad–hoc notions (e.g., refine around steep gradients) or analytical error estimation techniques involving the differential equations (e.g., Richardson extrapolation [13]). In contrast, hybrid methods apply computational models matched to the flow characteristics at each physical scale.

The AMAR algorithm can refine the grid and algorithm based on any flow field property and combinations thereof. For single species flows, refinement based on density gradients have been found to be robust and reliable. The tracking of concentration gradients or concentration values within specific interval are also effective for multi–species flows involving concentration interfaces. These refinement criteria will be demonstrated shortly with test examples in Section 6.5.

The parameters for transitioning from the continuum algorithm to the atomistic algorithm used here are based on a continuum breakdown parameter method proposed by Bird [19], whereby refinement is triggered by spatial gradients exceeding empirically–determined tolerances. The gradient detector formula employed in AMAR is a variation of a sharp dis-

continuity detector by Trangenstein and Pember [88].

Due to fluctuations present in atomistic computations, it is important to develop gradient refinement methods that do not allow fluctuations to trigger unnecessary refinement and excessively large atomistic regions. For example, at thermodynamic equilibrium, the standard deviation in the normalized gradient of density due to atomistic fluctuations can be shown to be given by [7],

$$\sigma = \sqrt{\left\langle \left(\frac{d\rho/dx}{\rho} \right)^2 \right\rangle} \approx \sqrt{\left\langle \left(\frac{N_{c(i+1)} - N_{ci}}{\Delta x_c \langle N_{ci} \rangle} \right)^2 \right\rangle} = \frac{\sqrt{2}}{\Delta x_c \sqrt{\langle N_c \rangle}} \tag{6.10}$$

since N_c, the number of particles in a DSMC cell, is Poisson distributed.

To investigate the effect of a fluctuating atomistic description on the continuum subdomain, an AMAR hybrid atomistic–continuum simulation was conducted for an equilibrium uniform stationary fluid. A 2 level (fine and coarse) AMAR grid hierarchy was used to discretize the geometry outlined in Figure 6-4. The atomistic and continuum subdomains are predetermined here and density gradient tolerance based refinement is turned off. The atomistic subdomain consists of 512 DSMC cells each of volume λ^3 in a cube $8\lambda \times 8\lambda \times 8\lambda$ occupying the fine grid level. The continuum subdomain consists of 400 cells each of volume $8\lambda^3$ arranged in a parallelepiped geometry of $50\lambda \times 8\lambda \times 8\lambda$ on the coarse grid level. Argon gas was simulated at atmospheric conditions; pressure $P = 1.013 \times 10^5$ Pa and temperature $T = 273$ K. Both atomistic and continuum subdomains were initialized with uniform density 1.78×10^{-3}g/cm^3. As shown in [7] for a given computational grid the density fluctuation can only be reduced by increasing the number of DSMC simulation particles per cell N_c. This is captured in Figures 6-5, 6-6, 6-7 where the density (averaged over the y–z plane) is plotted for $N_c = 20, 80$ and 320 respectively as a function of the x–coordinate position. The error bars indicate a one standard deviation in the density fluctuation over a 10 time step ($7.5 \times 10^{-10} s = 4\tau$) interval. As can be seen in these Figures, fluctuations in the atomistic region causes the continuum region to also fluctuate with a variance which decreases with the distance from the continuum interface. In fact, the variance of the fluctuations in the continuum region adjacent to the interface is very close to the atomistic region fluctuation variance. This is in agreement with the observations by Alexander et. al. [7] who performed similar measurements on a system of random walkers simulating the diffusion equation.

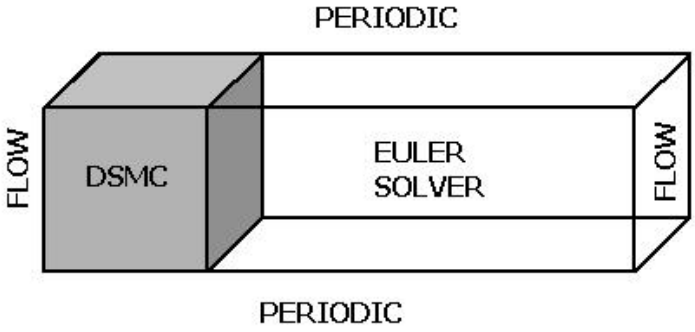

Figure 6-4: 3D AMAR computational domain for investigation of tolerance parameter variation with number of particles in DSMC cells N_c.

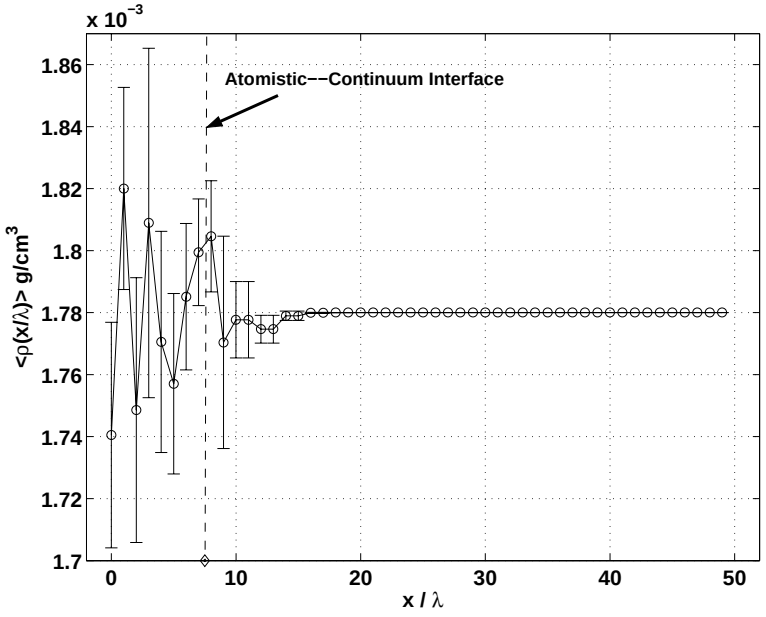

Figure 6-5: Average density for stationary fluid AMAR hybrid simulation with $N_c = 20$. Error bars give one standard deviation over 10 samples.

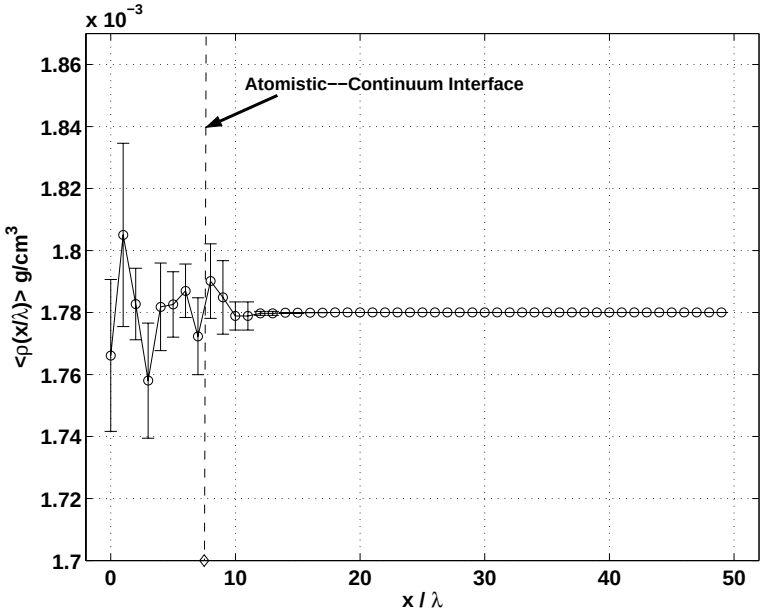

Figure 6-6: Average density for stationary fluid AMAR hybrid simulation with $N_c = 80$. Error bars give one standard deviation over 10 samples.

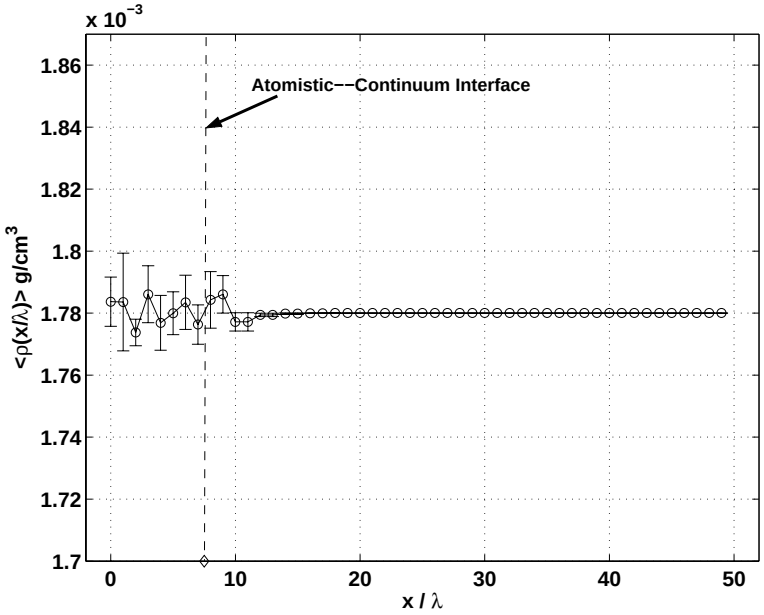

Figure 6-7: Average density for stationary fluid AMAR hybrid simulation with $N_c = 320$. Error bars give one standard deviation over 10 samples.

These results have consequences for the use of density gradient tolerances R_ρ used for AMAR. In general, such tolerances must be coupled to the number of particles used for the atomistic domain since the spatial gradients of density on the *coarse* grid which is fluctuating are used to decide whether refinement will take place. In particular, refinement occurs in regions where the non–dimensionalized density gradients are above the R_ρ threshold, i.e.

$$R_\rho < \frac{2\lambda}{\rho}\left|\frac{d\rho}{dx}\right| \tag{6.11}$$

To determine the minimum value of R_ρ required to prevent growth of the atomistic region, simulations were conducted using the domain geometry shown in Figure 6-4 for a range of N_c. During a "trigger" event where the density fluctuations exceed R_ρ grid refinement occurs as shown in Figure 6-8. The value of R_ρ that results on average a $5-10\%$ trigger rate (i.e. between 5-10 trigger events per 100 iterations) is plotted in Figure 6-9 as a function of N_c. In what follows we outline how theoretical predictions bounding these numerical results can be obtained. These predictions are shown as solid lines in Figure 6-9.

For the geometry considered here, each continuum cell consists of 8 DSMC cells and hence effectively the contribution of $8 \times N_c$ particles is averaged to determine the density gradient between continuum cells. The relationship between σ and N_c in Equation (6.10) is therefore modified to,

$$\sigma = \frac{1}{2\Delta x_c\sqrt{\langle N_c\rangle}} \tag{6.12}$$

Note that we are assuming that the fluctuation at the continuum cell across the atomistic–continuum interface is the same as that in the atomistic region. This allows the use of Equation (6.10) that was derived assuming 2 atomistic cells. Note the observed trigger event is a composite of a large number of probable density gradient fluctuations that could exceed R_ρ; gradients across all possible nearest neighbor cells, next-to-nearest neighbor cells and diagonally-nearest neighbor cells are all individually evaluated by the refinement routines and checked against R_ρ. For a 10% trigger rate (or equivalent probability of trigger) the probability of an individual cell having a density fluctuation exceeding R_ρ can be estimated as $O(0.1/100)$ by observing that,

- since the trigger event is a rare event, probabilities are additive,

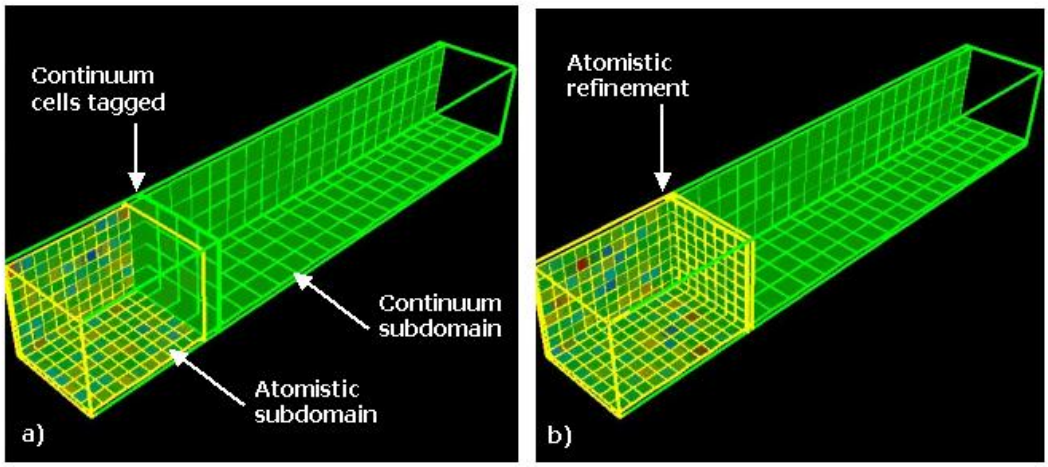

Figure 6-8: 3D AMAR hybrid simulation illustrating continuum to atomistic grid refinement during a "trigger" event where density gradients on coarse grid level exceed a user specified tolerance. a) Region of continuum grid is identified for tagging, b) DSMC routines replace continuum algorithm in tagged region.

- for the geometry considered, there are $O(100)$ nearest neighbor cells that can trigger refinement and
- the rapid decay of the Gaussian distribution ensures the decreasing probability ($O(0.1/100) \sim O(0.001)$) of a single event does not significantly alter the corresponding confidence interval and thus an exact enumeration of all possible trigger pairs with correct weighting factors is not necessary.

For example our probability estimate at $O(0.001)$ suggests that our confidence interval is $3 - 4\sigma$. This is verified in Figure 6-9. Larger trigger rates can be achieved by reducing R_ρ. Curves shown in Figure 6-9 help prototype tolerance criteria using a small number of particles prior to running larger simulations.

6.5 Validation Tests for AMAR

This section describes a range of test problems to verify the AMAR hybrid scheme. All single species tests use gaseous Argon (atomic mass $m = 6.63 \times 10^{-23}$ g, hard sphere diameter $\sigma = 3.66 \times 10^{-8}$ cm). Gases for binary systems will be defined with respect to the specific test problem. The computational domain used consists typically of periodic boundary conditions in the y–z directions and flow boundary conditions in the axial x direction as

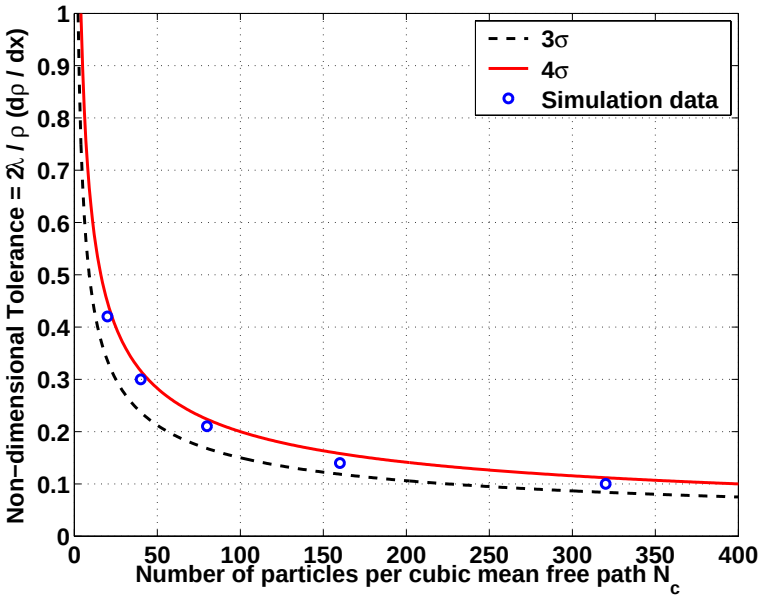

Figure 6-9: Variation of density gradient tolerance with number of DSMC particles per λ^3.

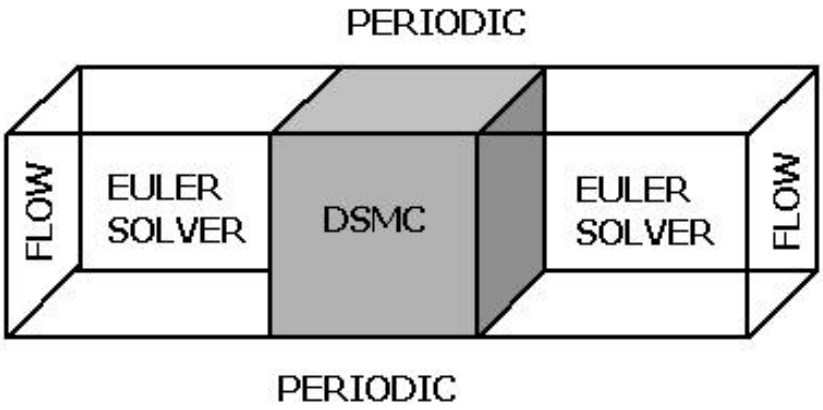

Figure 6-10: 3D AMAR computational domain for validation tests.

illustrated in Figure 6-10 unless noted otherwise. The domain size is $100\lambda \times 12\lambda \times 12\lambda$. All tests consists of 2 grid levels with the continuum subdomain occupying the coarse mesh and the atomistic subdomain residing on the fine.

6.5.1 Uniform Field Test

A uniform field test was conducted with the density and temperature initialized to $\rho = 1.78\times 10^{-3}\text{g/cm}^3$ and $T = 273\text{K}$ and with all velocity components set to zero. The computational domain consists of a cubic DSMC region of size $4\lambda \times 4\lambda \times 4\lambda$ embedded in the center of

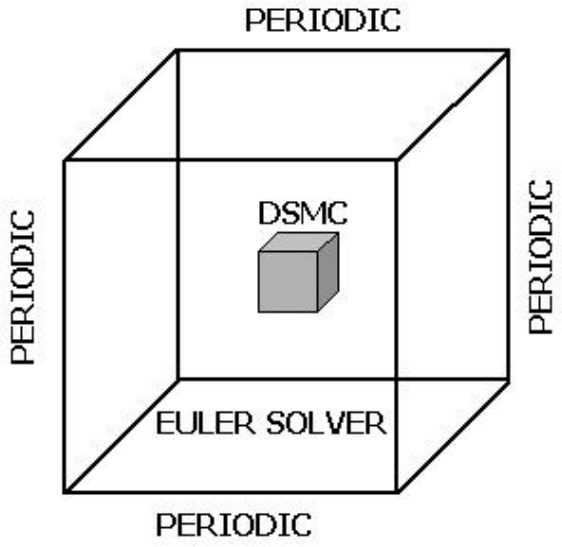

Figure 6-11: Computational domain for uniform field test.

an Euler continuum grid of size $32\lambda \times 32\lambda \times 32\lambda$ as shown in Figure 6-11. The DSMC simulation uses 800 particles per λ^3. The continuum cell size is 2λ while the DSMC grid size is λ. This test condition and geometry match that used by Garcia, et al. [36] to examine thermodynamic equilibrium in an Euler/DSMC hybrid scheme.

Although the initial conditions are uniform, the statistical nature of DSMC generates fluctuations that transfer heat flux to the continuum subdomain. Since the Euler model possesses no mechanism to transfer thermal energy back to the atomistic domain, the result is an energy increase in the continuum subdomain and a corresponding energy decrease in the atomistic subdomain (as total energy is conserved). This in turn produces an increase in density in the atomistic subdomain so that mechanical equilibrium (i.e., constant pressure) is maintained. This is evident by the increase in the total number of particles in the atomistic subdomain as shown in Figure 6-12. This phenomenon is not a flaw in the AMAR methodology but a common observance in other Euler/DSMC hybrid schemes [36]. The DSMC particle increase seen here is within 1% of the initial value and is consistent with the results obtained by Garcia, et al. [36].

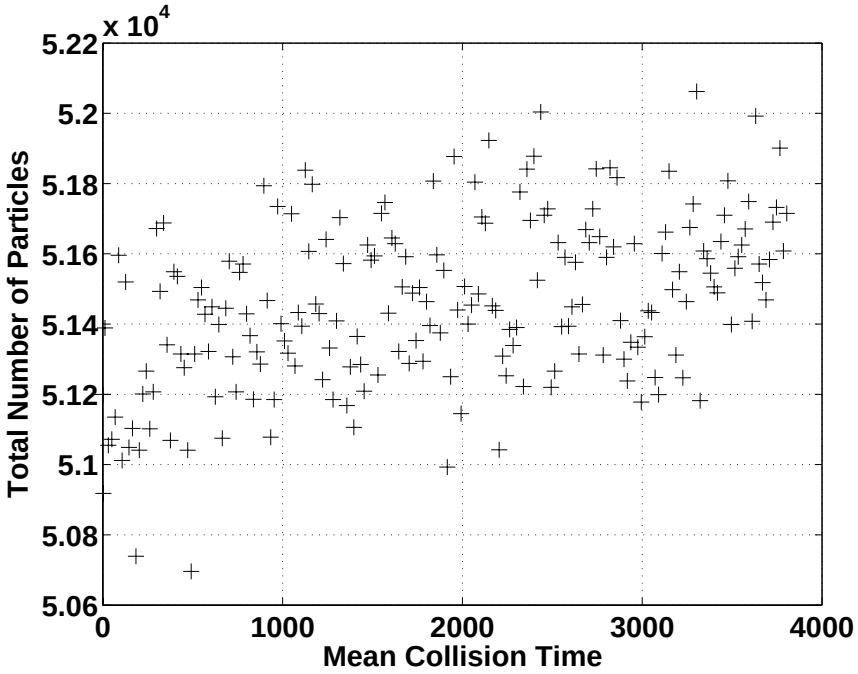

Figure 6-12: Particle increase in the DSMC domain resulting from net heat flux transfer from the atomistic to the continuum region.

6.5.2 Concentration Diffusion

A concentration diffusion test was conducted to assess the ability of the AMAR hybrid scheme to accurately track the spreading of an interface between two gases. Note that since the Euler equations contain no diffusion terms the physics of interface diffusion is captured solely by the DSMC atomistic routines. The diffusion coefficient for two gases modeled as hard spheres can be approximated as [52],

$$\mathcal{D}_{12} = \frac{3}{16}\frac{\sqrt{2\pi k^3 T^3/\mathcal{M}}}{P\pi\sigma_{12}^2} = \frac{3}{8}\frac{1}{n\sigma_{12}^2}\sqrt{\frac{kT}{2\pi\mathcal{M}}} \tag{6.13}$$

where $\mathcal{M} = (1/m_1{+}1/m_2)^{-1} = m_1 m_2/(m_1{+}m_2)$ is the reduced mass, and $\sigma_{12} = (\sigma_1{+}\sigma_2)/2$ is the average diameter. The self–diffusion coefficient for Argon at pressure $P = 1.013 \times 10^5$ Pa and temperature $T = 273$K is $\mathcal{D}_{11} = 0.14\,\mathrm{cm}^2/\mathrm{s}$. The DSMC simulation utilized 80 particles per λ^3.

A simple self–diffusion test can be conducted using Argon gas "colored" differently on either side of an interface (the different colors can be interpreted as different Argon isotopes with negligible differences in mass). The initial conditions for this test are shown

Property	Interval 0	Interval 1
Density (g/cm^3)	0.00178	0.00178
Velocity u (m/s)	0.0	0.0
Temperature (K)	273	273
Mass concentration	1.0	0.0

Table 6.1: Initial conditions for the concentration diffusion test. Interval 0 and Interval 1 correspond to upstream and downstream regions either side of the Argon–Argon interface.

in Table 6.1. A step change in mass concentration corresponds to the different colored Argon species.

Figure 6-13 shows the evolution of the Euler–DSMC computational domain for this self–diffusion test. Initially the red (left) and blue (right) particles are separated by a discontinuous interface corresponding to a step function profile for the gas concentration. Refinement of the computational domain is performed using a mass concentration gradient tolerance parameter R_{mc} and a mass concentration deviation parameter R_{mc}^{dev}. The former is used to locate the DSMC region at the gas interface during initialization and is turned off soon after at $t = \tau$. Since the gradient in mass concentration across a step initialization is infinite, any finite value for R_{mc} ensures the interface region is refined. Subsequently, the mixing region is tracked by placing particles in the region where R_{mc}^{dev} has a value between 0.001 and 0.999. This ensures negligible mass concentration gradients across the interface between the Euler and DSMC regions.

The AMAR concentration profiles for the self–diffusion case are compared with theoretical profiles in Figure 6-14. Also shown is the concentration profile for a test case using Argon and a fictitious gas G with hard–sphere diameter $\sigma_2 = 1.516 \times 10^{-8}$cm such that the diffusion coefficient is exactly twice the coefficient in the self–diffusion case; i.e., $\mathcal{D}_{12} = 2 \times \mathcal{D}_{11} = 0.28\text{cm}^2/\text{s}$. Note the simulated results show excellent agreement with theory in both cases.

6.5.3 Single Gas Stationary Shock Wave

Further validation of the AMAR hybrid scheme was performed using a $M = 5.0$ stationary gas shock wave test. The Rankine–Hugoniot conditions predict the density, temperature

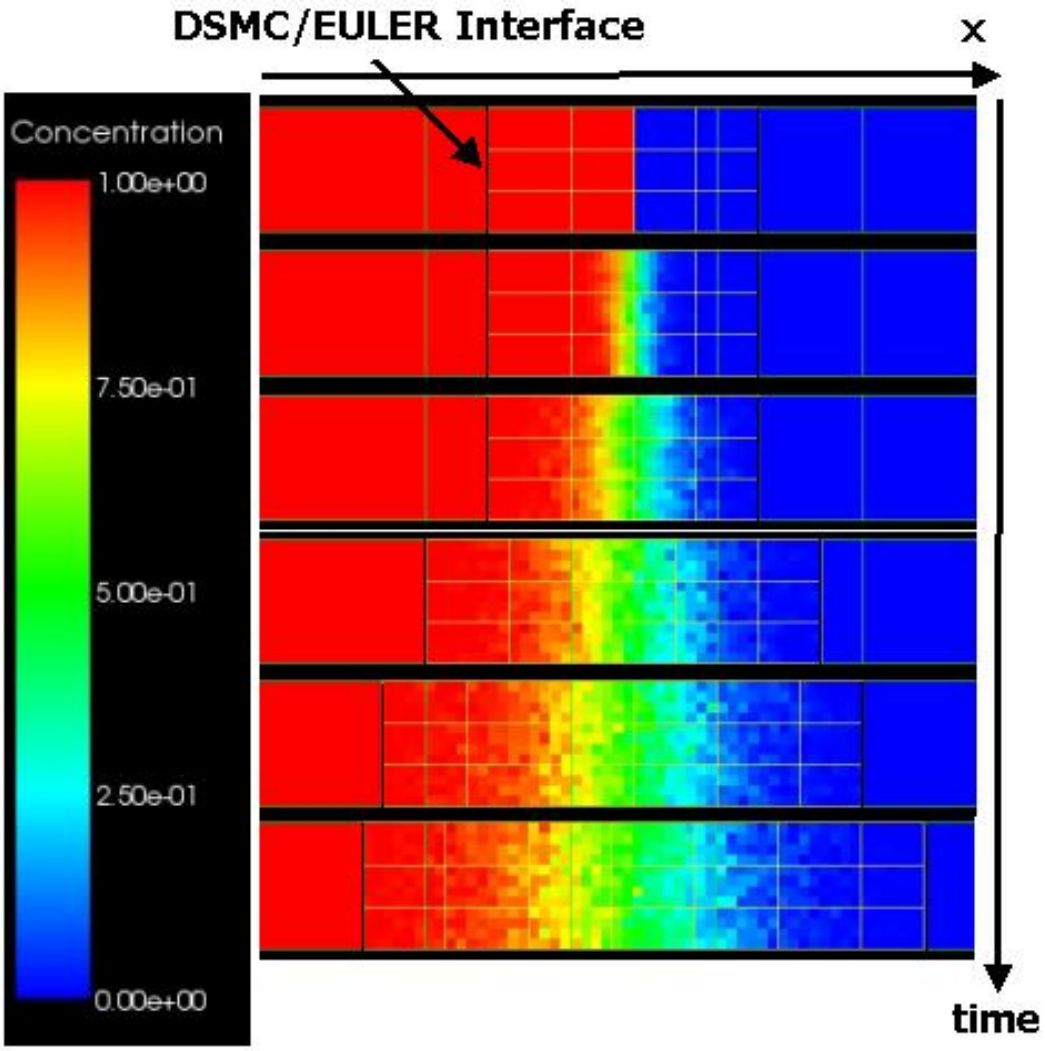

Figure 6-13: Computational domain for self-diffusion interface tracked adaptively. The borders of DSMC patches are indicated by the boxes near the middle of the domain. The Euler model is applied outside of this region.

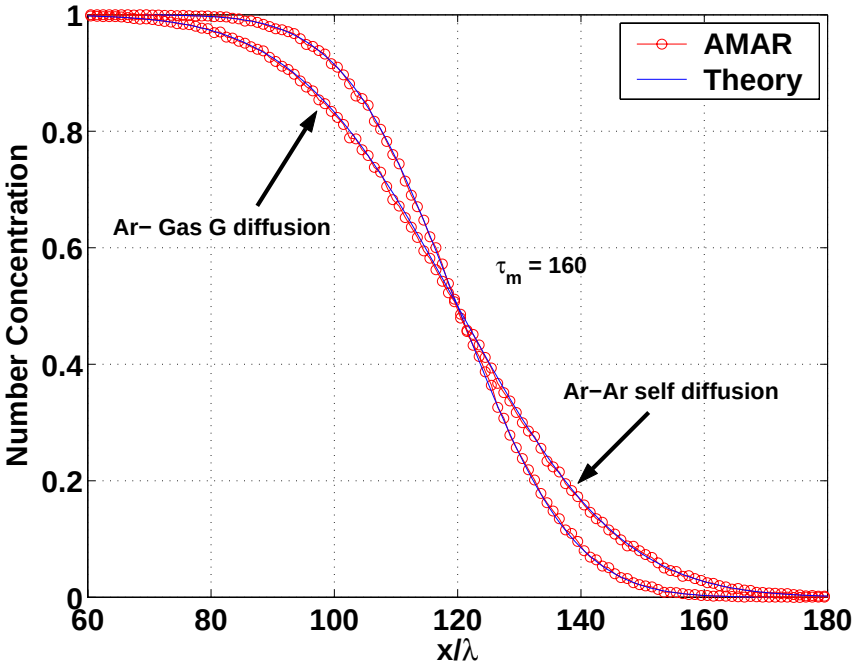

Figure 6-14: Comparison of profiles obtained simulating diffusion with AMAR with theoretical diffusion profiles. Both self-diffusion and two-species diffusion are shown. Note λ refers to the Ar-Ar mean free path. The mean collision time τ_m is also associated with the Ar-Ar system.

and u velocity ratios to be 3.57, 8.68 and 0.28 respectively at this Mach number. These ratios are reflected in the initial conditions used for the test listed in Table 6.2. The DSMC simulation utilized 80 particles per λ^3 for this test.

A density gradient tolerance parameter $R_\rho = 0.2$ was used to detect and refine the continuum grid region across the shock front. This value for R_ρ creates a stable $\pm 10\lambda$ atomistic region ahead of and behind the shock. Note this value also lies within the $3-4\sigma$ curves in Figure 6-9.

The step profile shock initialization gradually transitions to a smoother curved profile

Property	Interval 0	Interval 1
Density (g/cm^3)	0.00178	0.00636
Velocity u (cm/s)	153902.0	43092.5
Temperature (K)	273.0	2369.6
Mass concentration	1.0	1.0

Table 6.2: Initial conditions for single gas stationary shock test. Interval 0 and Interval 1 correspond to upstream and downstream regions either side of the shock wave interface.

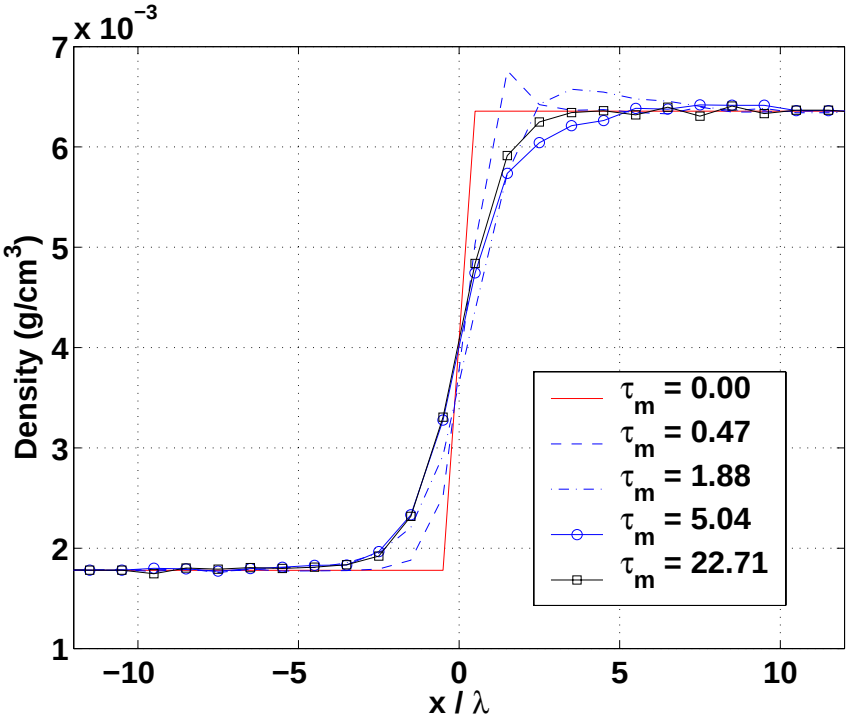

Figure 6-15: Argon gas density profile relaxation to equilibrium. τ_m is the mean collision time.

within the DSMC region as shown in Figure 6-15. The final equilibrium profiles for pressure, density, u velocity and temperature are shown in Figure 6-16. The hybrid solution matches the analytical solution in the far field while resolving the flow discontinuity at the shock front. Note since the initial step profile density gradient is infinite, the shock front will be refined for any setting of R_ρ. However as the profile becomes smoother, the value of R_ρ must be such that the shock front remains tagged for refinement while ensuring the atomistic subdomain does not grow excessively by tracking statistical fluctuations.

6.5.4 Binary Gas Stationary Shock Wave

A binary gas shock simulation was conducted to validate the multispecies capability of the AMAR hybrid scheme. A 97% Helium and 3% Xenon gas mixture by number density was chosen as a test case. The hard sphere mass and diameter for Helium and Xenon were specified as $m_1 = 6.65 \times 10^{-24}$g, $m_2 = 2.18 \times 10^{-22}$g, $\sigma_1 = 2.28 \times 10^{-8}$cm and $\sigma_2 = 5.18 \times 10^{-8}$cm respectively. The upstream flow Mach number was set to 3.89 with a temperature of 300K and reference mass density of 1.07×10^{-7}g/cm^3. These flow conditions were chosen to

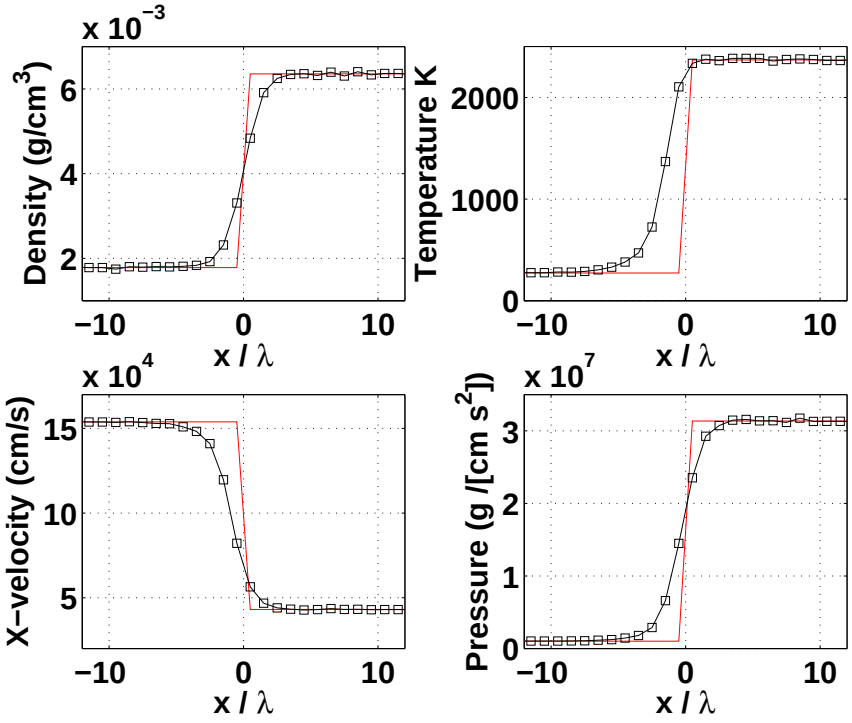

Figure 6-16: Equilibrium shock wave profiles for density, temperature, velocity, and pressure. The solid line is the analytical result, while the solid–square line is the AMAR result.

allow convenient comparison with published results. The corresponding Rankine–Hugoniot relations for the shock density, temperature and velocity ratios are $3.34, 5.59$ and 0.3 respectively. These ratios are reflected in the flow properties used to initialize the shock wave listed in Table 6.3. The DSMC simulation utilized 160 particles per λ^3 of Helium for this simulation. Tolerance parameters were not used for this test and instead the refinement region was user specified to extend 15λ ahead of and 35λ behind the step initialized shock front.

Property	Interval 0	Interval 1
Density (g/cm^3)	1.076×10^{-7}	3.593×10^{-07}
Velocity u (cm/s)	283561.0	84944.4
Temperature (K)	300.0	1677.4
Mass concentration	0.496555	0.496555

Table 6.3: Initial conditions for He–Xe binary gas stationary shock test. Interval 0 and Interval 1 correspond to upstream and downstream regions either side of the shock wave interface.

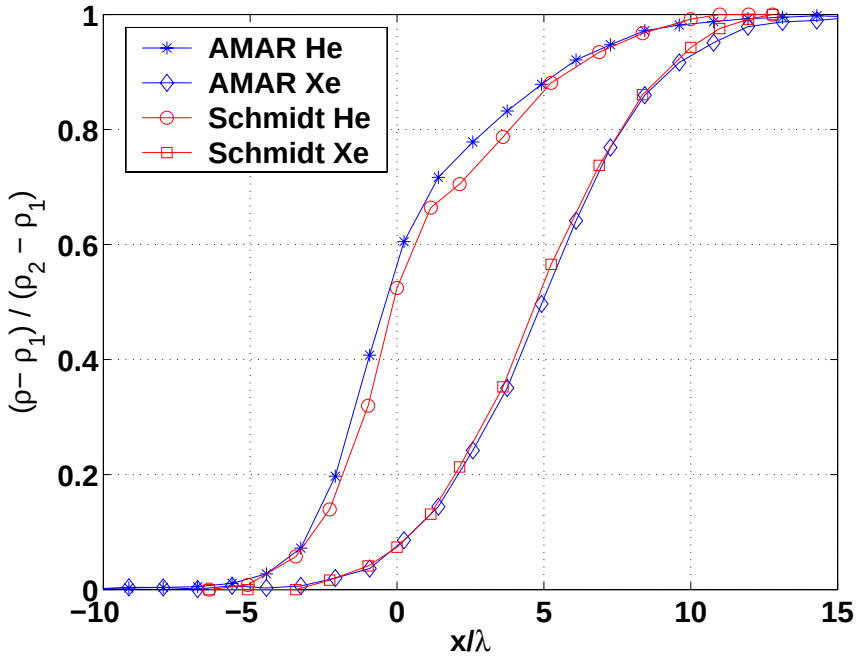

Figure 6-17: Comparison of He–Xe binary gas shock wave equilibrium profiles computed with AMAR and a fully DSMC simulation [79]. The mixture mean free path $\lambda = 0.46$ mm for this test.

Similar to the single gas shock case, the binary gas shock profile also transitions from the initial discontinuous step profile to a smoother equilibrium profile. A comparison of the equilibrium density profiles obtained by AMAR and a fully DSMC simulation [79] is shown in Figure 6-17. The lighter He gas density profile leads the heavier Xe gas density profile. Good qualitative and quantitative agreement is obtained.

6.5.5 Moving Shock Wave

Adaptive feature–tracking of the AMAR hybrid scheme is further validated using a $M = 5$ moving shock passing through a stationary Argon gas. The flow properties across the shock wave are listed in Table 6.4. 80 DSMC particles per cubic mean free path were used for the atomistic simulation.

Figure 6-18 shows the shock front dynamically tracked by the atomistic domain. Similar to the case of a stationary $M = 5$ shock wave a density gradient tolerance $R_\rho = 0.2$ was found successful to ensure the atomistic region extended $\pm 10\lambda$ about the shock front.

The density profile of the moving shock is shown in Figure 6-19. Good comparison is

Property	Interval 0	Interval 1
Density (g/cm^3)	0.00636	0.00178
Velocity u (cm/s)	110809.0	0.0
Temperature (K)	2369.6	273.0
Mass concentration	1.0	1.0

Table 6.4: Initial conditions for $M = 5$ moving shock test. Interval 0 and Interval 1 correspond to upstream and downstream regions either side of the shock wave interface.

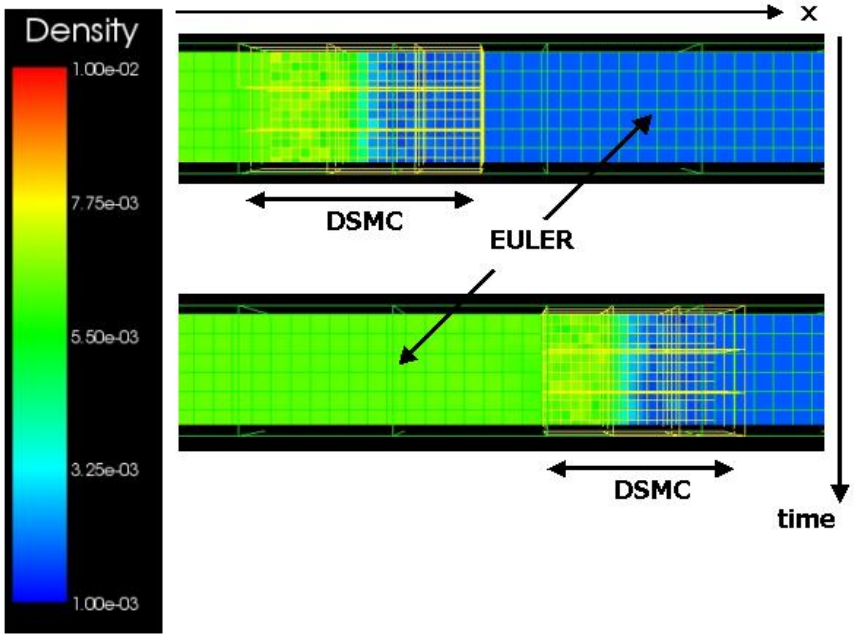

Figure 6-18: Moving Mach 5 shock wave though Argon.The AMAR algorithm tracks the shock by adaptively moving the DSMC region with the shock front.

seen with the analytical result. It is interesting to note that the density profile does not produce spurious post–shock oscillations that are well known to plague shock capturing schemes [10, 98]. Moving shock simulations using conventional shock capturing schemes for the Euler equations require artificial viscosity and enhanced smoothing techniques to reduce oscillations which recur in a periodic manner and often cannot be eliminated entirely. The use of a hybrid scheme with the shock front resolved with DSMC generates a resolved solution without spurious oscillations and artificial numerical constructs.

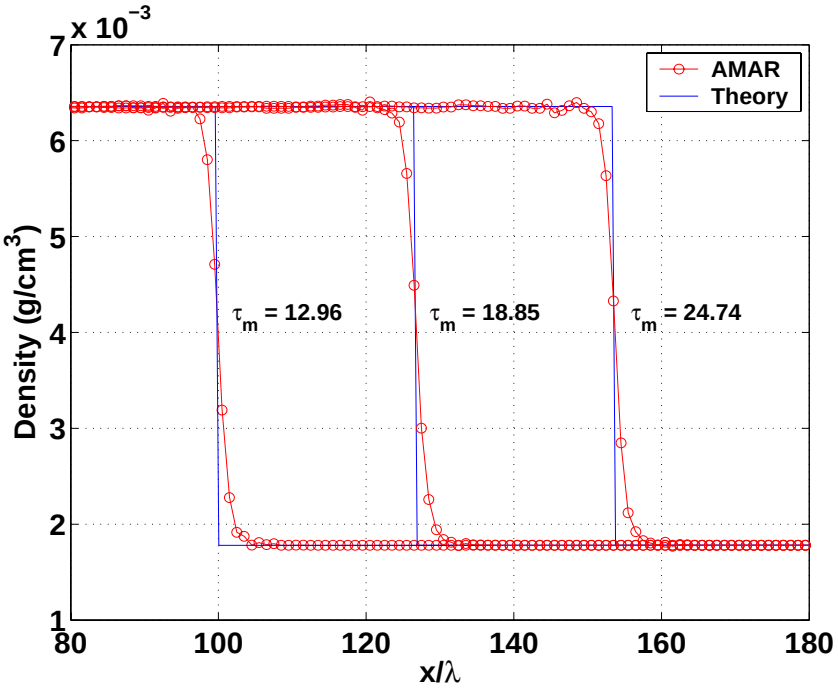

Figure 6-19: Moving $M = 5$ shock wave though Argon gas. The AMAR profile is compared with the analytical time evolution of the initial discontinuity. τ_m is the mean collision time.

6.5.6 Richtmyer–Meshkov Instability

The Richtmyer–Meshkov instability (RMI) (Meshkov [65, 66], Richtmyer [75]) is generated when a shock wave refracts through the interface between two gases. The impulse from the shock wave causes perturbations on the interface to grow in size which in turn creates a mixing layer between the two gases [53]. RMI is a significant test problem from which to assess both the adaptive feature tracking and multispecies capability of the AMAR hybrid scheme. For the simulation considered here adaptive mesh refinement is considered only for tracking the shock front.

The computational domain illustrated in Figure 6-20 was used for the RMI simulation. Argon gas and a fictitious gas B with hard sphere mass and diameter $m_B = 1.326 \times 10^{-22}$g, $\sigma_B = 3.66 \times 10^{-8}$cm were chosen for the test. In order to reduce diffusion between the gases the cross collision diameter σ_{12} defined in Equation (6.7) was increased by a factor of 4. The density ratio across the gas–gas interface was initialized to $\rho_2/\rho_1 = 1.5$ (which corresponds to an Atwood number $At = ((\rho_2/\rho_1) - 1)/((\rho_2/\rho_1) + 1) = 0.2$). The lighter Argon gas occupies the left hand side of the interface while the heavier gas B occupies the right hand

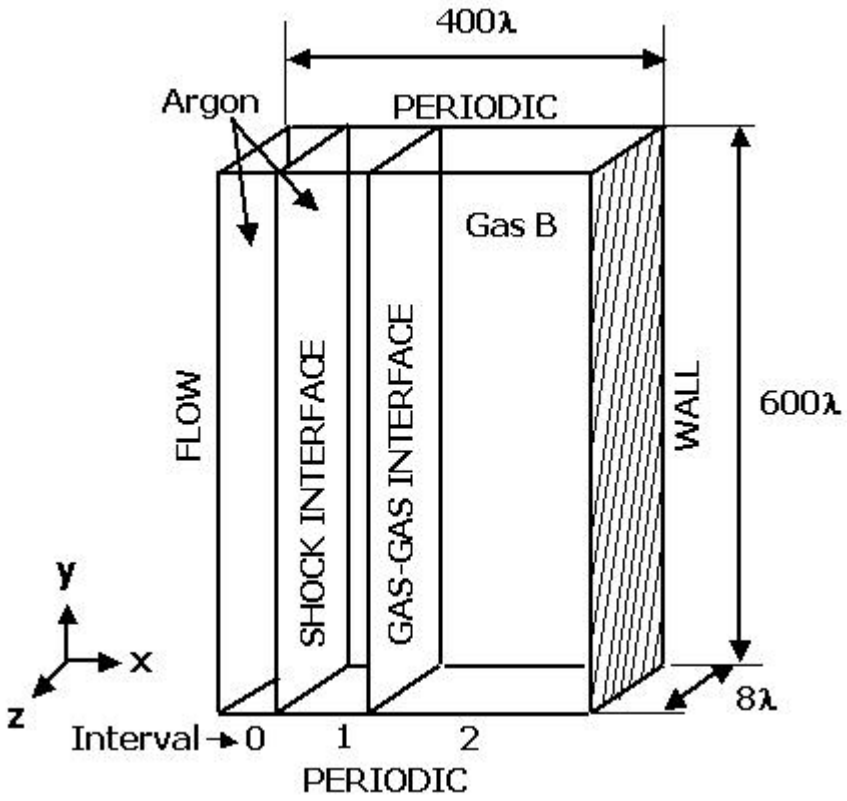

Figure 6-20: Computational domain for Richtmyer–Meshkov instability simulation.

side. The shock wave is initialized upstream of the gas–gas interface and propagates at Mach number $M = 4.0$ through Argon gas. The gas–gas interface has an initial sinusoidal profile with wavelengths 171λ and 57λ superimposed. Peak to trough amplitudes vary here between 8λ and 32λ.

On interception with the interface a reflected shock returns upstream and a transmitted shock continues through gas B. On reflection with the right hand wall, the transmitted shock returns past the interface and leaves the domain through the left face. The flow conditions at initialization are listed in Table 6.5 for each interval $0, 1$ and 2 defined in Figure 6-20. 20 DSMC particles per cubic mean free path of Argon is utilized for this simulation.

A density gradient tolerance $R_\rho = 0.6$ ensures the atomistic subdomain is localized about the shock wave region only while the gas–gas interface remains non–refined. Figures 6-21, 6-22 and 6-23 show the propagation of the shock front through the gas–gas interface. Note that Figure 6-23 also shows a reflected shock wave traveling upstream in addition to the transmitted shock through the gas–gas interface. The particular choice of R_ρ allows

Property	Interval 0	Interval 1	Interval 2
Density (g/cm^3)	0.00599	0.00178	0.00267
Velocity u (cm/s)	86569.9	0.0	0.0
Temperature (K)	1600.7	273.0	364.0
Mass concentration	1.0	1.0	0.0

Table 6.5: Initial conditions for Richtmyer–Meshkok instability test problem. Interval 0,1 and 2 are defined in Figure 6-20.

only for the transmitted shock wave to be refined in this case.

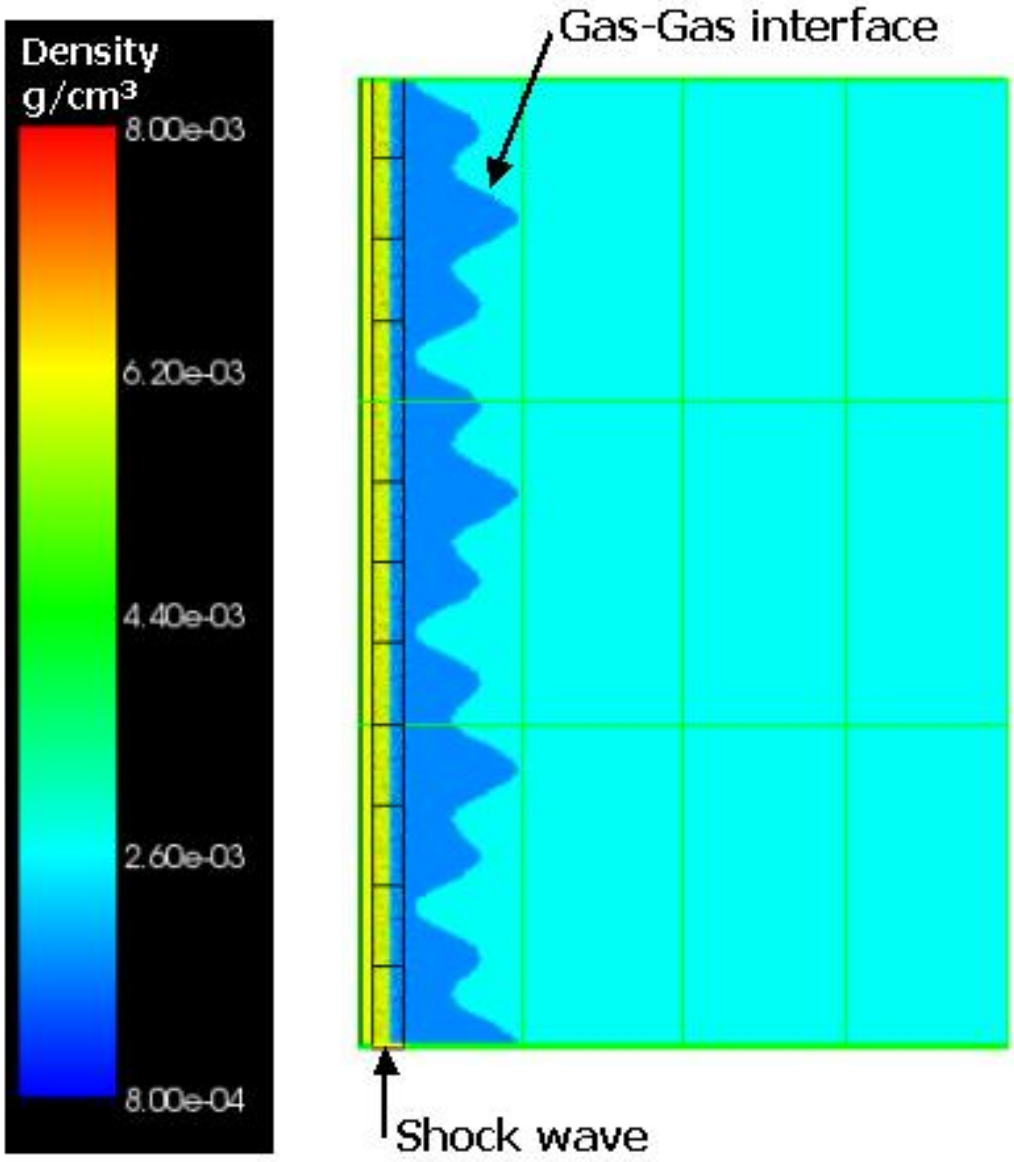

Figure 6-21: Density contour plot of Richtmyer–Meshkov instability simulation. Shock wave is ahead of the gas–gas interface. The time $t = 1.3\tau_m$ where τ_m is the Argon-Argon mean collision time.

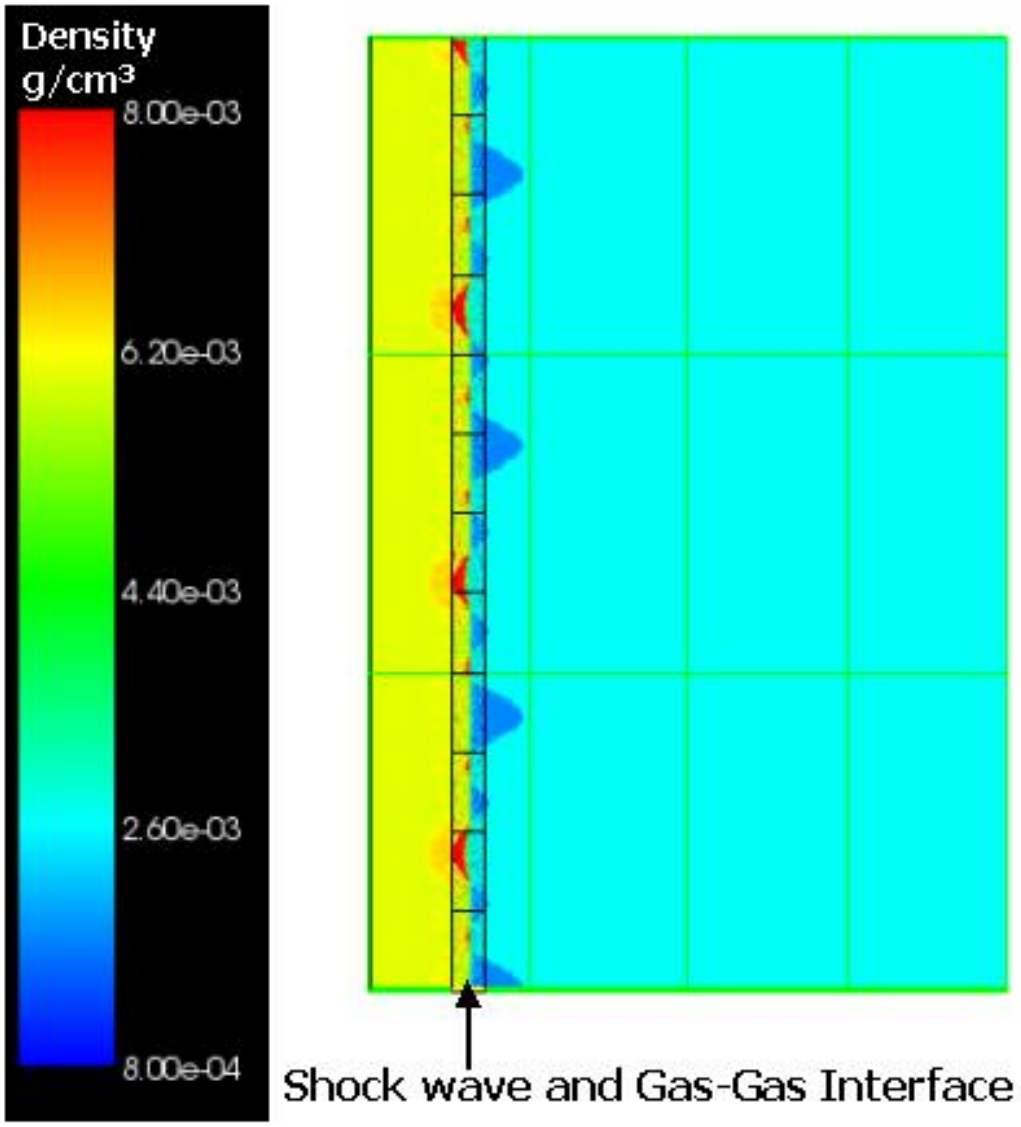

Figure 6-22: Density contour plot of Richtmyer–Meshkov instability simulation. Shock wave intercepts the gas–gas interface. The time $t = 26.0\tau_m$ where τ_m is the Argon-Argon mean collision time.

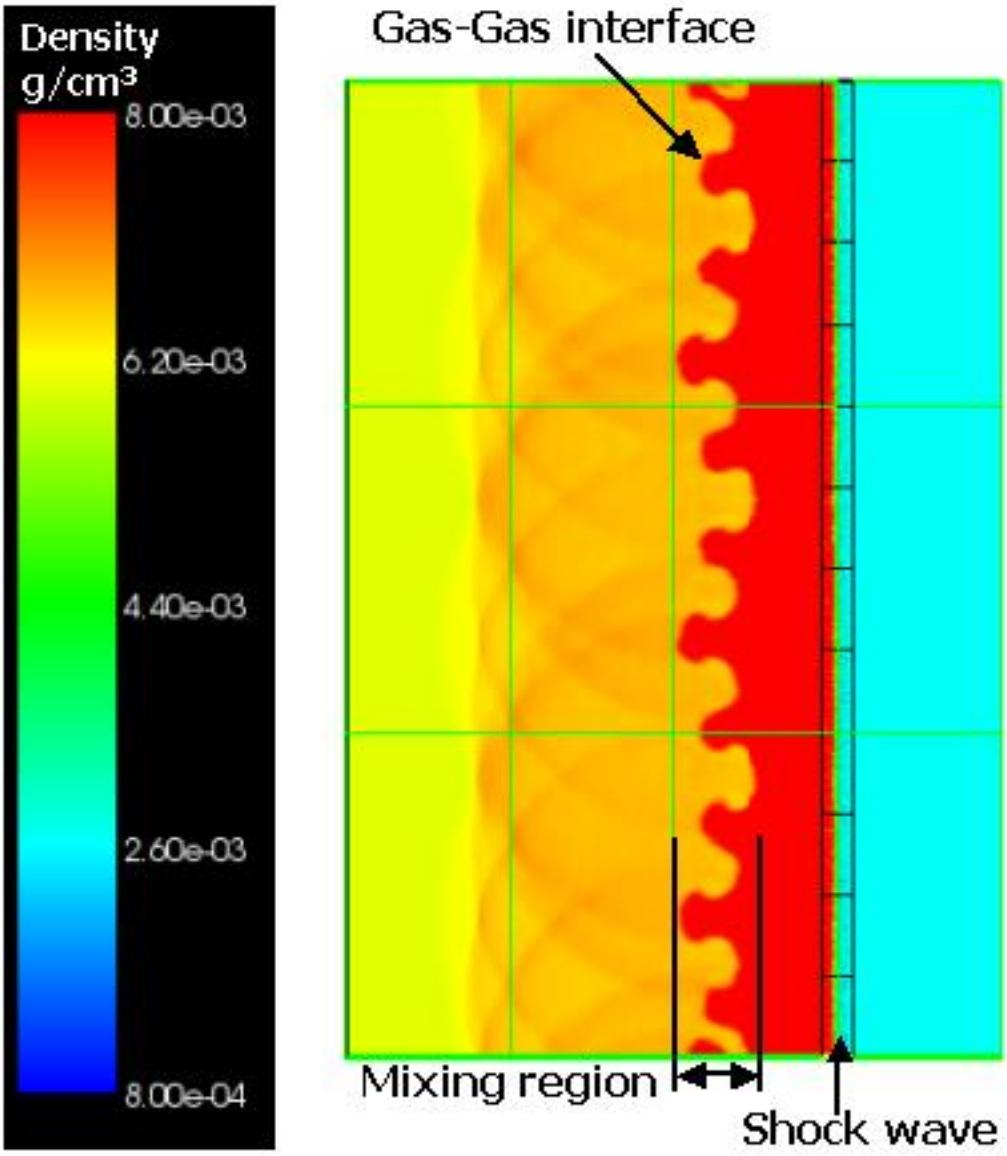

Figure 6-23: Density contour plot of Richtmyer–Meshkov instability simulation. Shock wave has passed the gas-gas interface. The time $t = 170.1\tau_m$ where τ_m is the Argon-Argon mean collision time.

Chapter 7

Summary

The development of nano and micro scale engineering devices has increased the need for accurate and efficient computation of multiscale hydrodynamic phenomena. Hybrid atomistic–continuum formulations provide a novel approach which combines the efficiency of established continuum field solution methods with the high fidelity of atomistic simulation tools. The present work has provided an overview of the current state–of–the–art in this field and has focused on hybrid scheme development for a variety of flow regimes as outlined in Figure 7-1. A summary of the work presented in this thesis is given below together with suggestions for further work.

7.1 Incompressible Flows

The true benefits of hybrid schemes are realized when both length scale *and* time scale de–coupling can be achieved between the solution schemes for the atomistic and continuum subdomains.

The present work demonstrates how this can be realized for incompressible steady and unsteady gaseous flows by using the Schwarz alternating method. Within the Schwarz coupling framework, an overlap region facilitates information exchange between the continuum and atomistic subdomains in the form of Dirichlet boundary conditions. Schwarz iterations using updated boundary conditions are repeated using steady solutions in both subdomains until convergence, i.e. until the solutions in the two subdomains are identical in the over-

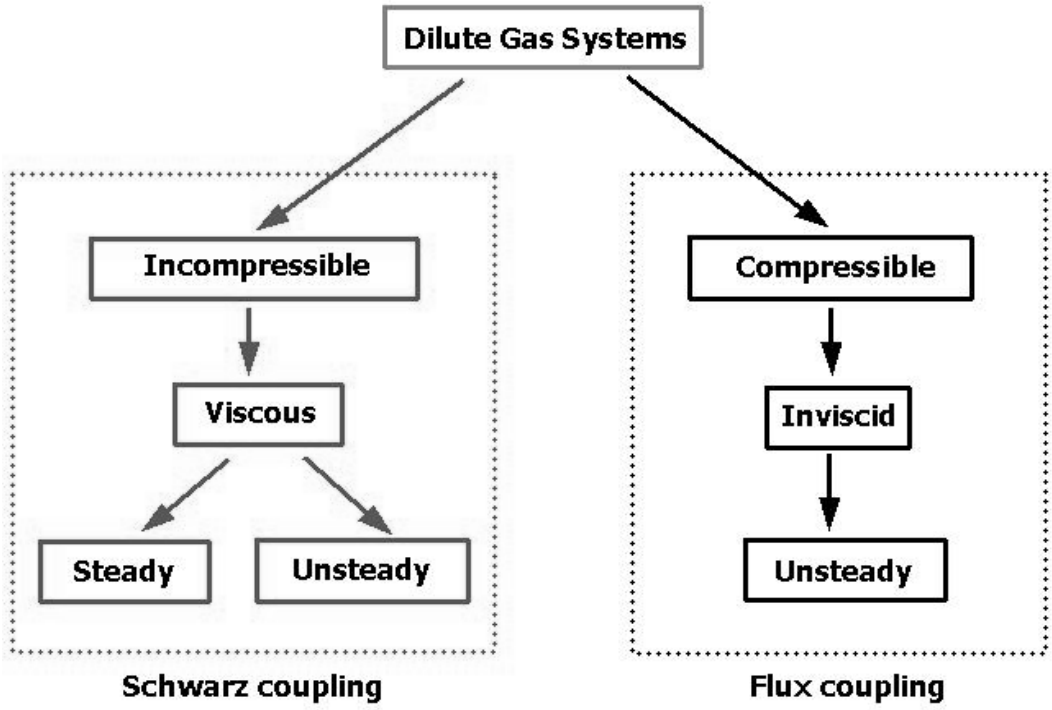

Figure 7-1: Scope of hybrid schemes considered in present work. The flow classification is specific to the assumptions used for the continuum submodel.

lap region. The Schwarz coupling scheme applied to a 2–dimensional driven cavity flow at Reynolds number $O(1)$ is found to converge within $O(10)$ Schwarz iterations.

The imposition of Navier–Stokes boundary conditions on the atomistic subdomain was also demonstrated here using the Chapman–Enskog distribution function in conjunction with particle reservoirs. In addition to sampling reservoir particle velocities from a Chapman–Enskog distribution parametrized by the continuum velocity and temperature fields, it is also essential to locate particles in the reservoir in a way that is consistent with the continuum density field. The latter requirement must not be overlooked as it appears to be of great importance to the correct imposition of boundary conditions.

For the unsteady flow case successive Schwarz iterations are used to converge the solution to a given time t^n. The converged solution at t^n forms the initial condition for subsequent Schwarz iterations to advance the solution to t^{n+1}. Time step decoupling is still feasible here provided appropriate interpolation between boundary conditions is performed. Solution of an atomistic–continuum 1–dimensional impulsive Couette flow test problem using unsteady Schwarz coupling shows good comparison with a fully atomistic simulation.

A method to further reduce the computational cost for unsteady hybrid schemes was also proposed using limited ensemble averaging. This method involves splitting the time step over which the solution advances into 2 intervals. The first interval is advanced using a smaller number of ensemble solutions relative to the second interval. For this particular implementation a factor of 2 computational savings was possible over non–accelerated unsteady Schwarz coupling while retaining the same error reduction. For flows with larger separation of time scales (between the atomistic relaxation time and the global solution time scale) significantly larger savings can be obtained.

7.2 Compressible Flows

For the case of high speed compressible fluid flows, atomistic–continuum coupling was achieved through explicit coupling of fluxes. The Adaptive Mesh and Algorithm Refinement (AMAR) hybrid scheme formulated by Garcia et. al. [36] has demonstrated the feasibility of this approach by using mesh refinement as a natural framework for robust explicit coupling of an atomistic fluid representation and a continuum field model. The finest level of an adaptive mesh refinement (AMR) hierarchy is replaced here by the direct simulation Monte Carlo atomistic simulation method. The continuum field is modeled using the compressible Euler equations and is solved using a second order Godunov scheme. The AMAR application code is implemented in C++ and is built upon the SAMRAI (Structured Adaptive Mesh Refinement Application Infrastructure) framework developed at the Lawrence Livermore National Laboratory. Numerical routines were written/modified to include an Euler convection equation for concentration, tagging routines for density and concentration gradient based refinement and DSMC particle flux bookkeeping for binary species simulations. Extensive debugging was performed on the code written here.

The current work has developed robust refinement criteria using tolerances based on the mean and gradients of flow field variables. In particular, density gradient based tolerances R_ρ have been found successful to capture and track moving shock waves. A theory for the effect of atomistic fluctuations on spurious refinement triggering was also developed. This theory uses the fact that the number of particles per cell N_c is Poisson distributed to show the standard deviation of the density fluctuation is proportional to $1/\sqrt{N_c}$. Moreover a

formula was developed for choosing R_ρ such that spurious fluctuations do not trigger rapid and uncontained growth of the atomistic subdomain.

The AMAR hybrid solution for a moving shock wave shows superior stability over existing continuum–only methods. This underlines the capability of hybrid schemes to capture the physics of fluid phenomena using the most appropriate physical models in a theoretically consistent manner.

The present work has also extended AMAR to perform simulations of binary gas mixtures. This has allowed the simulation of binary gas shock waves and also a representative Richtmyer–Meshkov instability calculation where a interface between two gases is accelerated by a moving shock wave.

7.3 Further Work

The adoption of hybrid atomistic–continuum schemes will continue to rely on their ability to deliver significant computational advantages over fully atomistic methods and greater physical accuracy over classical continuum techniques. The modeling of steady, incompressible gaseous flows using hybrid schemes is quite well understood at the current time. Extensions to unsteady flows however will require a significant more effort. While the Schwarz method has been shown to provide efficient coupling, the time integration of the atomistic simulation continues to consume significant computational resources. Methods to coarse grain the time evolution of atomistic systems will be required prior to pursuing investigations of unsteady flow field phenomena. This is further compounded by the poor signal–to–noise characteristics of atomistic schemes at low speeds. Hence methods for variance reduction of the atomistic solution must also be further explored.

Although not covered in this work, hybrid schemes for liquid modeling have the most to benefit from novel continuum to atomistic boundary condition imposition techniques. The need to use molecular dynamics for atomistic simulation of liquids limits almost by design the options available for efficient boundary imposition. Greater understanding of the packing and structure of liquid molecules and their velocity distributions will be required before significant benefits can be realized here.

The AMAR hybrid scheme has demonstrated the validity of an Euler–DSMC formulation for compressible flows. Future work should focus on adoption of a Navier–Stokes model using the same algorithmic framework to increase the range of flow problems that can be analyzed. Criteria for mesh and algorithm refinement should be more tightly coupled with local continuum breakdown, such that tagging of cells for refinement occurs automatically using the most optimal refinement criteria.

Finally, the range of scales and dynamic nature of hybrid schemes emphasizes the need for efficient computational approaches for large–scale parallel computing platforms. The SAMRAI grid hierarchy paradigm offers many advantages to algorithm development and parallel code implementation, including the ability to manage both field data and particles in a single grid system, while allowing workload and data for each method to be distributed in parallel independently of one other. Dynamic load balancing and data distribution algorithms are required to help increase the scale of the problems that can be simulated.

Bibliography

[1] Abraham, F. F., Broughton, J. Q., Bernstein, N. and Kaxiras, E., "Spanning the continuum to quantum length scales in a dynamic simulation of brittle fracture", *Europhysics Letters*, **44**, pp. 783–787, (1998).

[2] Aktas, O. and Aluru, N. R., "A Combined Continuum/DSMC Technique for Multiscale Analysis of Microfluidic Filters", *Journal of Computational Physics*, **178**, pp. 342–372, (2002).

[3] Altas, I. and Burrage, K., "A high accuracy defect-correction multigrid method for the steady incompressible Navier-Stokes equations", *Journal of Computational Physics*, **114**, pp. 227–233, (1994).

[4] Alexander, F. J., Garcia, A. L. and Alder, B. J., "Direct Simulation Monte Carlo for Thin–Film Bearings", *Physics of Fluids*, **6**, no. 12, pp. 3854–3860, (1994).

[5] Alexander, F. J., and Garcia, A. L., "The Direct Simulation Monte Carlo Method", *Computers in Physics*, **11**, pp. 588-593. (1997).

[6] Alexander, F. J., Garcia, A. L. and Alder, B. J., "Cell Size Dependence of Transport Coefficients in Stochastic Particle Algorithms", *Physics of Fluids*, **10**, p. 1540, (1998); erratum, *Physics of Fluids*, **12**, p. 731, (2000).

[7] Alexander, F., Garcia, A. L. and Tartakovsky D., "Algorithm Refinement for Stochastic Partial Diffential Equations: I. Linear Diffusion", *Journal of Computational Physics*, **182** No. (1), pp. 47–66, (2002).

[8] Alonso, A. and Valli, A., "A Domain Decomposition Approach for Heterogeneous Time–Harmonic Maxwell Equations", *Computer Methods in Applied Mechanics and Engineering*, **143**, pp. 97–112, (1997).

[9] Arkilic, E. B., Breuer, K. S., Schmidt, M. A., "Mass flow and tangential momentum accommodation in silicon micromachined channels", *Journal of Fluid Mechanics*, **437**, pp. 29–43, (2001).

[10] Arora, M., Roe, P. L., "On Postshock Oscillations Due to Shock Capturing Schemes in Unsteady Flows", *Journal of Computational Physics*, **130**, p. 25, (1997).

[11] Bercovier, M. and Pironneau, O., "Error Estimates for Finite Element Method Solution of the Stokes Problem in Primitive Variables", *Numerische Mathematik*, **33**, pp. 211–224, (1979).

[12] Berger, M. and Oliger, J., "Adaptive Mesh Refinement for Hyperbolic Partial Differential Equations", *Journal of Computational Physics*, **53**, p. 484, (1984).

[13] Berger, M. and Colella, P., "Local Adaptive Mesh Refinement for Shock Hydrodynamics", *Journal of Computational Physics*, **82**, p. 64, (1989).

[14] Beskok, A., and Karniadakis, G. E., "Simulation of Heat and Momentum Transfer in Complex Microgeometries", *Journal of Thermophysics and Heat Transfer*, **8**, pp. 647–655, (1994).

[15] Beskok, A., and Karniadakis, G. E., "A Model for Flows in Channels, Pipes and Ducts at Micro and Nano Scales", *Microscale Thermophysical Engineering*, **3**, pp. 43–77, (1999).

[16] Bhattacharya, D. K. and Lie, G. C., "Molecular-Dynamics Simulations of Nonequilibrium Heat and Momentum Transport in Very Dilute Gas", *Physical Review Letters*, **62**, No. 8, (1989).

[17] Bhattacharya, D.K., and Lie, G.C., "Nonequilibrium gas flow in the transition regime: A molecular–dynamics study", *Physical Review A*, **43**, No. 2, pp. 761–767, (1991).

[18] Bird, G. A., "Approach to Translational Equilibrium in a Rigid Sphere Gas", *Physics of Fluids*, **6**, pp. 1518–1519, (1963).

[19] Bird, G. A., "Breakdown of Translational and Rotational Equilibrium in Gaseous Expansions", *American Institute of Aeronautics and Astronautics Journal*, **8**, p. 1998, (1970).

[20] Bird, G. A., *Molecular Gas Dynamics and the Direct Simulation of Gas Flows*, Clarendon Press, Oxford, (1994).

[21] Burggraf, O. R., "Analytical and numerical studies of the structure of steady separated flows", *Journal of Fluid Mechanics*, **24**, part 1, pp. 113–151, (1966).

[22] Chapman, S. and Cowling, T. G., *The mathematical theory of non-uniform gases*, Cambridge University Press, (1970).

[23] Cercignani, C., *The Boltzmann Equation and its Applications*, Springer-Verlag, New York, (1988).

[24] Colella, P., "A Direct Eulerian MUSCL Scheme for Gas Dynamics", *SIAM Journal on Scientific and Statistical Computing*, **6**, pp. 104–117, (1985).

[25] Colella, P. and Glaz, H. M., "Efficient Solution Algorithms for the Riemann Problem for Real Gases", *Journal of Computational Physics*, **59**, pp. 264–289, (1985).

[26] Coronell, D. G. and Jensen, K. F., "Analysis of Transition Regime Flows in Low Pressure CVD Reactors Using the Direct Simulation Monte Carlo Method", *Journal of the Electrochemical Society*, **139**, pp. 2264–2273, (1992).

[27] Dawson, C. N., Du, Q. and Dupont, T. F., "A Finite Difference Domain Decomposition Algorithm for Numerical Solution of the Heat Equation", *Mathematics of Computation*, **57**, 195, pp. 63–71, (July 1991).

[28] Dawson, C. N. and Dupont, T. F., "Explicit/Implicit Conservative Galerkin Domain Decomposition Procedures for Parabolic Problems", *Mathematics of Computation*, **58**, 197, pp. 21–34, (Jan., 1992).

[29] Delgado–Buscalioni, R. and Coveney, P. V., "Continuum–Particle Hybrid Coupling for Mass, Momentum and Energy Transfers in Unsteady Fluid Flow", *Physical Review E*, **67**, No. 4, (2003)

[30] Devroye, L., *Non-Uniform Random Variate Generation*, Springer-Verlag, New York, (1986), [Garcia, A. L., *Numerical Methods for Physics*, Prentice Hall, New Jersey, (1994)].

[31] Eggers, J. and Beylich, A., "New algorithms for application in the direct simulation Monte Carlo method", *Progress in Astronautics and Aeronautics*, **159**, pp. 166–173, (1994).

[32] Fallavollita, M. A., Baganoff, D. and McDonald, J. D., "Reduction of Simulation Cost and Error for Particle Simulations of Rarefied Flows", *Journal of Computational Physics*, **109**, pp. 30–36, (1993).

[33] Flekkoy, E. G., Wagner, G. and Feder, J., "Hybrid model for combined particle and continuum dynamics", *Europhysics Letters*, **52**, pp. 271–276, (2000).

[34] Fukui, S. and Kaneko, R., "Analysis of Ultra Thin Gas Film Lubrication Based on Linearized Boltzmann Equation: First Report–Derivation of a Generalized Lubrication Equation Including Thermal Creep Flow", *Journal of Tribology*, **110**, pp. 253–262, (1988).

[35] Garcia, A .L. and Alder, B. J., "Generation of the Chapman Enskog Distribution", *Journal of Computational Physics*, **140**, pp. 66–70, (1998).

[36] Garcia, A. L., Bell, J. B., Crutchfield, W. Y. and Alder, B. J., "Adaptive Mesh and Algorithm Refinement Using Direct Simulation Monte Carlo", *Journal of Computational Physics*, **54**, pp. 134–155, (1999).

[37] Garcia, A. L. and Wagner, W., "Time step truncation error in direct simulation Monte Carlo," *Physics of Fluids*, **12**, pp. 2621–2633, (2000).

[38] Garcia, A. L., *Numerical Methods for Physics*, Prentice Hall, (2000).

[39] Garcia, A. L., "Notes On The Random Placement of Particles in the Presence of a Gradient", Personal notes, Dept. of Physics, San Jose State University, CA.

[40] Garcia, A. L., Private communication.

[41] Gartling, D., and Becker, E., "Finite Element Analysis of Viscous, Incompressible Fluid Flow", *Computer Methods in Applied Mechanics and Engineering*, **8**, pp. 51–60, (1960).

[42] Ghia, U., Ghia, K. N. and Shin, C. T., "High-Re solutions for incompressible flow using the Navier-Stokes equations and a multigrid method", *Journal of Computational Physics*, **48**, pp. 387-411, (1982).

[43] Glowinski, R., Periaux, J., Shi, Z-C. and Widlund, O., *Domain Decomposition Methods in Science and Engineering; 8th International Conference, Beijing, China*, Wiley, (1997).

[44] Gunawardena, N., Private communication.

[45] Gupta, M. M., "High accuracy solutions of incompressible Navier-Stokes equations", *Journal of Computational Physics*, **93**, pp. 343–359, (1991).

[46] Hadjiconstantinou, N. G. "Hybrid Atomistic-Continuum Formulations and the Moving Contact Line Problem", PhD Thesis, Mechanical Engineering Department, Massachusetts Institute of Technology, Cambridge, Massachusetts, (1998).

[47] Hadjiconstantinou, N. G. and Patera A. T., "Heterogeneous Atomistic-Continuum Representations for Dense Fluid Systems", *International Journal of Modern Physics C*, **8**, pp. 967–976, (1997).

[48] Hadjiconstantinou, N. G., "Hybrid Atomistic-Continuum Formulations and the Moving Contact-Line Problem", *Journal of Computational Physics*, **154**, pp. 245–265, (1999).

[49] Hadjiconstantinou, N. G., "Analysis of discretization in the direct simulation Monte Carlo", *Physics of Fluids*, **12**, pp. 2634–2638, (2000).

[50] Hadjiconstantinou, N. G., Garcia, A. L., Bazant, M. Z. and He, G., "Statistical Error in Particle Simulations of Hydrodynamic Phenomena", *Journal of Computational Physics*, **187**, pp. 274–297, (2003).

[51] Hash, D., and Hassan, H., "A Hybrid DSMC/Navier-Stokes Solver", *AIAA Paper 95-0410*, (1995).

[52] Hirschfelder, J. O., Curtiss, C. F. and Bird, B., *Molecular theory of gases and liquids*, New York, Wiley (1964).

[53] Holmes, R. L., Dimonte, G., Fryxell, B., Gittings, M. L., Grove, J. W., Schneider, M., Sharp, D. H., Velikovich, A. L., Weaver, R. P., Zhang, Q., "Richtmyer–Meshkov Instability Growth: Experiment, Simulation and Theory", *Journal of Fluid Mechanics*, **389**, pp. 55–79, (1999).

[54] Hood, R., Taylor, C., "Navier Stokes Equations Using Mixed Interpolation", *Finite Element Methods in Flow Problems*, pp. 121–132, University of Alabama Press, Huntsville, (1974).

[55] Hornung, R. D. and Wissink, A. M., "SAMRAI Sample Euler Application: Computation of 3-Dimensional Flux Terms", Internal Report, Center for Applied Scientific Computing, Lawrence Livermore National Laboratory, Livermore, CA 94551.

[56] Hornung, R. D. and Kohn, S. R., "Managing Application Complexity in the SAMRAI Object-Oriented Framework", *Concurrency and Computation: Practice and Experience*, **14**, pp. 347–368, (2002).

[57] Hou, S. L., Zou, Q., Chen, S. Y., Doolen, G. and Cogley A. C., "Simulation Of Cavity Flow By The Lattice Boltzmann Method", *Journal of Computational Physics*, **118**, No. 2, pp. 329–347, (1995).

[58] Huebner, K. H., Thornton, E. A., Byrom T. G., *The finite element method for engineers*, Wiley, (1995).

[59] Landau, L. D. and Lifshitz, E. M., *Statistical Mechanics*, Part 2, Pergamon Press, Oxford, (1980).

[60] Li, J., Liao, D. and Yip S., "Nearly exact solution for coupled continuum/MD fluid simulation", *Journal of Computer-Aided Materials Design*, **6**, pp. 95–102, (1999).

[61] Lions, P. L., "On the Schwarz alternating method. I.", *First International Symposium on Domain Decomposition Methods for Partial Differential Equations*, Eds. R. Glowinski, G. Golub, G. Meurant and J. Periaux, 1–42, SIAM, Philadelphia, (1988).

[62] Liu, S. H., "On Schwarz Alternating Methods For The Incompressible Navier-Stokes Equations", *Siam Journal of Scientific Computing*, **22**, No. 6, pp. 1974–1986, (2001).

[63] Mansour, M. M., Baras, F. and Garcia, A. L., "On the validity of hydrodynamics in plane Poiseuille flows", *Physica A*, **240**, pp. 255–267, (1997).

[64] Maxwell, J. C., *Philosophical Transactions of the Royal Society*, London, **170**, (No. 231), (1867).

[65] Meshkov, E. E., "Instability of the Interface of two Gases Accelerated by a Shock Wave", *Fluid Dynamics*, **43** (No. 5), pp. 101–104, (1969).

[66] Meshkov, E. E., "Instability of a Shock Wave Accelerated Interface between two Gases", *NASA Technical Translation*, **F-13**, 074, (1970).

[67] Morris, D. L., Hannon, L., and Garcia, A. L., "Slip length in a dilute gas", *Physical Review A*, **46**, pp. 5279–5281, (1992).

[68] Ohwada T., Sone, Y., Aoki, K., "Numerical Analysis of the shear and thermal creep flows of a rarefied gas over a plane wall on the basis of the linearized Boltzmann equation for hard-sphere molecules", *Physics of Fluids A*, **1**, (No. 9), pp. 1588–1599, (1989).

[69] O'Connell, S. T. and Thompson, P.A., "Molecular dynamics-continuum hybrid computations: A tool for studying complex fluid flows", *Physical Review E*, **52**, pp. R5792–R5795, (1995).

[70] Olson, M. D. and Tuann, S. Y., "Primitive Variable versus Stream Function Finite Element Solutions of the Navier–Stokes Equations", *Finite Elements in Fluids*, Chapter 4, Vol. 3, Wiley, New York, pp. 73–87, (1978).

[71] Perktold, K. and Rappitsch, G., "Computer Simulation of Local Blood Flow and Vessel Mechanics in a Compliant Carotid Artery Bifurcation Model", *Journal of Biomechanics*, **28**, pp. 845–856, (1995).

[72] Press, W. H., Flannery, B. P., Teukolsky, S. A., Vetterling, W. A., *Numerical Recipes in Fortran*, Cambridge University Press, (1992).

[73] Quarteroni, A., Pasquarelli, F. and Valli, A., "Heterogeneous Domain Decomposition: Principles, Algorithms, Applications", in *Fifth International Symposium on Domain Decomposition Methods for Partial Differential Equations*, Keyes, D. E., et.al. eds., SIAM, Philadelphia, pp. 129–150, (1992).

[74] Quarteroni, A., *Domain decomposition methods for partial differential equations*, Oxford, New York, Clarendon Press, (1999).

[75] Richtmyer, R. D., "Taylor Instability in Shock Acceleration of Compressible Fluids", *Communications on Pure and Applied Mathematics*, **13**, pp. 297–319, (1960).

[76] Roveda, R., Goldstein, D. B. and Varghese, P. L., "Hybrid Euler/direct simulation Monte Carlo calculation of unsteady slit flow", *Journal of Spacecraft and Rockets*, **37** No. 6, pp. 753–760, (2000).

[77] Rudd, R.E and Broughton, J. Q., "Concurrent coupling of length scales in solid state systems", *Physica Status Solidi B-Basic Research*, **217**, pp. 251–291, (2000).

[78] Saltzman, J., "An Unsplit 3D Upwind Method for Hyperbolic Conservation Laws", *Journal of Computational Physics*, **115**, p. 153, (1994).

[79] Schmidt, B. and Worner, M., "Problems with the Computation of the Shock Structure in Binary Gas Mixtures Using the Direct Simulation Monte Carlo Method", *Acta Mechanica*, (1-4), pp. 59–55, (1983).

[80] Schreiber, R. and Keller, H. B., "Driven Cavity Flows by Efficient Numerical Techniques", *Journal of Computational Physics*, **49**, pp. 310–333, (1983).

[81] Schwarz, H. A., *Gesammelte Mathematische Abhandlungen*, **2**, pp. 133–143, Springer, Berlin, 1890. First published in *Vierteljahrsschrift Naturforsch. Ges. Zurich*, **15**, pp. 272–286, (1870).

[82] Shenoy, V. B., Miller, R., Tadmor, E. B., Rodney, D., Phillips R. and Ortiz, M., "An Adaptive Finite Element Approach to Atomic-Scale Mechanics – The Quasicontinuum Method", *Journal of the Mechanics and Physics of Solids*, **47**, p. 611, (1999).

[83] Sone, Y., Ohwada T., and Aoki, K., "Temperature Jump and Knudsen Layer in a rarefied gas over a plane wall: Numerical analysis of the linearized Boltzmann equation for hard–sphere molecules", *Physics of Fluids A*, **1**, No.2, pp. 363–370, (1998).

[84] Structured Adaptive Mesh Refinement Application Infrastructure (SAMRAI), http://www.llnl.gov/CASC/

[85] Smith, B., Bjorstad, P., Gropp, W., *Domain Decomposition. Parallel Multilevel Methods for Elliptic Partial Differential Equations*, Cambridge University Press, (1996).

[86] Thompson, M. C. and Ferziger, J. H., "An adaptive multigrid technique for the incompressible Navier-Stokes equations", *Journal of Computational Physics*, **82**, pp. 94–121, (1989).

[87] Tison, S. A., "Experimental Data and Theoretical Modeling of Gas Flows through Metal Capillary Leaks", *Vacuum*, **44**, pp. 1171–1175, (1993).

[88] Trangenstein, J. A. and Pember, R. B., "Numerical Algorithms for Strong Discontinuities in Elastic-Plastic Solids", *Journal of Computational Physics*, **103**, pp. 63–89, (1992).

[89] Vanka, S. P,. "Block-Implicit Multigrid Solution of Navier-Stokes Equations in Primitive Variables", *Journal of Computational Physics*, **65**, pp. 138–158, (1986).

[90] Wadsworth, D. C. and Erwin, D. A., "One-Dimensional Hybrid Continuum/Particle Simulation Approach for Rarefied Hypersonic Flows", *AIAA Paper 90-1690*, (1990).

[91] Wadsworth, D. C. and Erwin, D. A., "Two-Dimensional Hybrid Continuum/Particle Simulation Approach for Rarefied Hypersonic Flows", *AIAA Paper 92-2975*, (1992).

[92] Wagner, W., "A Convergence Proof for Bird's Direct Simulation Monte Carlo Method for the Boltzmann Equation," *Journal of Statistical Physics*, **66**, p. 1011, (1992).

[93] Wesseling, P., Multigrid solution of the Navier-Stokes equations in the vorticity-streamfunction formulation, In *Efficient Solutions of Elliptic Systems, Notes on Numerical Fluid Mechanics*, **10**, (Edited by W. Hack- busch), pp. 145–154, Vieweg, Braunschweig, (1984).

[94] Wesseling, P., *Principles of Computational Fluid Dynamics*, p. 569, Springer, (2001).

[95] Wijesinghe, H. S. and Hadjiconstantinou, N. G., "A hybrid continuum-atomistic scheme for viscous incompressible flow", *Proceedings of the 23th International Symposium on Rarefied Gas Dynamics*, pp. 907–914, Whistler, British Columbia, (July, 2002).

[96] Wijesinghe, H. S., Hornung, R., Garcia, A. L., Hadjiconstantinou, N. G., "Three–dimensional Hybrid Continuum–Atomistic Simulations For Multiscale Hydrodynamics", submitted to 2003 International Mechanical Engineering Congress and Exposition

[97] Wong, J. S., Darmofal, D. L. and Peraire, J., "The Solution of the Compressible Euler Equations at Low Mach Numbers Using a Stabilized Finite Element Algorithm", *Computer Methods in Applied Mechanics and Engineering*, **190**, pp. 5719–5737, (2001).

[98] Woodward, P. R. and Colella, P., "The Numerical Simulation of Two-dimensional Fluid Flow with Strong Shocks", *Journal of Computational Physics*, **54**, p. 115, (1984).

[99] Yamada, Y., Ito, K., Yokouchi, Y., Tamano, T., Ohtsubo, T., "Finite Element Analysis of Steady Fluid and Metal Flow", *Finite Elements in Fluids*, Chapter 4, Wiley, New York, (1975).

[100] Yuan, X. and Daiguji, H., "A specially combined lower-upper factored implicit scheme for three dimensional compressible Navier-Stokes equations", *Computers and Fluids*, **30**, pp. 339–363, (2001).